Control over Microstructure Evolution and Device Performance in Solution Processable Organic Field-effect Transistors

Suhao Wang

Control over Microstructure Evolution and Device Performance in Solution Processable Organic Field-effect Transistors

Dissertation

Zur Erlangung des Grades

“Doktor der Naturwissenschaften“

am Fachbereich Chemie, Pharmazie und Geowissenschaften

der Johannes Gutenberg-Universität Mainz

Suhao Wang

geboren in Shandong, P.R China

Mainz, 2013

Dekan:

1. Berichterstatter:

2. Berichterstatter:

Tag der Mündlichen Prüfung: 13, 08, 2013

Table of contents

Chapter 1.

Introduction of Solution Processable Organic Field-effect Transistors (OFETs)

1.1 Introduction

Transistors are essential in our modern life, being used in almost all parts of information technology and most well-renowned in personal computers. Inorganic semiconductors like silicon are the fundamental building blocks of today's electronics. Since the first discovery of organic field-effect transistors (OFETs) in the 1986 by Tsumura and coworkers, OFETs have attracted increasing attention in many areas including chemistry, physics, materials, and micro/nano electronics, due to their wide variety of potential applications, [1-9] e.g. flexible smart cards, low cost radio frequency identification (RFID) tags, electronic paper, and organic active matrix displays (Figure 1.1). Compared to their inorganic counterparts, OFETs possess several advantages, such as flexibility, inherent compatibility with plastic substrates, easy, low-cost and low-temperature processing methods such as solution processing. Up to now, the performance of OFETs is already improved immensely, comparable of that based on amorphous silicon. [10] However, it is still far from satisfactory for many applications which require much higher performance.

The recent attention has been focused on improving device performance and device stability, on reducing the fabrication cost and power consumption, and on developing simple fabrication techniques. While it is well recognized that the molecular structure of semiconductor determines the intrinsic property of the OFET, for a given semiconductor, fulfilling the above mentioned goals relies on optimization of devices. Particularly, the way how molecules self-assemble to form the necessary pathway for the charge carriers has a major impact on the device performance. For instance, poorly packed molecules lead to inefficient charge carrier transport due to insufficient overlap of the molecular orbitals containing free charges, while highly ordered, well arranged molecules provide good molecular orbitals overlap and show unhindered charge carrier transport. In this aspect, the general motivation of this work is to greatly improve charge carrier mobility by further elevating the structural order of the conjugated molecules, for instance in single crystal ribbons of small molecules, or in single fibers of conjugated polymers.

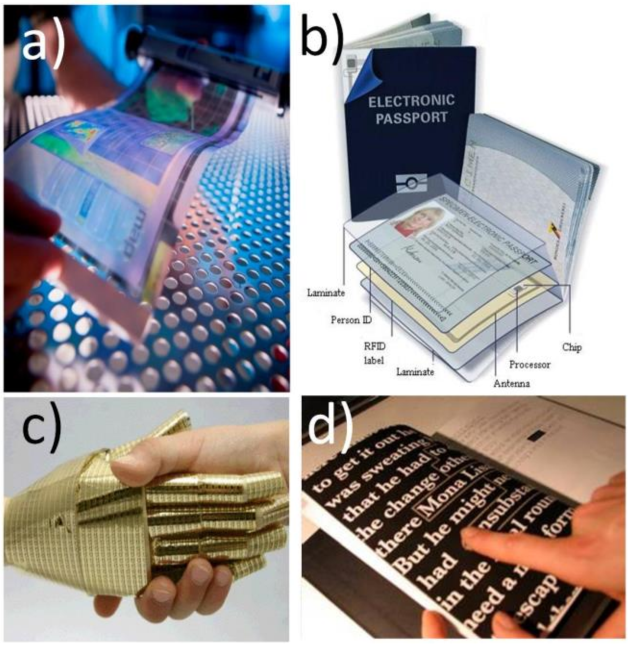

Figure 1.1. Possible applications of OFETs. a) Flexible displays b) RFID c) electronic skin d) electronic paper.[4-7]

Before discussing the research motivation in greater detail, a basic introduction to OFETs is warranted. Therefore, in this chapter, working principal of OFETs, the influencing factors of the device performance, and different processing techniques, especially solution processing, are introduced.

1.2 Working principals of OFETs

A typical OFET consists of a gate electrode, a gate dielectric layer, an organic semiconductor layer and source-drain electrodes. According to the structure of the devices, OFETs can be classified into four types: bottom-gate bottom-contact (BGBC), bottom-gate top-contact (BGTC), top-gate bottom-contact (TGBC) and top-gate top contact (TGTC) (Figure 1.2). The easiest configuration is the BGBC since the device is fabricated simply by depositing the organic semiconductor molecules on top of the dielectric insulator.

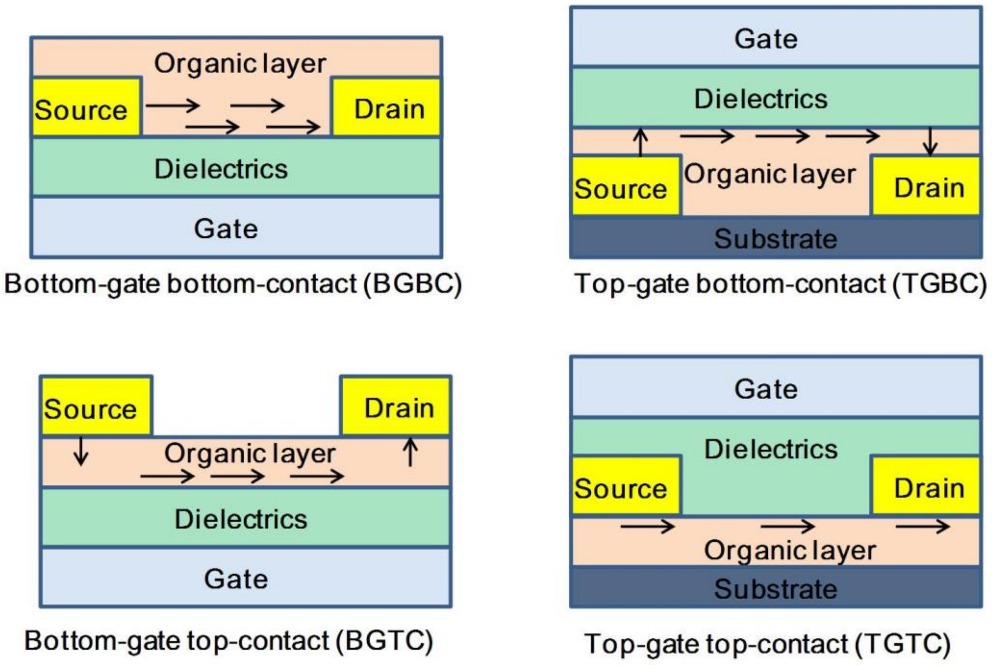

Figure 1.2. Four typical OFET geometries. The black arrows indicate the carrier injection and transport paths.

Before comparing different geometries, firstly the BTBC geometry is used as an example to show the working principal of OFETs. As shown in Figure 1.3a, the gate electrode is covered by a dielectric layer. The semiconductor film is deposited on top of this insulator layer and contacted by source and drain electrodes (in most cases Au is employed). The distance between the source and drain electrode is called channel length. When no gate voltage V_G is applied, the source-drain current I_{SD} is low. theoretically I_{SD} should be zero, as long as the semiconductor is not highly doped and the transistor is off. When a gate voltage is applied, the charge carriers accumulate near the dielectric/organic interface thus forming a conductive channel; the so-called accumulation layer (Figure 1.3b). In other words, the gate electrode controls the conductance of the organic semiconductor (OSC) in the transistor channel, by capacitive coupling of the thin dielectric layer. When the source drain voltage is applied, there will be current flow between the channels. (Figure 1.3c)

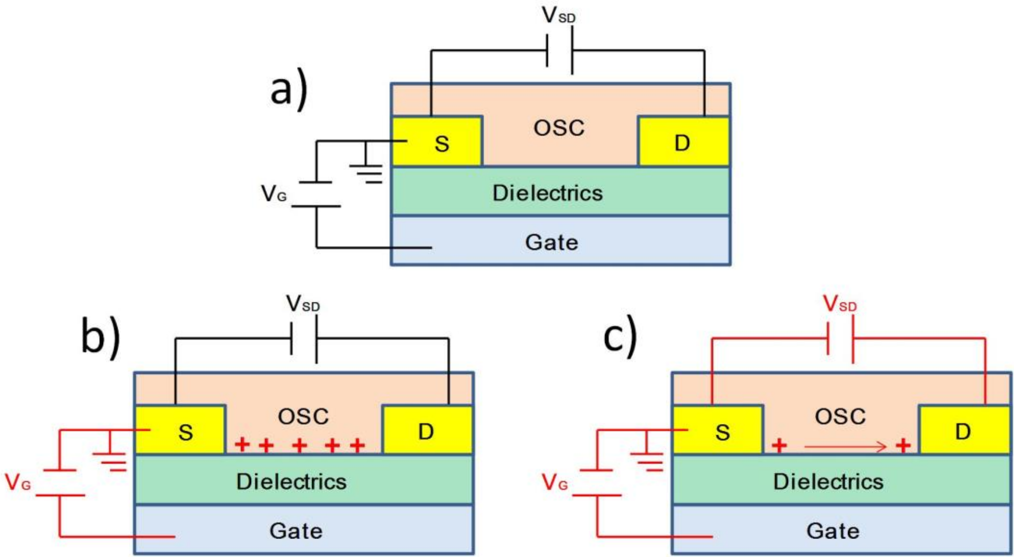

Figure 1.3. Working principal of OFETs. a) Structure of an top contact OFET, b) accumulation of charge carriers (holes in this case), as revealed by the red + symbols in response to an applied V_G; c) current flow caused by an additional V_{SD} applied between the source and drain electrodes.

It is well-accepted that BGTC and TGBC usually exhibit lower contact resistance than BGBC and TGTC. This could be attributed to the different carrier injection paths and injection areas. As is shown in Figure 1.2, in comparison to BGBC and TGTC devices, the BGTC and TGBC ones possess larger injection areas and more favored injection paths, leading to lower contact resistance.

On the other hand, the device geometry can also influence the contact condition. For instance, in BGBC OFETs, the source and drain electrodes have been deposited before the deposition of the organic layers. As a result, the gold electrodes could have a negative influence on the organic layer, because the surface energy between bottom Au electrodes and the SiO_2 surface. As an example, nucleation of pentacene takes place preferentially at the electrodes, which causes clustering and discontinuities in the pentacene film. [11] In such cases, in order to avoid such discontinuities, the top-contact OFET configuration is preferred. Therefore, OFETs based on single crystal microribbon or based on polymer thin films normally adopt top-contact configuration.

1.3 The characterization of OEFTs

To identify a performance of an OFET several important parameters, such as charge carrier mobility μ, *on/off ratio*, *threshold voltage* are used which are defined in the following sections.

1.3.1 Charge carrier mobility

The most important parameter to characterize the performance of OFETs is the charge carrier mobility, μ. It quantifies the average charge carrier drift velocity per unit electric field. The higher the μ, the better a transistor works, or in other words, the easier the charges can be moved by the applied potential.

The charge carrier mobility for transistors operated in saturation is given by:

$$I_{SD} = \frac{W}{2L} \mu_{sat} Ci \left(V_G - V_T\right)^2 \tag{1.1}$$

Here, L and W are the channel length and width, respectively. μ_{sat} is the charge carrier mobility in saturation. Ci is the insulator capacitance per unit area, and V_T is the extrapolated threshold voltage, which will be described in chapter 1.3.3.

Taking the square root of both sides of equation 1.1, we obtain:

$$\sqrt{I_{SD}} = \sqrt{\frac{W}{2L}\mu_{sat}Ci}\left(V_G - V_T\right) \tag{1.2}$$

It can be deemed as a linear equation when plotting $\sqrt{I_{SD}}$ versus V_G. The slope s of such a plot is the coefficient of V_G in equation in 1.2.

$$s = \sqrt{\frac{W}{2L}\mu_{sat}Ci} \Leftrightarrow s^2 = \frac{W}{2L}\mu_{sat}Ci \tag{1.3}$$

After rearranging, finally we get the equation for charge carrier mobility.

$$\mu_{sat} = \frac{2Ls^2}{WCi} \tag{1.4}$$

In short, μ is obtained by taking the slope of the linear fit at square root of the transfer curve and employing equation 1.4.

1.3.2 On/off ratio

Due to their special applications in microelectronics, such as individual pixels in flat panel displays or in computer central processing units (CPUs) for binary logic operations, the on/off ratio is also an important parameter to determine the quality of OFETs as switches. Hereby, the larger differences between on state and off state, the better are the switches.

The on/off ratio is defined as the source-drain current ratio between the on and off states of OFETs. The larger the on/off ratio, the more easily it is to distinguish between the transistor's on and off state. Conventionally, the off current (I_{off}) is the I_{SD} at a special V_{SD} with no gate voltage V_G applied. That is basically the intrinsic conductivity of the semiconductor since no additional charge carriers are being accumulated by the gate voltage. The on current (I_{on}) is the current I_{SD} flowing in the transistor when it is biased with V_{SD} = V_G. Ideally, the off current in organic semiconductor should be very low. There are exceptions, like some low bandgap materials with elevated intrinsic charge carrier density contributing to the current, for instance graphene. Another possiblility for relatively high off current is that the organic semiconductor layer is doped either by chemical impurities or oxygen and moisture. In this case, there are additional charge carriers being triggered even no gate voltage is applied. This can lead to a high off current which might not be significantly lower than the on current. [12-16] In the above-mentioned cases, the on/off ratio will be undesirably evoked. As a possible solution to this problem, a gate voltage can be applied to repel these charge carriers. For instance, for p-type organic semiconductors, negative gate biases are required for the accumulation of holes, in order to form the accumulation layer within the transistor channels, and vice versa for n-type organic semiconductors. As a result, applying the opposite gate bias, e.g. positive V_G for p-type and negative V_G for n-type devices, drives away those undesired charges, turning off the devices and decreasing the off current. In this way, one can get a higher on/off ratio, and the off current is then not defined as the current measured at V_G =0V anymore. It is the lowest current in a transfer curve.

1.3.3 Threshold voltage

The threshold voltage V_T is a parameter that evaluates the amount of traps. More precisely, V_T describes the gate voltage needed in order to turn the transistor on, [17-18] or in other words, where the current starts to flow at an applied V_{SD}.

Ideally, the threshold voltage is expected to be zero, which means current should already start to flow at V_G=0V. [19-21] However, in reality for most cases a non-zero threshold voltage has to be applied in order to get current flowing, due to the trapping sites caused by different reasons.

1.3.4 Two types of measurement

As a basic characterization, two types of measurements have to be performed. One is based on keeping V_{SD} constant while sweeping V_G. As V_G increases, I_{SD} rises as well as a result of more charge carriers being accumulated with growing V_G. The set of values are collected to make a transfer curve (Figure 1.4a). Similarly, if sweeping V_{SD} at various constant V_G, an output curve is recorded (Figure 1.4b).

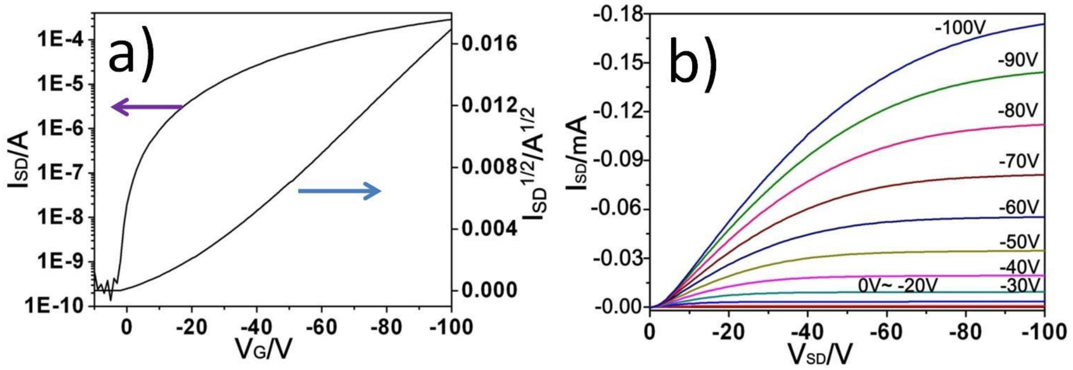

Figure 1.4. Two types of curves in characterizing OFETs: a) transfer and b) output curve.

1.3.5 Device categories

According to different charge carriers, the OFETs can function either as p-type or n-type devices. In p-type OFETs, the major carriers are holes, while in n-type OFETs, the major carriers are electrons. If both holes and electrons can act as carriers, the transistor shows so-called ambipolar behavior.

Actually it has been found that intrinsically, all organic semiconductors should transport both holes and electrons. [25] But in reality, most organic semiconductors tend to transport holes much better than electron because one characteristic feature of semiconductor materials is the strong trapping of electrons, but not holes. [22] As a result, most of the organic semiconductors so far investigated are p-type, which mainly consist of oligomers, pentancene, phthalocyanine, etc. However, n-type semiconductors are also important components in organic electronics, such as p-n junction diodes, complementary circuits, and bipolar transistors. [23-24] There are two reasons why most of them do not show ambipolar behavior.

One reason is that the metals used for source/drain contacts have work functions better suited for injection of holes into the highest occupied molecular orbital (HOMO) of the organic semiconductor than of electrons into the lowest unoccupied molecular orbital (LUMO), which associates with the band levels of the organic materials. Among all the metals, Au is most frequently chosen as source-drain electrodes due to its stability towards air and organic solvents. However, the work function, in other words, the energy required to free an electron from the metal, of Au is high, typically 4.8 to 5.1 eV. [26-27] As a result, the injection of electrons into the LUMO which is responsible for electron transport within the organic semiconductor, is energetically difficult.

Another reason is that for dielectric surface, SiO_2 is most often employed for OFETs. As is known, SiO_2 contains polar silanol groups that trap electrons within the organic semiconductor. [22] Therefore, in most cases, only hole transport could be observed. Proper extinction of these trapping sites by modifications of the SiO_2 surface with self-assembled monolayers such as hexamethyldisilazane (HMDS) or octyltrichlorosilane (OTS) has been proven to be beneficial for n-type OFETs.

1.4 The influencing factors of OFETs performance

To improve the performance of the OFETs, firstly one needs to know the influencing factors of the device performance. As mentioned in the very beginning, the molecular structure of semiconductor determines the intrinsic property of the OFET. While for a given semiconductor, the OFETs performance is determined by optimization of devices, which mainly includes the optimization of morphology/molecular packing and interfaces.

1.4.1 Morphology and molecular order

For a specific semiconductor material, the most important factor that determines the OFET performance is how the molecules arrange with respect to each other. It is of vital significance that the molecules are arranged in a way that the delocalized molecular orbitals can provide sufficient overlap over a large distance connecting source and drain electrodes. By analyzing the X-ray diffraction (XRD) from the organic films, one can infer the molecular organization. It has been proven that charge carrier transport is more efficient along the π-π stacking direction in well-ordered transistor films, in comparison to poorly packed or amorphous films which block the charge transport due to insufficient overlap of the molecular orbitals containing the free charges. [28]

Moreover, charge carrier transport is sensitive to structural defects such as molecular disorder and grain boundaries. In other words, grain boundaries can affect the properties of semiconductors and reduce the charge carrier transport between the electrodes. Therefore, by improving the thin film morphology and elevating the structural order of the molecules, one can improve the corresponding device performance. [28] This principal is applicable for films of both small conjugated molecules and polymers.

Firstly how the morphology and molecular packing influence the device performance of transistors based on small conjugated molecules should be discussed. The molecular order and the extent of crystallinity dominate the device performance. For example, the extend of crystallinity is proven to have a great impact on the OFET performance. [29] It is observed that the charge carrier mobility of further macroscopically ordered and extended crystalline layers is greatly improved compared to that exhibited by the lower ordered films. The results also indicate that the less grain boundaries the film possesses, the better the device performance it exhibites.

In this aspect, one-dimensional (1D) nano/microstructures have attracted increasing attention in recent years because of their unprecedented device performance. Especially, single crystal mircoribbons or microwires are free of molecular disorder and grain boundaries, facilitating directional charge transport and excition diffusion. [10-23] OFETs based on such nano- and micro-sized single crystal ribbons or wires for various small conjugated molecules have been reported to show much higher charge carrier mobility than their corresponding thin film based devices. For example, p-type OFETs based on oligoarene single-crystal microribbons with a performance as high as 2.1 $cm^2V^{-1}s^{-1}$have been reported, a two orders of magnitude improvement compared to the solution processed thin layers of the same compound. [30] Recently, mobilities beyond 2.0 $cm^2V^{-1}s^{-1}$ were observed for both p-type and n-type OFETs based on single crystal ribbons of various small crystalline building blocks. [31-33] Because of their solution processability, polymeric transistors are believed to have more potential applications. For polymers, the charge transport mechanism is slightly different. On one hand, polymers cannot form single crystals due to the self-assembly limitation of the polymer chain, which is a major drawback compared to small conjugated molecules. Instead, polymers typically form polycrystalline films with complex microstructures, such as well packed domains which are separated by grain boundaries. On the other hand, in comparison to small conjugated molecules, polymers possess long conjugated backbones, along which faster charge immigration usually takes place. This is a major advantage of polymers for yielding high charge carrier mobilites, in comparison to small conjugated molecules. [34] A slower motion takes place along the π-π stacking direction. Here, the π-π stacking distance is also very important in determing the charge carrier mobility. Usually solubilising groups are introduced to render polymer sufficient solubility. However, the sterical hindrance of these substituents always leads to an increase in π-π stacking distance. As a result, the charge carrier mobility is determined by both intra-chain transport (along conjugated backbones) and inter-chain transport (along π-π stacking direction).

Although long-range ordered polymer film are highly desirable for high performance OFET devices, some examples of macroscopically low ordered polymer films were found to exhibit remarkably high mobility values above 0.5 cm^2/Vs. In order to further improve the charge carrier mobility, one has to orient polymer backbones along the current flow direction since the limiting factor for device performance is the hopping between the conjugated backbones. This phenomenon has been not only observed for isolated polymer chains, but also in macroscopically oriented thin films. For instance, pre-aligned PTFE or a concentration gradient could induce oriented thin films, for which higher mobilities were detected in the direction of the backbones. The ideal case is that molecules are highly ordered in polymer single fibers. [35]

Hereby, the molecular arrangement of both small molecules and conjugated polymers relies on the tendency of the organic semiconductors to self-assemble. The self-assembly of these semiconductor molecules can be enhanced through the proper fabrication methods. In the following parts of this chapter (1.5), the state of the art of processing techniques for OFETs will be presented.

1.4.2 Importance of the interfaces

It is important to note that the previous theory predicts high density of charges and thus of the charge carrier mobility in the first few nanometers of the active film. [36] This is also verified by the actual experiments. [37-44] Therefore, the conditions of dielectric/organic layer interface, and the molecular arrangement in the first few layers of the film on dielectric surface, are important factors in determining the OFET performance. In this aspect, the control of the molecular order in the first few layers becomes a key issue. Hereby, applying different processing methods, such as dip coating and zone casting, which can induce molecular alignment. Besides, surface treatment is another effective way to align the molecules with their stacking direction parallel to the current flow direction. There are some requirements for the substrates.

Firstly the substrates should be as clean as possible, since any impurity could form traps at the interface. Besides, these dust could also alter the relative energy levels and inhibit the charge carriers transport, thus greatly affecting the charge carrier mobility as well as the on/off ratio. In order to ensure a clean surface, plasma treatment is required to remove dust or organic dirty on the surface.

Here it should be emphasized that various inorganic materials could be employed as gate dielectric layers for OFETs, such as SiO_2, SiNx, Al_2O_3, etc. Among these materials, SiO_2 is most often employed as dielectric surface in OFETs. However, SiO_2 contains polar silanol groups that trap charge carriers, especially electrons within the organic semiconductor. [22] Therefore, the modification of this interface offers a general way to improve carrier transport accordingly. Usually modifications of the SiO_2 surface with self-assembled monolayers such as hexamethyldisilazane (HMDS), [45]octyltrichlorosilane (OTS), [46, 47] as well as other silanes, have been proven to be able to extinct these trapping sites. In most cases, the mobility can be improved obviously since these surface treatments could also lead to favorable molecular orientation. For instance, HMDS treatment was found to be able to promote a lamella-like structure of P3HT with the alkyl chains perpendicular to the substrate, which gave a much higher mobility in comparison to the untreated surface. [38],While OTS treatment was found to have a beneficial effect on forming larger crytal grains and improving order. [48]

1.5 Processing techniques

The molecular organization of organic semiconductor can be clarified based on their molecular structure. Further control of the self-assembly and microstructure evolution of semiconductor is determined by the way how the molecules are processed. Hereby, the commonly employed processing techniques include vacuum deposition, solution-processing technique, and printing techniques, etc, are introduced one by one.

1.5.1 Vacuum Sublimation

Small molecules are commonly deposited via vacuum deposition, which is one of the most frequently used techniques in OFET fabrication. During this process, the organic semiconductor is deposited by sublimation in a chamber under very high vacuum or even ultrahigh vacuum, with a pressure in the range of 10^{-8} to 10^{-6} Torr. [49] Hereby, the substrate conditions e.g. substrate temperature, surface energy, can influence the packing mode and crystal domain sizes. By optimizing the deposition rate and substrate temperature, highly ordered thin films could be obtained.

It is observed that a faster deposition rate leads usually to higher nucleation density, in other words, smaller average grain sizes. Therefore, high charge carrier mobility is usually obtained by slower deposition rate. [49].There are also clear examples of the influence of the deposition temperatures on the thin film morphology. For example, a range of crystallinities could be obtained by evaporating pentence at different temperatures, which could be closely correlated with the resulting device performance. [50] On the other hand, deposition temperature could also influence the size of crystal grains. For instance for copper phthalocyanine (CuPc), when being deposited at different substrates temperatures, its microstructures differ greatly. [51] The film deposited at room temperature consists of small but homogeneously covered crystal grains. With increasing the substrate temperature, the morphology of the film changes from grains to large flat crystals. Such kind of larger flat crystals are far more preferable for charge carrier transport. [38] However, on the other hand, nucleation obtained at high temperature is very sparse. This leads to the large crystals being separated from each other, which has a negative effect on the charge carrier mobility.

Based on this understanding, the influence of vacuum deposition parameters have been systematically studied on a series of benzo[d,d]thieno[3,2-b;4,5-b]dithiophene (BTDT) derivatives. It is found that with increasing the substrate temperature, the grain size also increases. Moreover, smaller but better interconnected crystalline domains were obtained when depositing the molecules at high deposition rate. Interestingly, a compromise between large crystalline domains and sufficiently interconnected grains was achieved by a careful tuning the substrate temperature and deposition rate, thus showing a maximum OFET mobility. [52]

However, vacuum deposition has several disadvantages. Firstly, in comparison to solution processing, it is material consuming for each deposition. Moreover, this method typically yields discontinuous patches due to 3D island growth. [51] Another disadvantage is that vacuum deposition requires sophisticated instrumentation and cannot be employed for polymer film deposition. Despite the disadvantages, this method has already been proven to be an efficient deposition approach for insoluble organic small molecules and oligomers. Up to now, the record OFET mobility has been reported for pentacene films prepared by vacuum deposition, showing a charge carrier mobility as high as 40 cm^2/Vs. [53]

1.5.2 Solution Processing

Solution processing allows large area, easy, fast and low-cost fabrication of OFETs therefore is considered to be the future process in roll-to-roll fabrication of electronic devices. The most commonly used solution deposition methods are drop casting, spin coating, dip coating, zone casting, and ink jet printing. Dip coating and zone casting can be used to align the semiconductor molecules in the thin film from solution, which is highly required for fabricating high performance devices. [54] Therefore, in this section, dip coating and zone casting will be introduced in greater detail than other solution processing methods. In the following, these solution processing methods will be introduced one by one, at the same time pointing out their advantages and disadvantages.

1.5.2.1 Drop casting

Drop-casting is the simplest method among all the solution processing techniques. (Figure 1.5) Hereby, the solution is prepared by dissolving the organic semiconductor molecules in an organic solvent. Droplets of the solution are dropped on the transistor substrate. The solvent is removed from the substrate via evaporation. [55] The evaporation rate can be controlled by choosing different organic solvents. For instance, solvent with higher boiling point can prolong the evaporation, allowing more time for molecules to self-assemble into better ordered films.

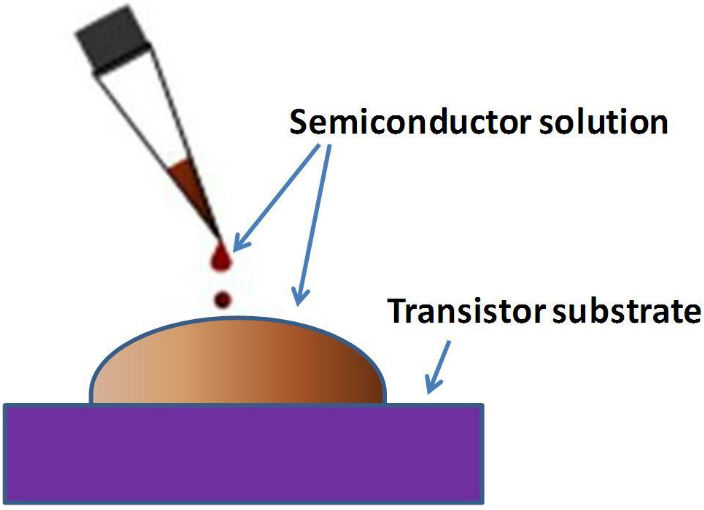

Figure 1.5. Schematic illustration of drop casting.

As a disadvantage, drop casting is dominated by hydrodynamic forces suffering from de-wetting effect which are detrimental for forming long range ordered films and often lead to coffee ring effect. [55] Besides, this usually causes very high surface roughness and is not suitable for the top contact configuration.

1.5.2.2 Spin coating

Spin coating is another simple, most versatile processing method of semiconductor molecules. (Figure 1.6) It is practical for large area and low cost fabrication. Hereby, the solution is firstly deposited on the substrate and then spun at a specific rate and time. [56-57] Similar to drop casting, the solvent is removed from the surface also by evaporation, during the spinning. Here it should be emphasized that the solvent used for spin coating should have a low boiling point, to ensure a quick evaporation during the rapid spinning process. Otherwise, no film can be formed because the whole solution is spread away from the substrate. As a disadvantage, spin coating also could not provide delicate control over the formation of well ordered microstructures because it often leads to badly trapped, poorly ordered films due to high solvent evaporation speed.

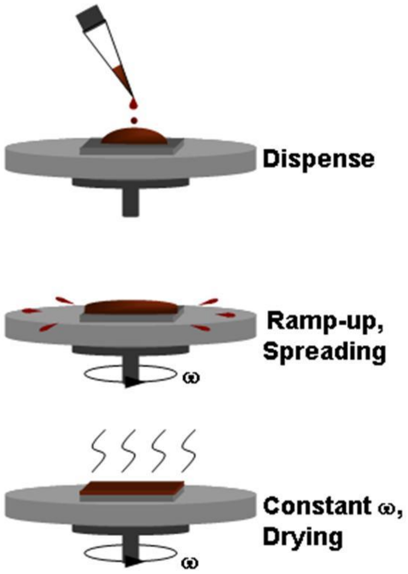

Figure 1.6. Schematic illustration of spin coating. [59]

The microstructure and molecular packing of conjugated molecules on the surface are essential parameters for the device performance. However, these two parameters cannot be well controlled because of the high spinning speed. It is necessary to find alternative processing techniques for efficient solution processing. In this aspect, dip coating and zone casting can allow uniaxially directed self-assembly.

1.5.2.3 Dip coating

Dip coating is a more powerful evaporation-controlled process in comparison to drop casting and spin coating, and is well recognized for aligning the semiconductor molecules in thin films from solution. [58-67]In this process, the substrate is firstly immersed vertically into the solution. Then it is withdrawn at a defined speed, controlled by a high-precision linear motor stage. During this processing, the substrate is moved out of the semiconductor solution, while a meniscus is formed at the substrate–solution interface where the molecules are deposited under the driving force of a concentration gradient. (Figure 1.7) In other words, the pulling velocity of the substrate from the liquid leads to the formation of a meniscus at the substrate-solution interface. Hereby, the molecules can align as a result of the concentration gradient. This method provides a fine control over the evaporation rate of solvent at the contact line, substrate speed, and self-assembly propensity of the molecules. After the substrate is fully moved out of the solution, usually the semiconductor molecules are aligned parallel to the dip coating.

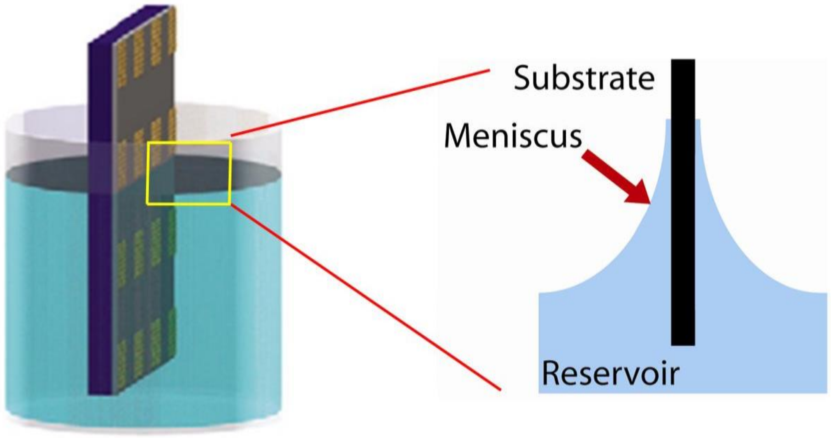

Figure 1.7. Schematic illustration of dip coating [59]

During dip coating, the parameters that influence the self-assembly and film formation includes dip coating rate, the choice of solvents, solution concentration, and solution temperature. These factors have to be optimized individually for each compound. The quality of the dip coated film depends also on the self-assembly behavior of organic semiconductor molecules. However, in many cases it is expectable that well-aligned structures are yielded if crystalline domains or well-defined one dimensional object (fiber, ribbon or needle) are observed simply by drop casting or spin coating.

As a disadvantage, semiconductor molecules are inevitably deposited on both sides of the substrates, which causes unnecessary waste of materials. As another disadvantage, in comparison to drop casting, one cannot apply hydrophobic surface, such as HMDS or OTS treated surface, during dip coating since no film can be obtained on the substrate after dip coating due to the hydrophobic surface repelling the solution when the substrate is withdrawn vertically out of the solution. To solve this problem, weaker hydrophobic treatment should be applied. In spite of the few discussed disadvantages dip coating is a desired processing method for directional alignment and morphology control in device applications. In comparison to the films obtained by drop casting and spin coating, the improved organization by dip coating can result in a greatly improved device performance with much better mobility being achieved for small conjugated molecules by alignment. This will be indicated below for several examples.

Dithieno[2, 3-*d*;2’, 3’-*d*’] benzo[1,2-*b*;4,5-*b*’]dithiophene (DTBDT) shows a OFET charge carrier mobility of 10^{-2} cm^2/Vs after spin-coating (Figure 1.8a).[58] Moreover, crystalline domains emerge in this spin coated film (Figure 1.8b). According to the principles mentioned in the former paragraph, it is predictable that dip coating will further enhance the film morphology and yield directionally oriented structures. Based on this assumption, dip-coating has been applied to improve the transistor performance. As expected, after dip coating, the size of crystalline domains is greatly enlarged (Figure 1.8c). The grain boundaries are minimized, and clearly the charge carrier pathways are oriented between the drain and source electrodes. Under optimized solvent evaporation and dipping rates, highly crystalline domains ranging over several squared millimeters have been obtained. (Figure 1.8c) The structural analysis has indicated a parallel orientation of the π-stacking axis with respect to the substrate. Such an orientation is especially beneficial for transistor applications. Finally, the corresponding devices show an excellent hole mobility as high as 1.7 cm^2/Vs.

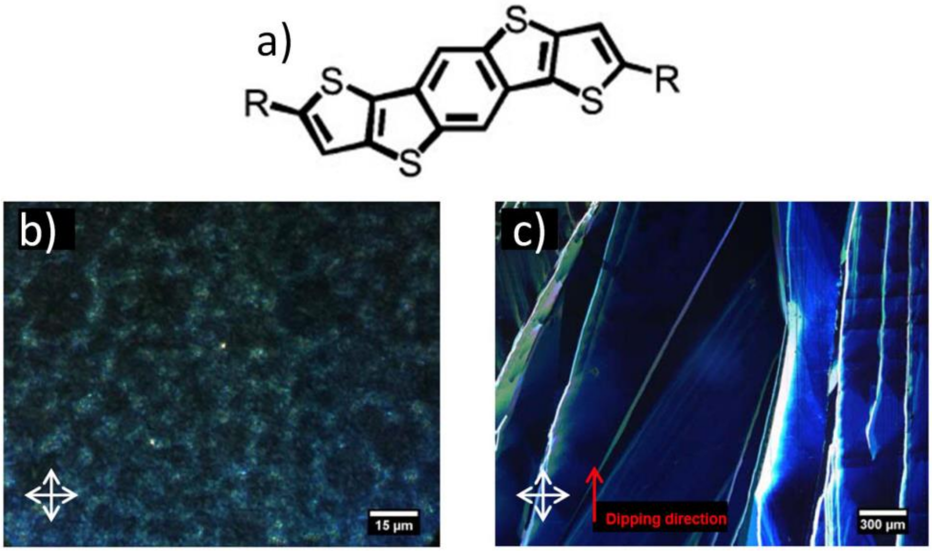

Figure 1.8. a) Chemical structure of the DTBDT; polarized optical microscopy of b) spin coated and c) dip coated film of DTBDT. [58]

Dip coating can also be applied to improve the performance of polymer-based transistors. For example, the cyclopentadithiophene-benzothiadiazole copolymer (CDT-BTZ copolymer, Figure 1.9a; average molecular weight $M_n = 50$ kg/mol using PS/THF standards) was oriented by dip coating from solution. [59] A spin coated film of this polymer gives an OFET mobility of 0.67 cm^2/Vs. However, dip coating significantly enhances this value up to 1.4 cm^2/Vs. GIWAXS measurements performed perpendicular and parallel to the processing direction of the film confirm structural in-plane anisotropy. It is verified that the conjugated polymer backbones are oriented along the dip-coating direction and are arranged with respect to the substrate in an edge-on configuration. AFM is employed to compare the morphologies for films obtained by dip coating and spin coating. As is shown in Figure 1.9b, upon spin-coating, the film texture showed 50 nm large ring-like structures indicating a self-assembly of the macromolecules into circular structures. By contrast, dip-coated films mainly consist of well-aligned, anisotropic fibers (Figure 1.9c).

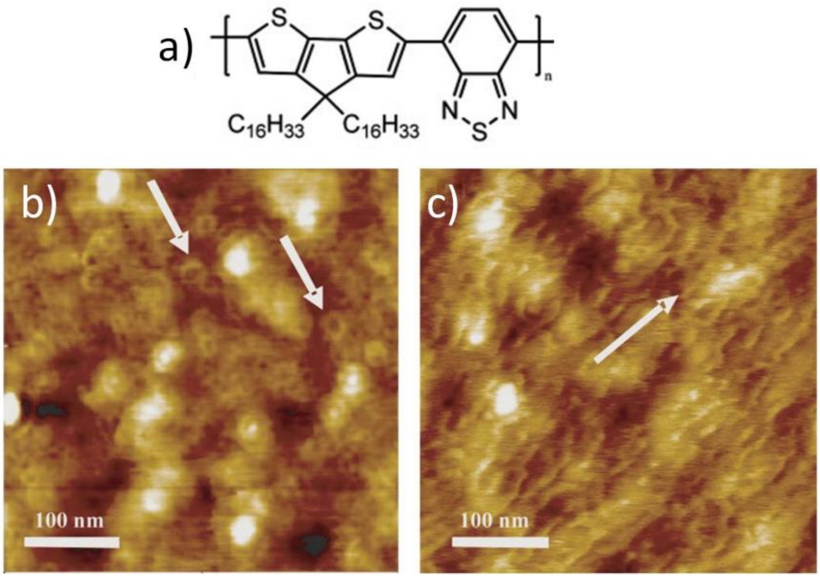

Figure 1.9. a) Chemical structure of CDT-BTZ copolymer. AFM height images of b) spin-coated and c) dip-coated CDT-BTZ copolymer. The arrow in c) indicates the dip-coating direction. The arrows in b) highlight the donut-like structures of spin-coated CDT-BTZ copolymer films. [59]

Recently, researchers devised a novel dip coating procedure performing dip coating at a low speed inside an airtight environment saturated with solvent vapor, in this way reducing the dewetting effect caused by solvent evaporation during dip coating. Actually this is a combination of deposition technique (dip coating) and post processing treatment (solvent vapor annealing, which will be described in greater details in chapter 1.4.2.5) This procedure has been employed for the electron-acceptor [6, 6]-phenyl C61 butyric acid methyl ester (PCBM; Figure 1.10a). [68] Disorded patches on the macroscopic scale appear when processing PCBM by conventional techniques such as spin coating and drop casting. However, by dip coating in solvent vapor atmosphere, crystals were obtained on various substrates such as silicon, gold, and copper, etc. (Figure 1.10c and 1.10d) Their well-defined shape and flatness make PCBM crystals an ideal interface to perform fundamental photophysical studies in electron donor and acceptor blends.

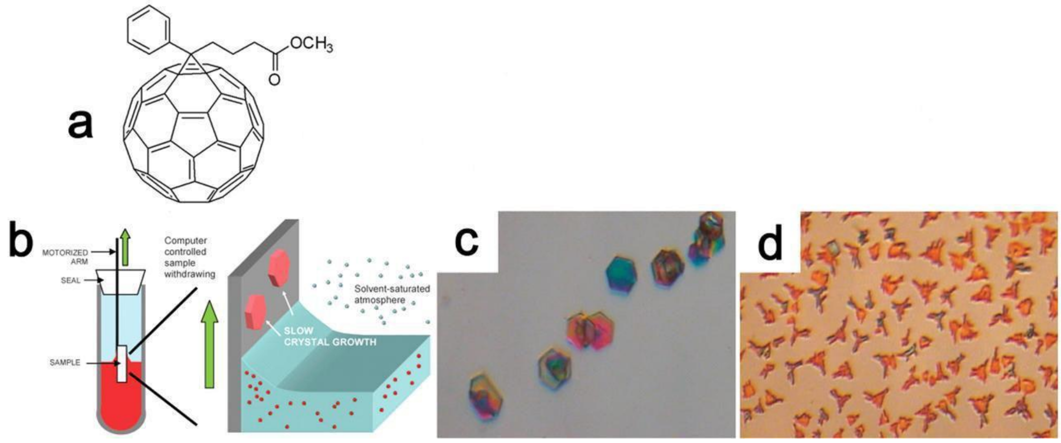

Figure 1.10. a) Molecular structures of PCBM. b) Schematic illustration dip coating process in solvent vapor atmosphere. c, d) OM images of PCBM crystals obtained by dip coating on SiO_2 surface. [68]

1.5.2.4 Zone casting

As mentioned above, besides dip coating, zone casting is another effective approach to control the orientation of conjugated molecules on the substrate. [69-75] This method is based on the surface alignment of ordered nanostructures grown from solution which is cast from a nozzle onto a moving support. In comparison to dip coating, more parameters determine the quality of the film, which include: solution concentration, evaporation rate of the solvent, substrate speed, temperature of both substrate and solution. Like in dip coating, these factors also need to be optimized for each compound individually. Moreover, before starting zone-casting, it is necessary to gain fundamental understanding on the aggregation of the molecules in solution and self-assembly during deposition on a surface.

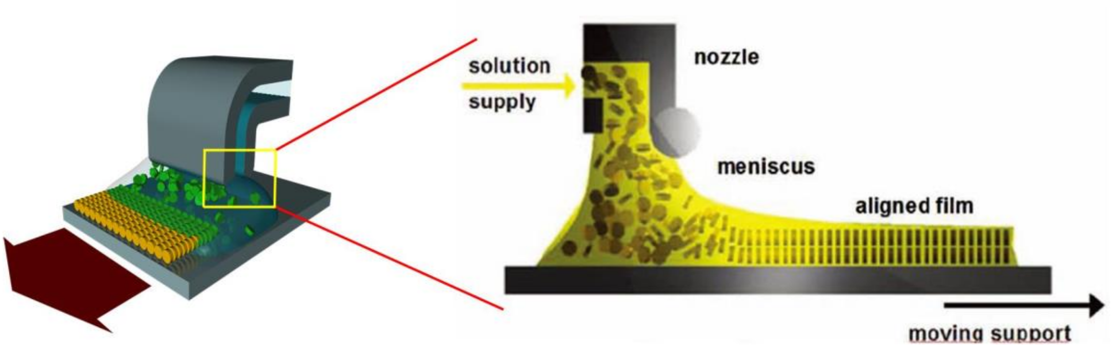

Figure 1.11. Schematic illustration of zone casting. [69]

The principle is quite similar to dip coating. As is presented schematically in Figure 1.11, the principle can be stated as follows: during zone casting, a concentration gradient is established within a defined zone in a meniscus that is formed between the nozzle and the moving support, working as the driving force for the directional growth. Along this meniscus the solvent fraction decreases due to its evaporation until a critical concentration is reached, thereby initiating the nucleation process on the moving support to form an aligned thin layer. Since fresh solution is permanently provided, a large area deposition can be obtained allowing up-scaling of this technology for industrial applications and mass production.

For instance, highly ordered, zone-cast thin layers of a hexadodecyl substituted discotic hexa-*peri*-hexabenzocoronene (HBC) (HBC-C_{12}, Figure 1.12a) were obtained.[69] This molecule shows a strong tendency towards aggregation already in solution. [70] As evidence, a fibrillar network is already formed when this compound is drop-cast on SiO_2 wafer. [70] During zone-casting, the molecules assemble on the surface into pre-aggregates which grow within the processing zone to yield superstructures at the last stage of solvent evaporation. X-ray diffraction (XRD) has revealed a perfect uniaxial long-range orientation of the columnar stacks along the processing direction, displaying individual columns of HBC-C_{12} molecules down to molecular resolution (Figure 1.12b,c).

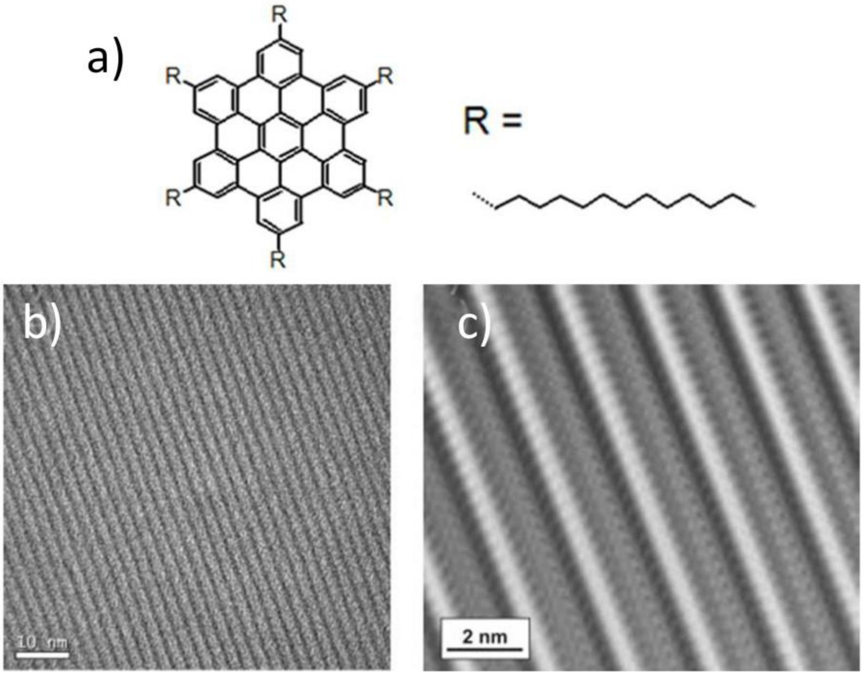

Figure 1.12. a) Chemical structure of the HBC-C_{12}. b) high-resolution transmission electron microscopy of zone-cast of HBC-C_{12} with individual columns oriented in the zone-casting direction, c) filtered inverse FFT (IFFT) image displaying intermolecular periodicity along the columns. [69]

This edge-on arrangement is particularly attractive for applications in FETs. [71-72], which is proven by the comparison of OFETs performance of drop-casting film and zone casting film. Drop-cast FETs of **1** yield charge carrier mobilities of 3×10^{-4} cm^2/Vs,[73] while the oriented layers show significantly higher values up to 10^{-2} cm^2/Vs along the alignment direction, which coincides with the direction of the columnar structures. [69] The mobility measured perpendicularly to the stacks yields values two orders of magnitude lower than the previous ones, confirming a one-dimensional nature of the charge transport along the columns.

As a disadvantage, zone casting is more complicated than dip coating and the optimization is usually difficult and time consuming. Moreover, the concentration changes with the deposition of the solution leading to not completely homogeneous films over large scale.

1.5.2.5 Post processing treatments

It should be emphasized that the semiconductor morphology on the surface can be also improved by post processing treatment, for instance, thermal annealing and solvent vapor annealing. Since device fabrication is typically carried out in air, the films obtained are inevitably affected by unintentional doping and unwanted contamination of the semiconductor layer. Oxygen and solvent residues are considered as major dopings of the transistor. [76]

Thermal annealing is commonly employed to re-assemble molecules to a better order.. Moreover, it has been proven to be an effective route to eliminate the doping and improve the corresponding charge carrier mobility for both small conjugated molecules and conjugated polymers. [76] For instance, effects of thermal annealing in vacuum for OFETs based on small conjugated molecules such as α-sexithienyl and pentence were systematically studied. Annealing at 60 °C for several hours does not provide any effect on device performance. However, increasing the substrate temperature to 90 °C for a few hours, leads to an obvious increase in charge carrier mobility. Thermal annealing could increase the performance of polymer as well. For example, regioregular poly (3-hexylthiophene) (P3HT) exhibits reasonable high performance. Thermal annealing results in significantly improved charge carrier mobility. The improved mobility was attributed to both higher crystalline and better contact between the polymer and electrodes. [77] However, thermal annealing is not suitable for all the conjugated molecules, especially not suitable for transistors using plastic substrates.

Solvent vapor annealing (SVA) is another efficient way to improve the molecular order and thus device performance because solvent vapor has been also proven to be beneficial for the re-assembly of the semiconductor molecules on the surface. Particularly, SVA is more appealing when thermal annealing risks thermal degradation of the organic layers on the dielectric surfaces, since SVA takes place under ambient conditions. Hereby, SVA is based on positioning the deposited film in an airtight container that is saturated with solvent vapors. In comparison to thermal annealing where only the annealing temperature plays an essential role during SVA, one has larger amounts of parameters to tune, such as the choice of solvent with different boiling point and different polarity. For instance, when a perylene diimide (PDI) solution (chloroform as solvent)were deposited onto a SiO_2 surface, only a less-organized, dewetting layer were obtained after the solvent evaporation. [78] When these samples were subjected to a saturated THF vapor atmosphere, macroscopically long fibers were formed on the surface. (Figure 1.13)The reorganization of the PDI molecules on the surface is ascribed to the partial re-solubilization of the deposited layers, in this way allowing the molecules to rearrange into better order.

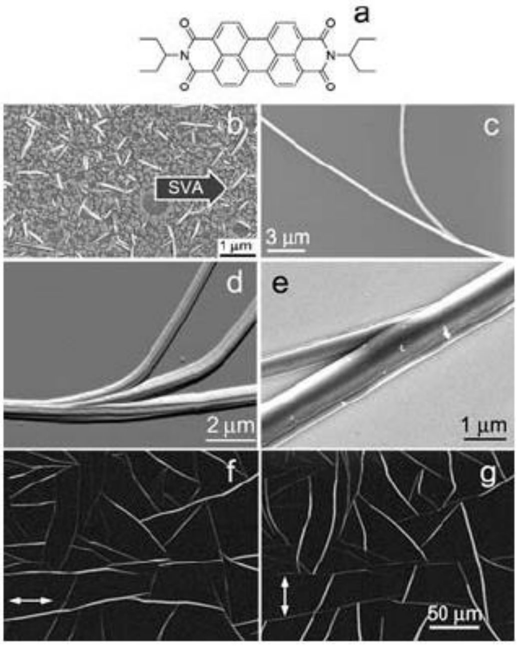

Figure 1.13. a) Chemical structure of the PDI derivative. b) AFM image of PDI nanostructures obtained by spin coating PDI $CHCl_3$ solution on a SiO_2 substrare, c) AFM togography, d) AFM topography gradient, e) SEM image, f) g), PDI fibers obtained after SVA in THF. [78]

Recently, single crystal of dioctylbenzothienobenzothiophene (C8-BTBT, Figure 1.14) were sucessfully fabricated by further combining SVA with a phase-separation method. Hundreds of micronmter long single crystals of C8-BTBT were simultaneously obtained on a polymer dielectric surface. Interestingly, the crystallization procedure was observed at different time periods, which suggests that the self-assembly of the molecules underwent a nucleation-governed procedure to crystallize. AFM scanning the single crystals exhibits a highly uniform width and low top surface roughness. Correspondignly, OFET devices based on the SVA fabricated single crystal gave a p-type mobility as high as 9.1 cm^2/Vs. [31]

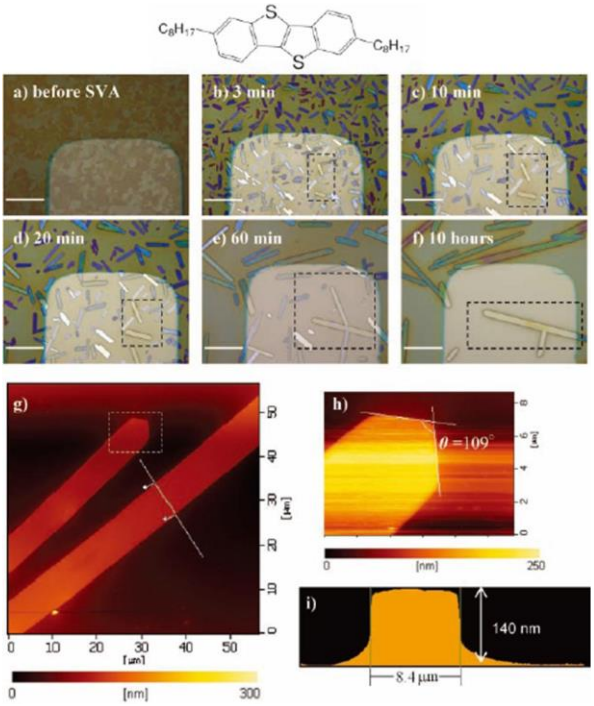

Figure 1.14. a)-f) Optical images of a sample taken from the SVA at different time periods. The sample was put back into the SVA after taking each photo Chemical structure of the PDI derivative. b) AFM image of PDI nanostructures obtained by spin coating PDI CHCl3 solution on a SiO_2 substrare, c) AFM togography, d) AFM topography gradient, e) SEM image, f) g), PDI fibers obtained after SVA in THF. [31]

As a disadvantage, SVA could not rearrange molecules over macroscopic distances, thus requiring a preformation of homogeneous and continuous films. SVA is usually employed to treat the homogeneous films deposited by spin coating or drop casting. For those obtained by drop casting which exhibit macroscopically large aggregations, SVA is not applicable. This limits the applicability of SVA in device fabrication.

1.5.3 Other processing techniques

Besides vacuum deposition and solution processing, it is also necessary to mention Langmuir-Blodgett and printing techniques. The former is known for homogeneous film fabrication and the later is attractive for commercial use.

1.5.3.1 Langmuir-Blodgett (LB)

LB technique has been proven to be an efficient approach to fabricate one or more monolayers of semiconductor molecules. The first requirement is that the semiconductor molecules are not water soluble. During LB process, the solution is deposited on a water surface on which the self-assembly occurs followed by subsequent compressing into a homogenous and continuous film. Afterwards, this monolayer is transferred onto a solid substrate by a dip coating process. This procedure can be repeated to reach a multilayer film arrangement. As a result, a ultrathin and well-ordered thin LB film is formed. Using LB, single molecular monolayers with nearly no defects can be obtained. [79-80] However, as a disadvantage, this technique is generally restricted to amphiphilic molecules, which is not the case for most of the semiconductor materials used in OFETs.

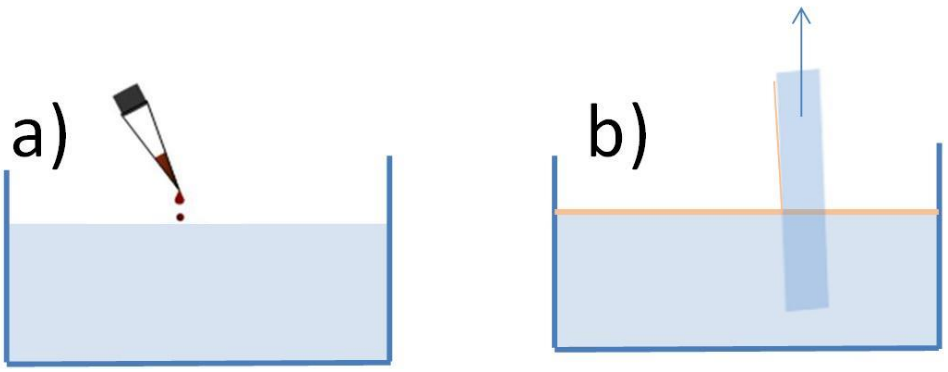

Figure 1.15. Schematic illustration of LB technique. a) Deposition of solution on a water surface. b) Transferring the monolayer onto substrate by dip coating process.

1.5.3.2 Printing techniques

Printing techniques are especially attractive for commercial use since they are faster method in comparison to the dip coating and zone casting. The most known printing methods are ink-jet [81-82] and roll-to-roll. The former one is akin to drop-casting but in a much larger scale. Ink-jet printing is a mature technique initially employed to print pictures and text with high resolution. OTFTs can be printed by this technique as well, simply by replacing conventional inks with semiconductor solution. Hereby, multiple nozzles are employed to deposit droplets onto a substrate, thus processing semiconductor layers in a larger scale.

Roll printing such as screen printing is even faster than ink-jet printing. A specially formulated ink is squeezed through a screen mask onto the substrate surface to form a desired pattern. [83] Hereby, the flexible transistor substrates are printed with the liquid organic semiconductor like newspapers are printed in large rolls. However, the limitation of this technique is the limited feature size it can print. [83]

As another obvious disadvantage, like drop casting, both printing techniques do not allow directional alignment and film morphology control. Therefore, the printing techniques are suitable for the semiconductor molecules which can give high OFET performance without the need for additional orientation.

REFERENCES

[1] A. R. Brown, A. Pomp, C. M. Hart, D. M. de Leeuw, *Science*, **1995**, *270*, 972.

[2] C. J. Drury, C. M. J. Mutsaers, C. M. Hart, M. Matters, D. M. De Leeuw, *Appl. Phys. Lett.* **1998**, *73*, 108.

[3] C. D. Sheraw, L. Zhou, J. R. Huang, D. J. Gundlach, T. N. Jackson, M. G. Kane, I. G. Hill, M. S. Hammond, J. Campi, B. K. Greening, J. Francl, J. West, *Appl. Phys. Lett.* **2002**, *80*, 1088.

[4] L. Zhou, A. Wanga, S.-C. Wu, J. Sun, S. Park, T.-N. Jackson, *Appl. Phys. Lett.* **2006**, *88*, 083502.

[5] P. Mach, S. J. Rodriguez, R. Nortrup, P. Wiltzius, J. A. Rogers, *Appl. Phys. Lett.* **2011**, *78*, 3592.

[6] B. Crone, A. Dodabalapur, Y. -Y. Lin, R. . Filas, Z. Bao, A. LaDuca, R. Sarpeshkar, H. E. Katz, W. Li, *Nature*, **2000**, *403*, 521.

[7] J. A. Roger, Z. Bao, *J. Polym. Sci. Part A: Polym. Chem.* **2001**, *40*, 3327.

[8] H. Klauk, M. Halik U. Zschieschang, F. Eder, D. Rohde, G. Schmid, C. Dehm, IEEE Trans. *Electron Devices*, **2005**, *52*, 618.

[9] Y. Watanabe, K. Kudo, *Appl. Phys. Lett.* **2005**, *87*, 223505.

[10] H. Sirringhaus, M. Ando, *MRS Bulletin* **2008**, *33*, 676.

[11] A. Ruiz, A. Papadimitratos, A. C. Mayer, G. G. Malliaras, *Adv. Mater.* **2005**, *17*, 1795.

[12] M. S.A. Abdou, F. P. Orfino, Y. Son, S. Holdcroft, *J. Am. Chem. Soc.* **1997**, *119*, 4518.

[13] E. J. Meijer, C. Detcheverry, P. J. Baesjou, E. Van Veenendaal, D. M. de Leeuw, T. M. Klapwijk, *J. Appl. Phys.* **2003**, *93*, 4831.

[14] S. Hoshino, M. Yoshida, S. Uemura, T. Kodzasa, N. Takada, T. Kamata, K. Yase, *J. Appl. Phys.* **2004**, *95*, 5088.

[15] T. P. I. Saragi, T. Fuhrmann-Lieker, J. Salbeck, *Synth. Met.* **2005**, *148*, 267.

[16] W. L. Kalb, K. Mattenberger, B. Batlogg, *Phys. Rev.* **B 2008**, *78*, 035334.

[17] G. Horowitz, *Adv. Mater***. 1996**, *8*, 177.

[18] G. Horowitz, *J. Mater. Chem.* **1999**, *9*, 2021.

[19] G. Horowitz, R. Hajlaoui, H. Bouchriha, R. Bourguiga, M. Hajlaoui, *Adv. Mater.* **1998**, *10*, 923.

[20] R. Schroeder, L. A. Majewski, M. Grell, *Appl. Phys. Lett.* **2003**, *83*, 3201.

[21] E. J. Meijer, C. Tanase, P. W. M. Blom, E. Van Veenendaal, B. H. Huisman, D. M. de Leeuw, T. M. Klapwijk, *Appl. Phys. Lett.* **2002**, *80*, 3838.

[22] L. L. Chua, J. Zaumseil, J. -F. Chang, E. C. -W. Ou, P. K. -H. Ho, H. Sirringhaus, R. H. Friend *Nature*, **2005**, *434*, 194.

[23] Z. Bao, *Adv. Mater.* **2000**, *12*, 227.

[24]B. Q. Xu, X. Y. Xiao, X. M. Yang, L. Zang, N. J. Tao, *J. Am. Chem. Soc.* **2005**, *127*, 2386.

[25] E. J. Meijer, D. M. de Leeuw, S. Setayesh, E. van Veenendaal, B. H. Huisman, P. W. M. Blom, J. C. Hummelen, U. Scherf, T. M. Klapwijk, *Nat. Mater.* **2003**, *2*, 678.

[26] N. Koch, A. Kahn, J. Ghijsen, J. -J. Pireaux, J. Schwartz, *Appl. Phys. Lett.* **2003**, *82*, 1532102.

[27] H. Ishii, K. Sugiyama, E. Ito, K. Seki, *Adv. Mater.* **1999**, *11*, 605.

[28] M. M. Torrent, C. Rovira, Chem. Rev. 2011, 111, 4833..

[29] C. D. Dimitrakopoulos, D. J. Mascaro, *IBM J. Rev. Dev.* **2001**, *45*, 11.

[30] Y. Zhou, T. Lei, L. Wang, J. Pei, Y. Cao, J. Wang, *Adv. Mater.* **2010**, *22*, 1484.

[31] C. Liu , T. Minari , X. Lu , A. Kumatani , K. Takimiya , K. Tsukagoshi, *Adv. Mater.*, **2011**, *23*, 523.

[32] W. Jiang, Y. Zhou, H. Geng, S. Jiang, S. Yan, W. Hu, Z. Wang, Z. Shuai, J. Pei, *J. Am. Chem. Soc.* **2011**, *133*, 11.

[33] Md. M. Islam, S. Pola, Y. T. Tao, *Chem. Commun.* **2011**, *47*, 6356-6358.

[34] P. Prins, F. C. Grozema, J. M. Schins, S. Patil, U. Scherf, L. D. A. Siebbeles, *Phys. Rev. Lett.* **2006**, *96*, 146601.

[35] X. L. Xiao, Z. B. Wang, Z. J. Hu, T. B. He, *J. Phys. Chem. B* **2010**, *114*, 7452.

[36] C. Tanase, E. J. Meijer, P. W. M. Blom, D. M. d. Leeuw, *Org. Electron.* **2003**, *4*, 33.

[37] A. Dodabalapur, L. Torsi, H. Katz, *Science* **1995**, *268*, 270.

[38] H. Sirringhaus, P. J. Brown, R. H. Friend, M. M. Nielsen, K. Bechgaard, B. M. W. Langewvld-Voss, A. J. H. Spiering, R. A. J. Janssen, E. W. Meijer, P. Herwig, D. M. de Leeuw, *Nature* **1999**, *401*, 685.

[39] K. Xiao, Y.Q. Liu, X. B. Huang, Y. Xu, G. Yu, D. B. Zhu, *J. Phys. Chem. B* **2003**, *107*, 9226.

[40] J. Locklin, K. Shino, K. Onishi, F. Kaneko, Z. N. Bao, R. C. Advincula, *Chem. Mater*. **2003**,*15*, 1404.

[41] F. Dinelli, M. Murgia, P. Levy, M. Cavallini, F. Biscarini, D. M. de Leeuw, *Phys. Rev. Lett.* **2004**, *92*, 116802.

[42] A. Ruiz, A. Papadimitratos, A. C. Mayer, G. G. Malliaras, *Adv. Mater.* **2005**, *17*, 1795.

[43] J. Huang, J. Sun, H. E. Katz, *Adv. Mater.* **2008**, *20*, 2567.

[44] S. G. J. Mathijssen, E. C. P. Smits, P. A.v. Hal, H. J. Wondergem, S. A. Ponomarenko, A. Moser, R. Resel, P. A. Bobbert, M. Kemerink, R. A. J. Janssen, D. M. D. Leeuw, *Nature Nanotech.* **2009**, *4*, 674.

[45] H. Sirringhaus, N. Tessler, R. H. Friend, *Science*, **1998**, *280*, 1741.

[46] M. Shtein, J. Mapel, J. B. Benziger, S. R. Forrest, *Appl. Phys. Lett.* **2002**, *81*, 4383.

[47] J. Lee, K. Kim, J. H. Kim, S. Ima, *Appl. Phys. Lett.* **2003**, *82*, 4171.

[48] H. Klauk, D. J. Gundlach, J. A. Nichols, C. D. Sheraw, M. Bonse, T. N. Jackson, *Solid State Technol.* **2000**, *43*, 63.

[49] M. M. Ling, Z. Bao, *Chem. Mater.* **2004**, *16*, 4824.

[50] C. D. Dimitrakopoulos, D. J. Mascaro, *IBM J. Rev. Dev.* **2001**, *45*, 11.

[51] X. Xiao, Y. Q. Liu, G. Yui, D. B. Zhu, *Appl. Phys. A*, **2003**, *77*, 367.

[52] J. Youn, M. Chen, Y. Liang, H. Huang, R. Ponce Oritz, C. Kim, C. Stern, T. Hu, L. Chen, J. Yan, A. Facchetti, T. Marks, *J. Chem. Mater.* **2010**, *22*, 5031.

[53] M. Yamagishi, Y. Tominari, R. Hirahara, Y. Nakazawa, T. Nishikawa, T. Kawase, T. Shimoda, S. Ogawa, *Appl. Phys. Lett.* **2007**, *90*, 102120.

[54] G. D. Luca, W. Pisula, D. Credgington, E. Treossi, O. Fenwick, G. M. Lazzerini, R. Dabirian, E. Orgiu, A. Liscio, V. Palermo,. K. Müllen,. F. Cacialli, P. Samorì, *Adv. Funct. Mater.* **2011**, *21*, 1279.

[55] V. Palermo, P. Samorì, *Angew. Chem. Int. Ed.* **2007**, *46*, 4428.

[56] V. Biju, M. Micic, D. Hu, H. P. Lu, *J. Am. Chem. Soc.* **2004**, *126*, 9374.

[57] H. L. Yip, H. Ma, A. K. Y. Jen, J. C. Dong, B. A. Parviz, *J. Am. Chem. Soc.* **2006**, *128*, 5672.

[58] P. Gao, D. Beckmann, H. N. Tsao, X. Feng, V. Enkelmann, M. Baumgarten, W. Pisula, K. Müllen, *Adv. Mater.* **2009**, *21*, 213.

[59] H. N. Tsao, D. Cho, J. W. Andreasen, A. Rouhanipour, D. W. Breiby, W. Pisula, K. Müllen, *Adv. Mater.* **2009**, *21*, 209.

[60] N. L. Liu, Y. Zhou, L. Wang, J. B. Peng, J. Wang, J. Pei, Y. Cao, *Langmuir* **2009**, *25*, 665.

[61] G. Wang, J. Swensen, D. Moses, A. J. Heeger, *J. Appl. Phys.* **2003**, *93*, 6137.

[62] A. L. Briseno, J. Aizenberg, Y. Han, R. A. Penkala, H. Moon, A. J. Lovinger, C. Kloc, Z. Bao, *J. Am. Chem. Soc.* **2005**, *127*, 12164.

[63] R. van. Hameren, P. Schon, A. M. van. Buul, J. Hoogboom, S. V. Lazarenko, J. W. Gerritsen, H. Engelkamp, P. C. M. Christianen, H. A. Heus, J. C. Maan, T. Rasing, S. Speller, A. E. Rowan, J. A. A. W. Elemans, R. J. M. Nolte, *Science* **2006**, *314*, 1433.

[64] J. X. Huang, R. Fan, S. Connor, P. D. Yang, *Angew.Chem., Int. Ed.* **2007**, *46*, 2414.

[65] Y. Tong, Q. Tang, H. T. Lemke, K. Moth-Poulsen, F. Westerlund, P. Hammershøj, K. Bechgaard, W. Hu, T. Bjørnholm, *Langmuir* **2010**, *26*, 1130.

[66] R. Dabirian, X. L. Feng, L. Ortolani, A. Liscio, V. Morandi, K. Müllen, P. Samorì, V. Palermo, *Phys. Chem. Chem. Phys.* **2010**, *12*, 4473.

[67] L. Li, P. Gao, K. C. Schuermann, S. Ostendorp, W. Wang, C. Du, Y. Lei, H. Fuchs, L. DeCola, K. Müllen, L. Chi, *J. Am. Chem. Soc.* **2010**, *132*, 8807.

[68] R. Dabirian, X. Feng, L. Ortolani, A. Liscio, V. Morandi, K. Müllen, P. Samorì, V. Palermo, *PCCP* **2010**, *12*, 4473.

[69] W. Pisula, A. Menon, M. Stepputat, I. Lieberwirth, U. Kolb, A. Tracz, H. Sirringhaus, T. Pakula, K. Müllen, *Adv. Mater.* **2005**, *17*, 684.

[70] M. Kastler, W. Pisula, D. Wasserfallen, T. Pakula, K. Müllen, *J. Am. Chem. Soc.* **2005**, *127*, 4286.

[71] D. W. Breiby, O. Bunk, W. Pisula, T. I. Sølling, A. Tracz, T. Pakula, K. Müllen, M. M. Nielsen, *J. Am. Chem. Soc.* **2005**, *127*, 11288.

[72] D. W. Breiby, F. Hansteen, W. Pisula, O. Bunk, U. Kolb, J. W. Andreasen, K. Müllen, M. M. Nielsen, *J. Phys. Chem. B* **2005**, *109*, 22319.

[73] H. N. Tsao, H. J. Räder, W. Pisula, A. Rouhanipour, K. Müllen, *Phys. Status Solidi A* **2008**, *205*, 421.

[74] A. Tracz, J. K. Jeszka, M. D. Watson, W. Pisula, K. Müllen, T. Pakula, *J. Am. Chem. Soc.* **2003**, *125*, 1682.

[75] J. Piris, M. G. Debije, N. Stutzmann, B. W. Laursen, W. Pisula, M. D. Watson, T. Bjørnholm, K. Müllen, J. M. Warman, *Adv. Funct. Mater.* **2004**, *14*, 1053.

[76] C. Vaterlein, B. Ziegler, W. Gebauer, H. Neureiter, M. Stoldt, M. S. Weaver, P. Bauerle, M. Sokolowski, D. D. C. Bradley, E. Umbach, *Synth. Met.* **1996**, *76*, 133.

[77] S. Cho, K. Lee, *J. App. Phys.* **2006**, *100*, 114503.

[78] G. De Luca, A. Liscio, P. Maccagnani, F. Nolde, V. Palermo, K. Mullen, P. Samori, *Adv. Funct. Mater.* **2007**, *17*, 3791.

[79] K. Xiao, Y.Q. Liu, X. B. Huang, Y. Xu, G. Yu, D. B. Zhu, *J. Phys. Chem. B* **2003**, *107*, 9226.

[80] S. Fabiano, C. Musumeci, Z. Chen, A. Scandurra, H. Wang, Y. Loo, A. Facchetti, B. Pignataro, *Adv. Mater.*, **2012**, *24*, 951.

[81] J. Z. Wang, Z. H. Zheng, H. W. Li, W. T. S. Huck, H. Sirringhaus, *Nat. Mater.* **2004**, *3*, 171.

[82] K. E. Paul, W S. Wong, S. E. Ready, R. A. Street, *Appl. Phys. Lett.* **2003**, *83*, 2070.

[83] Z. Bao, Y. Feng, A. Dodabalapur, V. R. Raju, A. J. Lovinger, *Chem. Mater.* **1997**, *9*, 1299.

.

Chapter 2.

Motivation

Although the device performance based on organic materials is comparable of that based on amorphous silicon, it is still far from satisfactory for many applications which require much higher performance, for instance high complexity circuits. In recent years, an equivalent focus in research is now put on fabrication technologies, as well as on the design of novel chemical structures. The motivation of this work is to further enhance the device performance of organic field-effect transistors by elevating the structural order of the conjugated molecules. Fulfilling this goal relies on a more fundamental understanding of the influence of the film microstructure on the performance. Therefore, how the processing methods and processing parameters influence the microstructure evolution should be firstly clarified. In this thesis, I will focus on the following aspects.

2.1 Fabrication of one-dimensional (1D) fibers/crystals

Based on the influencing factors of the device performance described in chapter 1.3, to achieve pronounced device performance it is of vital significance that the conjugated molecules are arranged in a way that the delocalized molecular orbitals can provide sufficient overlap over a large distance connecting source and drain electrodes, so that the current can flow unhindered. Therefore, one of our strategies to greatly improve the charge carrier mobility is by further elevating the structural order of the conjugated molecules. The number of defects can be decreased by increasing molecular order or reducing the distance between source drain electrodes. Hereby, I focus on exploiting the self-assembly of conjugated molecules to create defect-free, highly ordered objects. One-dimensional (1D) organic mesoscopic fibers/crystals are expected to significantly enhance the charge carrier transport as a result of strong intermolecular coupling between closely packed molecules and of a lower density of structural defects, facilitating directional charge transport and excition diffusion. Therefore, in this thesis, I will introduce the fabrication of OFETs based on 1D single crystal microribbons/fibers.

But before we consider fabricating such kind of devices, one important point has to be clarified: how to control the self-assembly of conjugated molecules into such 1D objects which includes the range of several tens of nanometers up to few micrometers. So far, it is still a challenge to grow organic single crystal ribbons and fibers via conventional solution processing techniques directly on the substrate and to incorporate them into transistors. Therefore, designing a novel and versatile solution processing method is required, thus pointing out one important motivation in the following chapter 2.2.

2.2 Design of novel processing method

As a disadvantage, conventional techniques such as drop casting and spin coating, involve a step in which the solvent is removed from the surface by evaporation, a kinetically controlled phenomenon. After evaporation, the conjugated molecules still remain in a disordered arrangement due to the effect of surface tension forces (primarily dewetting), which tends to favor the formation of macroscopically poor patches at surfaces. The strongest impact over the mesoscopic self-assembly and microstructure is achieved directly during solvent evapoation. Therefore, in this work, I will introduce a solution processing method, termed as solvent vapor diffusion (SVD), which permits a modification of the self-assembly of conjugated molecules on the surface directly during solvent evaporation. In comparison to conventional techniques, larger variety of processing parameters that can be tuned during SVD, such as surface energy and solvent polarity in the solution and vapor open the opportunity to fine balance dewetting effects and intermolecular forces, including solvent-molecule, solvent-substrate, and molecule-substrate interactions in order to achieve the desired microstructure and molecular organization on the surface.

Particularly, SVD is necessary when conventional solution processing techniques can not generate the desired microstructure and molecular organization on the surface. As an example, SVD is especially effective to tune the self-assembly of conjugated molecules with electron donor (D) and electron acceptor (A) units, which have recently revealed potential for applications in both organic solar cells and OFETs. For practical use in organic photovoltaics it is well recognized as a successful strategy to control the phase separation at different scales in electron acceptor–donor blends. Recently, an alternative strategy to obtain nanosegregated D-A domains can be accomplished by using D-A dyads as pre-configured functional building blocks to be deposited directly from solution. However, usually disordered aggregations can exist after being processed by conventional techniques. SVD is expected to enhance the self-assembly of D-A conjugated molecules and finally lead to well ordered molecular organization. In this thesis, we discuss how SVD allows a delicate control over the microstructure of conjugated molecules on the following examples:

In chapter 3, SVD assisted self-assembly and microstructure formation from solution is demonstrated on the example of a D-A dyad composed of covalently bonded hexa-*peri*-hexabenzocoronene (HBC) as donor and perylene diimide (PDI) as acceptor. This covalently linked HBC-PDI shows great potential for controlling the supramolecular ordering and phase separation at the nanometer scale. Previously, it was observed that no well-ordered thin films were achieved after processing HBC-PDI by conventional techniques. SVD is the only method that can create highly ordered fibrous structures for the HBC-PDI. More detailed study is described in chapter 3.

In chapter 1.5.2.3, I introduced the previous work in our group that OFETs based on dithieno[2, 3-*d*;2', 3'-*d*'] benzo[1,2-*b*;4,5-*b*']dithiophene –DTBDT crystalline thin films were fabricated, exhibiting average hole mobilities of up to 1.0 $cm^2V^{-1}s^{-1}$. It is anticipated that this is not the ultimate device performance because grain boundaries even in uniaxially oriented thin films affect the properties of semiconductors and reduce the charge carrier transport between the electrodes. As a result, higher hole mobilities can be achieved by further improving the structural order of the molecules for instance in single crystal ribbons. Therefore, in chapter 4, I focus on directly fabricating single crystal ribbons of DTBDT on SiO_2 surface by SVD and studying their corresponding device performance in OFETs. In chapter 1.5.2.3, I described that a cyclopentadithiophene-benzothiadiazole copolymer (CDT-BTZ copolymer) film gave an OFET mobility as high as 1.4 cm^2/Vs after dip coating. How to further improve the charge carrier mobility? It is recognized that the limiting factor for the bulk electronic properties is the hopping between the conjugated backbones. Therefore one effective way is to improve the overall crystallinity and molecular order by controlling the self-assembly of CDT-BTZ copolymer into highly ordered copolymer fibers. In chapter 5, I focus on fabricating high mobility CDT-BTZ single fiber OFETs by SVD to reach high molecular order and pronounced alignment.

2.3 Probing the role of first monolayer in conjugated polymers

The previous theory predicted that high density of charges and thus of the charge carrier mobility occurred in the first few nanometers of the active film. Therefore the prerequisite for enhancing the OFETs device performance is to control the structural order of the conjugated molecules in the first few layers. However, it is still challenging to fabricate conjugated molecules into one single monolayer and its subsequent layers directly on the surface by solution processing. For small conjugated molecules, it has already been proven that the main charge carrier transport in transistors occurs in few molecular layers near the dielectric surface. By contrast, the solution processing of conjugated polymers into one single monolayer and its subsequent layers directly on the surface in an OFET channel is so far rarely reported. Especially, technical questions concerning a precise bottom-up solution growth of conjugated polymers from monolayer to multilayer still need to be answered. This would allow a fundamental study of the role of the first monolayer on the evolution of the bulk polymer microstructure and the charge carrier transport in the transistor. In chapter 6 and chapter 7, well-known high performance p-type conjugated polymer Poly (2,5-bis(3-alkylthiophen-2-yl) thieno[3,2-b]thiophene) PBTTT and n-type conjugated polymer poly{[*N* , *N* ′ -bis(2-octyldodecyl) -naphthalene-1,4, 5,8-bis(dicarboximide)-2,6-diyl]-*alt*-5,5′- (2,2′-bithiophene)}, P(NDI2OD-T2) are chosen for the study.

2.4 Importance of surface roughness

For OFETs based on solution-processed thin films, silane treatment is usually used to modify the dielectric surface for better molecular order and improved charge carrier mobility. On the other hand, silane treatment is detrimental to layer formation because the hydrophobic surface repels the organic solvents, resulting in no film formation. Especially for dip coating and zone casting, which are well recognized as effective ways to align thin films, SiO_2 without silane treatment is typically employed to exclude the hydrophobicity of the silane treatment. Hereby, surface roughness becomes the essential factor in determing the microstructure evolution and their corresponding performance.

Although it was reported that increased dielectric surface roughness contributed to the decrease of mobility for the thin films grown by vacuum deposition, the influence of surface roughness on solution-processed ultra thin layers are still poorly understood. In chapter 8, I will downscale the semiconductor film into monolayer scale on substrates with different surface roughness by solution processing, to get a fundamental understanding of the role that surface roughness plays in determining the microstructure evolution and device performance. To fulfill this goal, in chapter 8, well-known n-type N,N’-bis(n-octyl)-(1,7:1,6)-dicyanoperylene-3,4:9,10-bis (dicarboximide)(PDI8-CN_2) is chosen for the study.

2.5 Materials

Self-assembly of semiconductor materials is highly dependent on the purity, substituents of small conjugated molecules, as well as molecular weight, and dispersity of conjugated polymers. Therefore it is of vital importance to specify these information whenever studying their self-assembly. Hereby, all the materials used in this thesis are either provided by my colleagues or purchased from companies. Details about synthesis, yield, and dispersity are stated as follows:

2.5.1 HBC-PDI

In chapter 3, D-A dyad composed of covalently bonded hexa-*peri*-hexabenzocoronene (HBC) as donor and perylene diimide (PDI) as acceptor, was synthesized and provided by Dr. Lukas Dössel. [1] HBC-PDI exhibited excellent solubility in common organic solvents such as THF, chloroform, cyclohexane, toluene, chlorobenzene, etc. and this allowed for easy purification with recycling GPC, yielding 86% of a dark red solid. [1]

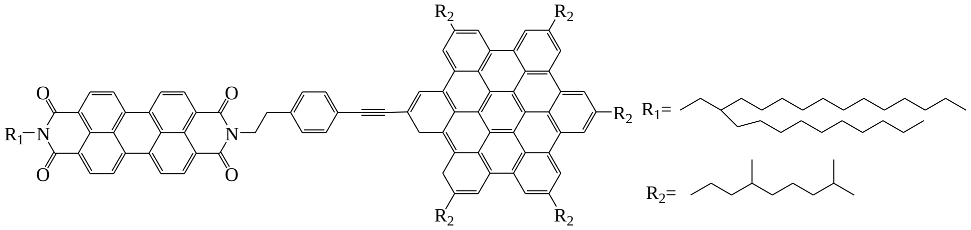

Scheme 2.1. Molecular structure of **HBC-PDI**.

2.5.2 DTBDT

In Chapter 4, dithieno[2, 3-*d*;2’, 3’-*d*’]benzo[1,2-*b*;4,5-*b*’]dithiophene was synthesized and provided my Dr. Peng Gao. DTBDT was obtained in good yields of 93%.” [2]

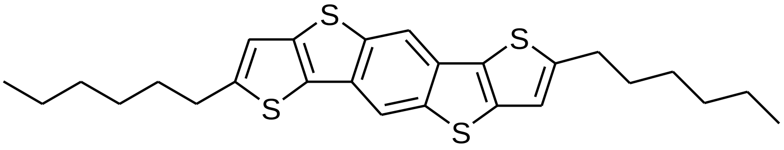

Scheme 2.2. Molecular structures of **DTBDT**.

2.5.3. CDT-BTZ copolymer

In chapter 5, cyclopentadithiophene-benzothiadiazole copolymer (CDT-BTZ) was synthesized and provided by Dr. Don Cho (Mn = 50K using PS/THF standards) and Filex Henkel (Mn = 28K using PS/THF standards).

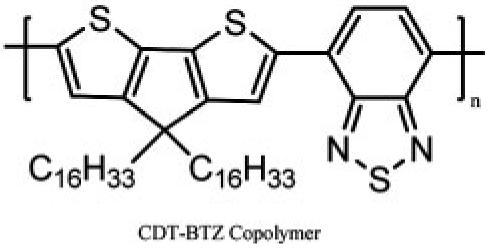

Scheme 2.3. Molecular structures of **CDT-BTZ**. [3, 4]

2.5.4. PBTTT polymer

In chapter 6, p-type conjugated polymer Poly (2,5-bis(3-alkylthiophen-2-yl) thieno[3,2-b]thiophene) PBTTT (Mw=28K by GPC against polystyrene standards, with a dispersity of 2.5) was purchased from Solarmer Material Inc. The synthesis part was described in detail in literature. [5]

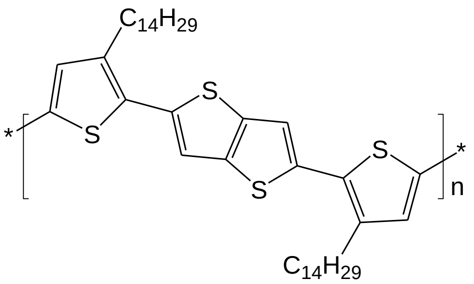

Scheme 2.4. Molecular structures of **PBTTT**. [5]

2.5.5. P(NDI2OD-T2) polymer

In chapter 7, n-type conjugated polymer poly{[*N*,*N*′-bis(2-octyldodecyl)-naphthalene-1,4,5,8-bis(dicarboximide)-2,6-diyl]-*alt*-5,5′-(2,2′-bithiophene)}, (**(P(NDI2OD-T2)**, Scheme 1) was purchased from Polyera. (ActivInk N2200 from Polyera Corporation)

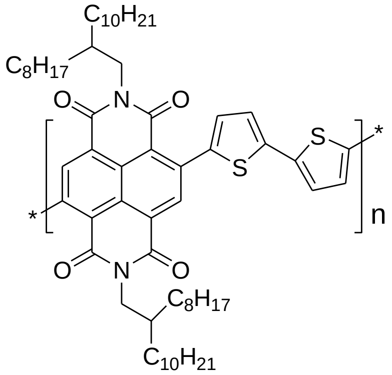

Scheme 2.5. Molecular structures of **P(NDI2OD-T2)**. [6]

2.5.6. PDI8-CN2

In chapter 8, n-type semiconductor N,N'-bis(n-octyl)- (1,7:1,6)-dicyanoperylene-3,4:9,10-bis(dicarboximide) (PDI8-CN_2, ActivInk N1200 was purchased from Polyera Corporation)

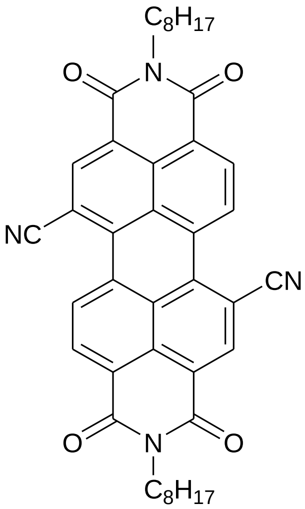

Scheme 2.6. Molecular structures of **PDI8-CN_2.** [7]

REFERENCES

[1] L. Dȍssel, V. Kamm, I. Howard, F. Laquai, W. Pisula, X. Feng, C. Li, M. Takase, T. Kudernac, S. De Feyter, K. Mϋllen, *J. Am. Chem. Soc.* **2012**, *134*, 5876.

[2] P. Gao, D. Beckmann, H. N. Tsao, X. Feng, V. Enkelmann, M. Baumgarten, W. Pisula, K. Müllen, *Adv. Mater.*, **2009**, *21*, 213.

[3] M. Zhang, H. N. Tsao, W. Pisula, C. Yang, A. K. Mishra, K. Mullen, *J. Am. Chem. Soc.* **2007**, *129*, 3472.

[4] M. Zhang, H. N. Tsao, W. Pisula, C. Yang, A. K. Mishra, K. Mullen, *J. Am. Chem. Soc.* **2007**, *129*, 3472.

[5] I. Mcculloch, M. Heeney, C. Bailey, K. Genevicius, I. Macdonald, M. Shkunov, D. Sparrowe, S. Tierney, R. Wagner, W. Zhang, M. L. Chabinyc, J. R. Kline, M. D. Mcgehee, M. F. Toney, *Nature Mater.* **2006**, *5*, 328.

[6] H. Yan, Z. Chen, Y. Zheng, C. Newman, J. R. Quinn, F. Dötz, M. Kastler and A. Facchetti, *Nature*, **2009**, *457*, 679.

[7] B. A. Jones, *Angew. Chem. Int. Ed.* **2004**, *43*, 6363.

Chapter 3.

Self-Assembly and Microstructure Control of Hexa-*peri*-hexabenzocoronene - Perylene Diimide Dyad by Solvent Vapor Diffusion

3.1 Introduction

As mentioned in chapter 1.4, self-assembly of organic semiconductors on the surface into well-defined microstructures, including the range of several tens of nanometers up to few micrometers, is a subject of continuous interest in the field of organic field-effect transistors (OFETs).[1-11] It is also demonstrated in chapter 1.5 that the simplest and most versatile processing method is based on solution deposition including drop-casting[12], spin-coating[13-14] and dip-coating[15-18]. Unfortunately, all these conventional techniques suffer from dewetting effects caused by evaporation which is the kinetic for removing the solvent before forming a film on the surface [19-21]. As a result, coffee ring formation and macroscopically poor aggregations are usually observed at surfaces after solvent evaporation. [12] Overcoming the dewetting effects relies on developing new solution processing methods. Before designing such a method, a fundamental understanding of the influencing factors is warranted.

In general, the molecular self-assembly from solution is determined by a complex combination of interactions between molecule-molecule, molecule-substrate, molecule-solvent, and substrate-solvent.[12] To obtain a control over the microstructure, a subtle balance of all these interactions involved must be achieved.

Alongside, various post-treatment procedures have been widely employed to improve molecular surface organization after solution deposition such as thermal [22-23] and solvent vapor annealing (SVA).[24-28] As a disadvantage, post-treatment requires a preformation of homogeneous and continuous films which limits their applicability in device fabrication. For instance, thermal annealing is not suitable for all the conjugated molecules, especially not suitable for transistors using plastic substrates. In this aspect, SVA is more appealing when thermal annealing risks thermal degradation of the organic layers on the dielectric surfaces, since this process takes place under ambient conditions. However, SVA could not rearrange molecules over macroscopic distances, thus requiring a preformation of homogeneous and continuous films. As a result, SVA is usually employed to treat the homogeneous films deposited by spin coating or drop casting.

The strongest impact on the mesoscopic self-assembly and microstructure is achieved directly during solvent evaporation. In this chapter, a solution processing method, termed as *solvent vapor diffusion* (SVD), is demonstrated, which permits a modification of the self-assembly of organic semiconductors on the surface directly during solvent evaporation. The optimizations of different processing parameters are described in great details.

3.2 Introduction to solvent vapor diffusion

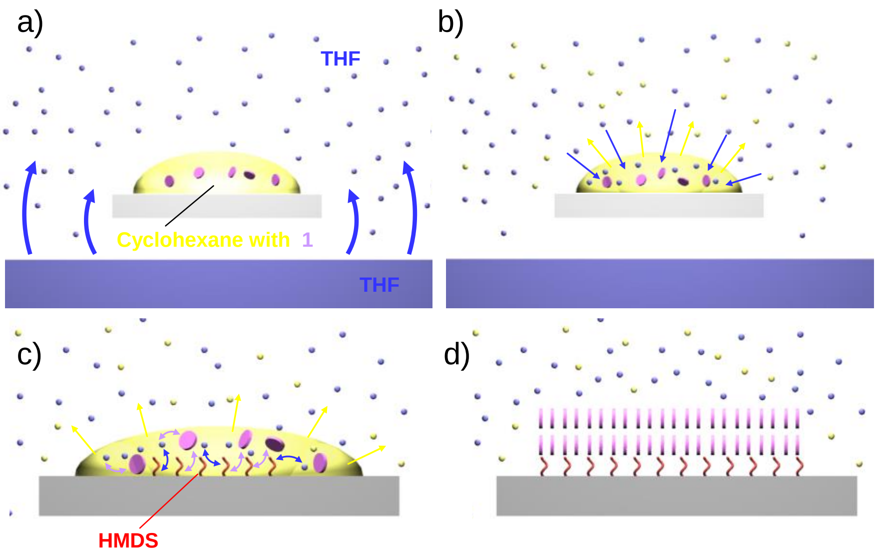

Figure 3.1. Schematic protocol of the SVD process: a) evaporation of THF molecules to saturate the environment, b) THF molecules penetrate into the cyclohexane drop and cyclohexane evaporates, c) THF – HMDS, THF – **3.1** and HMDS – **3.1** interactions within the cyclohexane drop, d) solifification and organization of **3.1** on the HMDS surface.

During the process of SVD a drop cast solution is exposed to a saturated solvent vapor atmosphere in an airtight container (Figure 3.1a). The advantage of this process is the fine adjustment of the evaporation rate of the solution by the right choice of the saturated solvent vapor. This minimizes dewetting effects and ensures the formation of macroscopically homogenous thin layers. At the same time, the evaporation rate can be adapted in terms of the molecular interactions in order to obtain a well-ordered microstructure. Furthermore, a high structural order is achieved due to the active solvent vapor which induces sufficient mobility of the molecules. As a great advantage of the SVD procedure technique a large variety of different processing parameters can be adjusted including also polar/apolar co-solvent conditions under which the solvent polarity forces solvophobic association between the alkyl side chains.[29]

3.3 Drop casting of HBC-PDI on SiO_2 surface

Semiconductor molecules with electron donor (D) and electron acceptor (A) units have recently revealed great potential for applications in both organic solar cells and OFETs.[30-41] A well recognized approach for successful organic photovoltaics is based on bulk heterojunctions, e.g. interpenetrating blends of D and A. [31, 32] Furthermore, blends of D and A were observed to show ambipolar behavior in OFETs, which is highly desirable in organic electronics. [33] In recent years, due to their excellent self-assembly and electronic properties, synthetic nanographenes such as hexa-*peri*-hexabenzocoronene (HBC) and perylene diimide (PDI) are highly promising for applications in organic electronics. [34,35] It has been proven successful that blends of to blend HBC acting as D and perylenetetracarboxy diimide (PDI) serving as A resulted in high efficiencies in organic photovoltaic devices. [32] The high performance was attributed to the phase-segregated structure providing a large interfacial area between D and A. [32] In this aspect, D-A dyads with a covalent link is particular well-suited for fulfilling the phase separation, even at the nanometer scale. Recently D-A dyad composed of HBC and perylene monoimide (PMI) showed a potential in ambipolar transistor with balanced p- and n-type mobilities. [36] In this chapter, we demonstrate the SVD assisted self-assembly and microstructure formation from solution on the example of a D-A dyad (Figure 3.2a, **3.1**) composed of covalently bonded hexa-*peri*-hexabenzocoronene (HBC) as donor and perylene diimide (PDI) as acceptor, synthesized by Dr. Lukas Dössel. This study would provide a fundamental understanding of how processing parameters can be optimized in order to balance dewetting effect and intermolecular interactions, so that one can exploit this approach for other organic semiconductors.

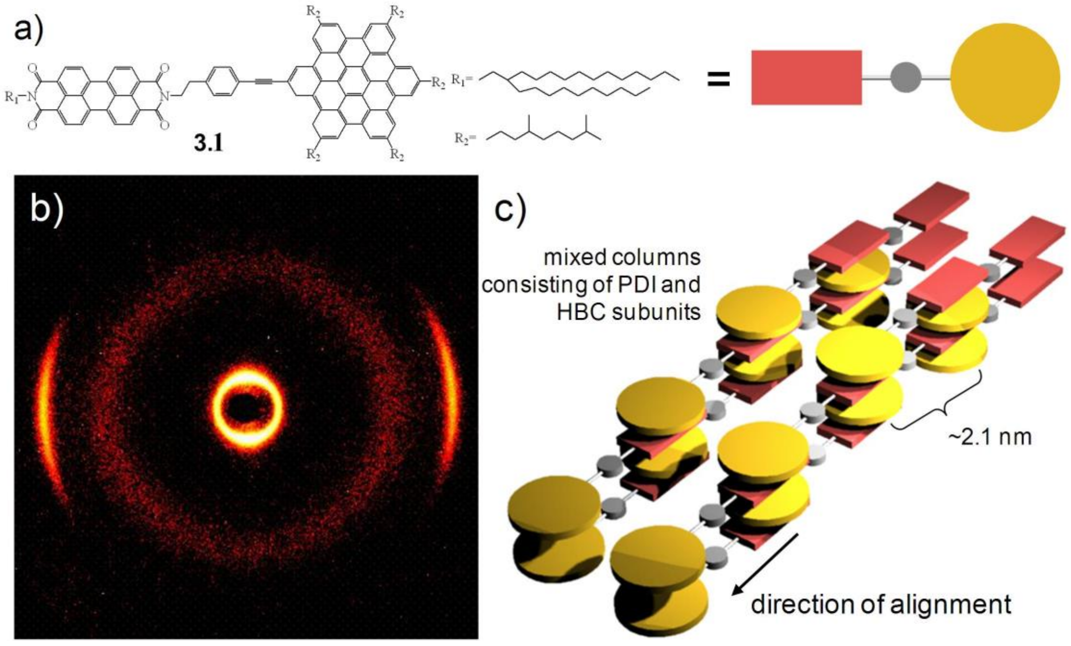

Figure 3.2. a) Molecular structure of **3.1**; b) 2D-WAXS of **3.1** recorded at 30 °C (arrow indicates alignment direction); c) schematic illustration of the supramolecular organization of **3.1** (alky side chains are neglected).

Characterization of thermal behavior and supramolecular structures in bulk provides an estimation of self-assembly tendency. By differential scanning calorimetry scans (DSC) and two-dimensional wide-angle X-ray scattering (2DWAXS) performed by Dr. Alexey Mavrinskiy, **3.1** is liquid crystalline over a broad temperature range from – 100 °C up to 250 °C. The 2D X-ray pattern of extruded filaments of **3.1** is characteristic for a discotic columnar organization (Figure 2.2b). In these one-dimensional stacks a typical π-stacking distance of 0.34 nm is determined. Furthermore, an intercolumnar spacing of only 2.10 nm is derived along the extrusion direction (as indicated by the equatorial position in the pattern) and suggests mixed columns consisting of both HBC and PDI subunits. It is interesting to note that the columnar structures are aligned perpendicular to the extrusion direction due to the high aspect ratio of **3.1**. This behavior has been reported only for liquid crystalline polymers with disc-shaped triphenylene units introduced in the backbone or with attached functional groups capable for additional non-covalent interactions.[42-43]

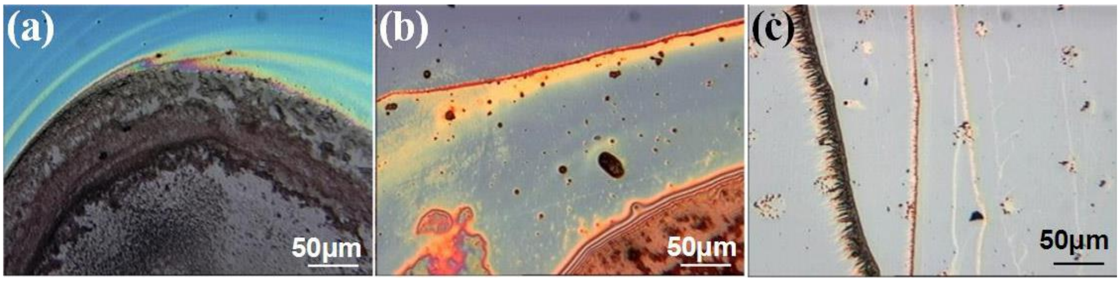

Figure 3.3. POM images of drop cast **3.1** on silicon wafer from different solvent. a) THF, b) chloroform, c) chlorobenzene.

Typically, one-dimensional stacks of liquid crystalline disc-shaped molecules orient along the shearing direction.[44-46] The introduction of a phenylethinylene spacer between the HBC and PDI decreases the steric hindrance in comparison to a single C-C bond between the disc subunits.[36] On the other hand, the bulky dove-tailed side chains, which ensure solubility and thus processibility, are known to dramatically reduce the molecular interactions in the solid state and in solution.[47-49] In consequence, compound **3.1** is liquid crystalline even at low temperatures down to -100 °C and does not form well-ordered microstructured thin films after deposition from solution. Instead, inhomogeneous and disordered patches on the macroscopic scale appear when processed by drop-casting at 0.6 mg/ml from conventional solvents such as THF, chloroform, cyclohexane, toluene and chlorobenzene on SiO_2 surface (Figure 3.3, Figure 3.4a and 3.4b). Reducing the solvent evaporation rate by simply adding a cover over the droplet does not distinctly change the film microstructure. Moreover, applying SVA on the dry thin layer could not improve the film microstructure, since SVA requires a preformation of homogeneous and continuous films. As an additional processing method, precipitation in solvent mixtures also results only in disordered aggregations.

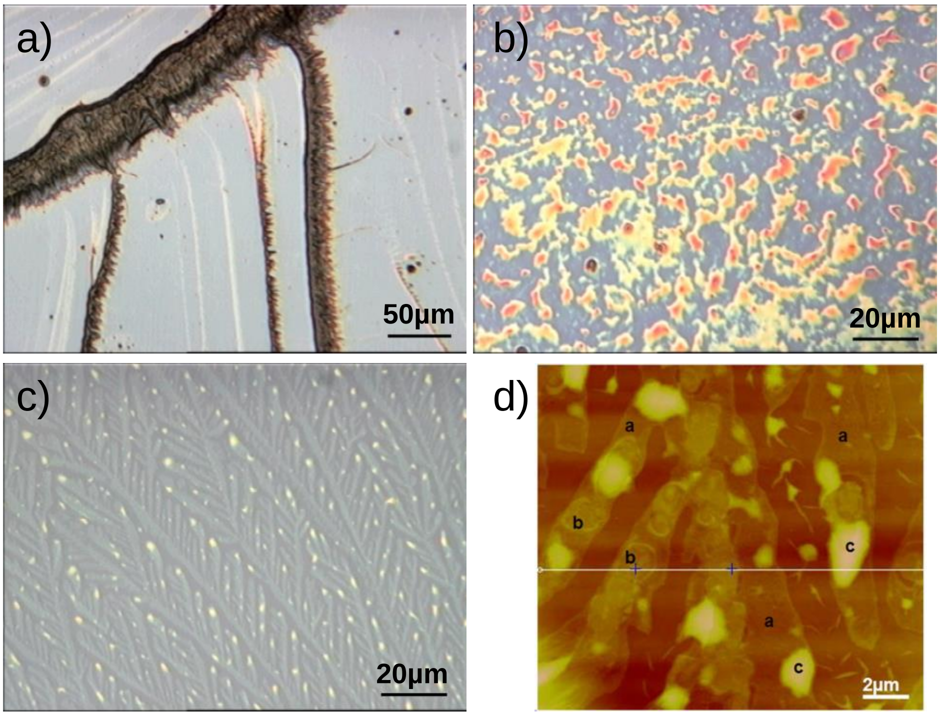

Figure 3.4. Optical microscopy (OM) images of drop cast **1** on silicon wafer from a) toluene and b) cyclohexane, c) OM and d) AFM images of drop cast **3.1** on HMDS-treated silicon wafer form cyclohexane.

3.4 Drop casting of HBC-PDI on modified surface

Interestingly, **3.1** forms large-scale dendritic microstripes only after drop casting from cyclohexane solution on hexamethyldisilazane (HMDS) treated SiO2 surface (Figure 3.4c), which is not observed for other solvents. Moreover, the branches of the microstripes show a well-defined angle of ~40° to each other indicating a tendency towards spontaneous patterning (Figure 3.4c). Each branch consists of hierarchic terraces of different thicknesses which are in correlation with the number of columnar layers. Based on atomic force microscopy (AFM) (Figure 3.4d) and X-ray diffraction (XRD) (Figure 3.5) one can identify three characteristic areas which are labeled as *a* (thickness of 4-6 nm, 2 columnar layers), *b* (9-11 nm, ~4 columnar layers) and *c* (40-50 nm, ~20 columnar layers).

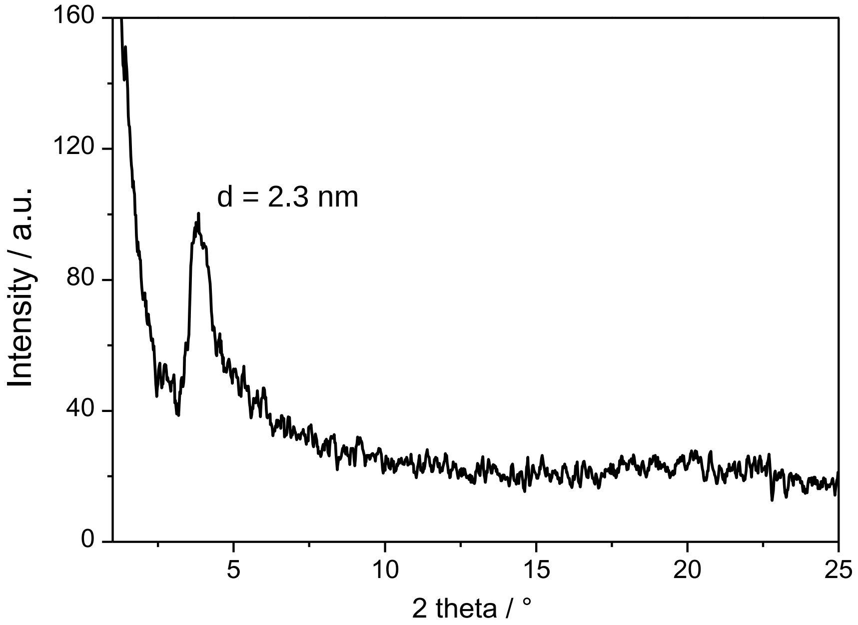

Figure 3.5. XRD of layer in Figure 3.3c.

An identical pattern in the shape of a dentritic microstructure has been previously reported for various polymer films.[50-52] The origin of this morphology is assigned mainly to a dewetting effect for which the initial state is governed by a spinodal process, driven by dispersion forces.[53] For instance, heterogeneous nucleation can be initiated by dust particles that further grow into dendritic morphologies upon thermal annealing.[50] During thermal dewetting, instabilities lead to either spinodal-like dewetting, in which capillary waves are spontaneously amplified, or hole nucleation, in which dry spots are nucleated. Hereby, it is demonstrated in the literature that the evolution of all these dendritic patterns on the surface requires thermal, solvent or hybrid annealing.[50-52] However, in our work these microstructures are directly formed on a HMDS modified SiO_2 surface without any annealing. We assume that the instability regime changes from spinodal dewetting to hole nucleation during the solvent evaporation.[54] While the solvent induced spinodal dewetting affects the microstructure pattern, favorable interactions between the apolar cyclohexane and weakly polar HMDS surface improve the molecular self-assembly within this surface morphology. [26] Previously it was reported that cyclohexane had the ability to induce fiber formation of arylene ethynylene macrocycles (AEM), due to the enhancement of hydrophobic interactions between the long alky chains of AEM. [26] Therefore, cyclohexane is considered as the suitable solvent for further investigations.

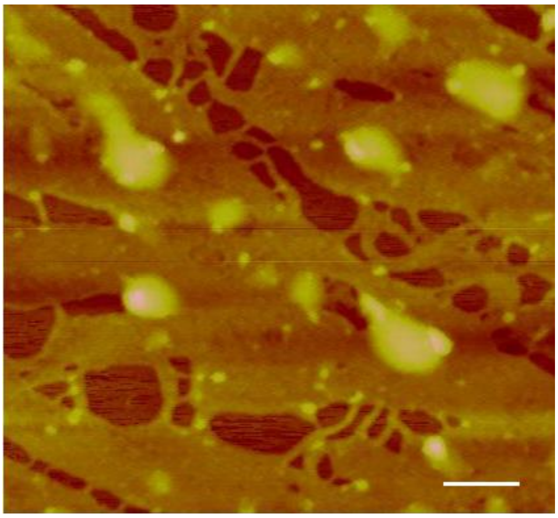

Figure 3.6. AFM image of **3.1** deposited on HMDS from cyclohexane by THF solvent vapor annealing for 2 hours. The scale bar is 2 µm.

3.5 Self-assembly of HBC-PDI by solvent vapor diffusion

Similar to the plain SiO_2 surface, the microstructure on HMDS remains also unchanged when the solvent evaporation rate is reduced by using a cover over the solution. In an additional test, THF solvent vapor annealing was applied on the dry thin layer without improving the microstructure (Figure 3.6). When using SVD on SiO_2 surface, the film does not show significant differences in comparison to the films obtained by simple drop casting. In order to improve the self-assembly and reduce spinodal dewetting effects on the surface of **3.1** during solution processing, SVD and modification of the surface energy have been combined. Through a careful choice of solvent, concentration, vapor atmosphere in combination with surface modification, over macroscopic areas well-ordered microstructures are formed for **3.1** from cyclohexane solution at 0.6 mg/ml on HMDS treated silicon wafer surface in THF vapor atmosphere (Figure 3.7a).

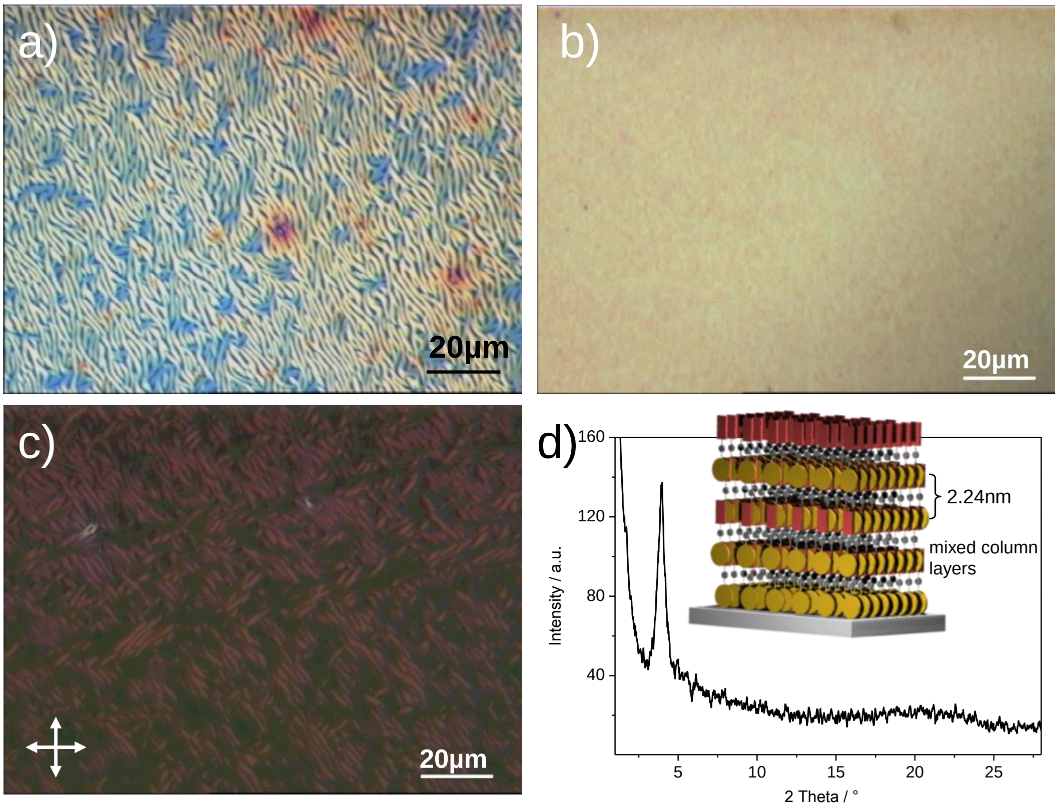

Figure 3.7. OM images of the SVD thin layer of **3.1** from cyclohexane solution on a) HMDS and b) OTS, c) POM with cross-polarizers and d) XRD of layer in a) (Inset illustrates schematically the molecular organization on the surface).

This can be understood on the basis of reduced substrate polarity after hexamethyldisilazane (HMDS) (Figure 3.7a) or octyltrichlorosilane (OTS) (Figure 3.7b) treatment. The nonpolar cyclohexane used for drop casting interacts most favorably with the weakly polar HMDS and OTS modified surface (Figure 3c). In addition to the solvent-substrate interactions, molecule-substrate forces are also enhanced by the surface modification (Figure 3.1c). More precisely, the side chains of **3.1** interplay more strongly with the alkyl groups of the hydrophobic surface.[36] For **3.1**, in comparison to other solvents THF vapor leads to most pronounced interactions between molecule-molecule and molecule-solvent (Figure 3.8).

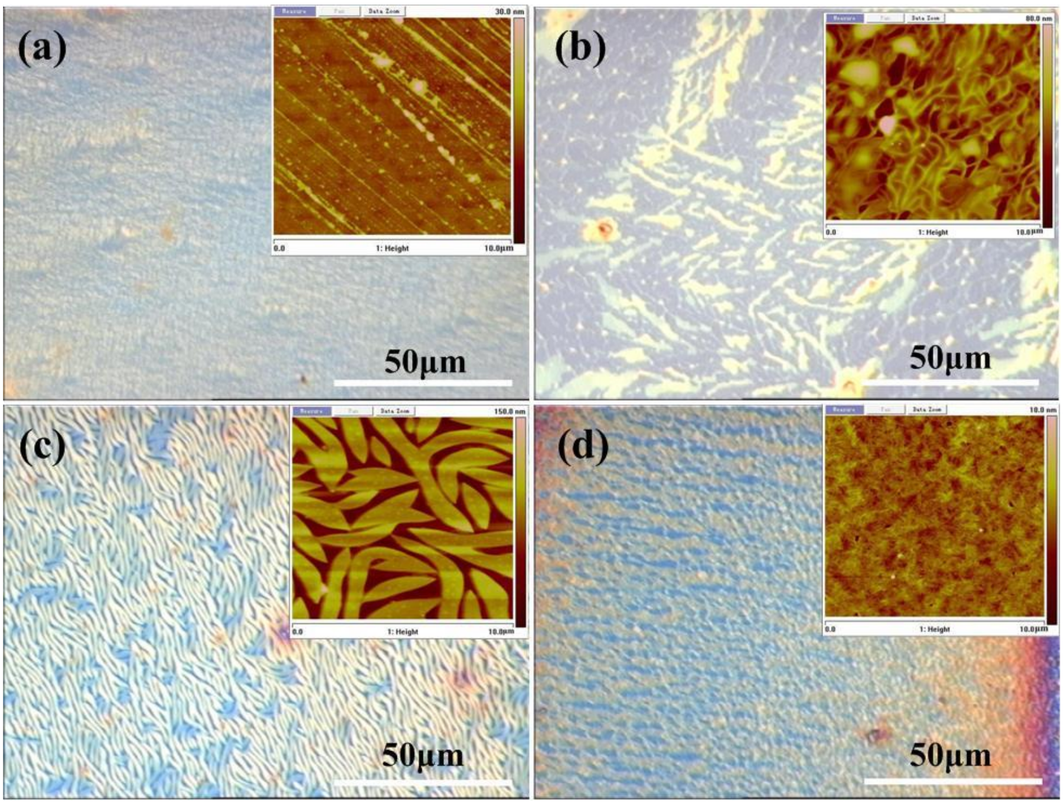

Figure 3.8. POM pictures of surfaces induced by vapor diffusion using different solvents: a) hexane, b) methanol, c) THF, and d) toluene. Insets are AFM pictures related to each POM picture.

This is attributed to the polarity and the boiling point of THF which ensures a sufficiently high vapor pressure. At the first stage of SVD, THF vapor penetrates the cyclohexane solution and interacts with both **3.1** and cyclohexane (Figure 3.1b). Thereby, a high pressure promotes interactions between the drop cast solution and the solvent vapor. In comparison to other low boiling point solvents such as nonpolar hexane, THF is polar and can be exploited for a polar/apolar co-solvent environment with e.g. nonpolar cyclohexane as the solvent during SVD. Finally, after cyclohexane has completely evaporated, the molecules arrange within the thin layer in an edge-on fashion (Figure 3.1d).

But it should be also emphasized that the same penetration effect takes place also for the other solvent vapors, including even the non-miscible methanol. [55] In the case of methanol vapor the increase in solvent polarity forces solvophobic association between the alkyl side chains in a similar manner like 1D self-assembly of surfactants and other amphiphilic molecules. [29] Therefore, minor fibrillar structures and larger aggregates are observed (AFM image in Figure 3.8b) which are, however, less well defined than for THF as the optimal vapor for **3.1**. Finally THF was chosen as the best solvent vapor for the whole study.

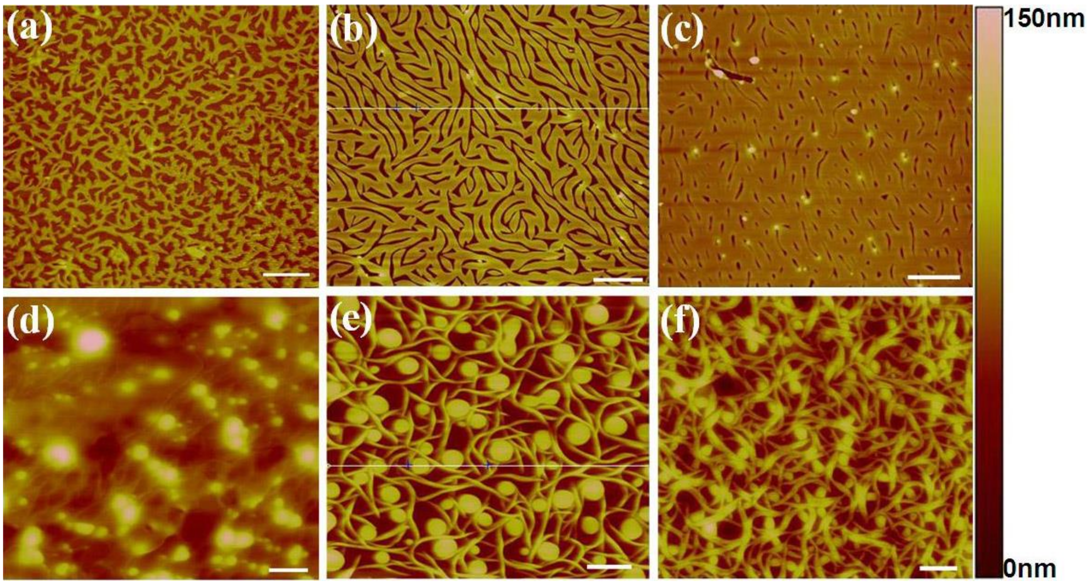

Figure 3.9. AFM images of **3.1** deposited on HMDS from cyclohexane at a) 0.3 mg/ml, b) 0.6 mg/ml, c) 0.9 mg/ml and on OTS at d) 0.3 mg/ml, e) 0.6 mg/ml, f) 0.9 mg/ml during THF SVD. The scale bar in a), b), c) is 10 µm and in d), e), f) is 1 µm, respectively.

The optical microscopy and atomic force microscopy (AFM) images display large-scale (several cm²) uniform microstructures in a so-called *tribal* shape with gently curved branches formed from **3.1** in cyclohexane solution at 0.6 mg/ml on HMDS treated silicon wafer surface in THF vapor atmosphere (Figure 3.7a and 3.9b). From the line profile of the AFM scan a uniform thickness of 60 nm and a mean width of 2 µm of the branches are determined (Figure 3.10a). Interestingly, the microstructure consists of a continuous phase with almost infinite branches which are well interconnected with each other by a complex bifurcation system. The thickness remains in the same range after deposition from a lower or higher concentration, but only the width of the branches and thus the surface coverage change. At 0.3 mg/ml a homogenous network of short fibers of a thickness of ca. 45 nm is apparent (Figure 3.9a), while at 0.9 mg/ml the surface is almost completely covered by the thin layer (Figure 3.9c). This concentration dependence indicates that microstructure formation would occur as long as the concentration of **3.1** in a thin film is subjected to spinodal dewetting at a certain thickness, from which the molecules start to self-assemble.[56-57]

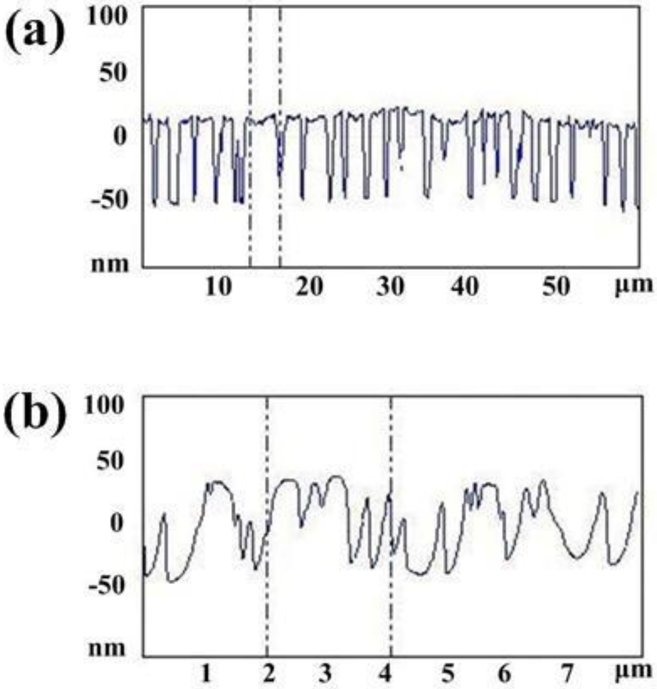

Figure 3.10. a) and b) Height profiles corresponding to the scanning lines in Figure 3.9b) and 3.9e), respectively.

It is further verified by the appearance of a peak in the X-ray diffractogram for this layer which is assigned to the intercolumnar spacing of 2.24 nm (Figure 3.8d). We assume from the XRD structural analysis that the discs are arranged edge-on toward the substrate, while the columnar stacks are oriented along the belts. Due to the pronounced beam sensitivity of the molecules during study by transmission electron microscopy (TEM), a further structure evaluation is not possible.

Since the surface modification plays an essential function in the molecular self-assembly and the establishment of the microstructure (termed as morphology in mirco- and nanoscale), [58-61] it is expected that modification of the surface energy leads also in the case of **3.1** to different morphologies. This is verified by an additional experiment in which the surface energy is even lowered. Hereby, during the past two decades, intensive research has shown that surface energy of OTS treatment is smaller than 30.0 mJ/m^2, whereas for HMDS treatment it is bigger than 40.0 mJ/m^2, [62-64] which were calculated from the tree contact angles using three liquids with different polarities and surface tensions by a Lewis acid/base model. [62, 64] Indeed, altering the surface from HMDS to OTS results in a significant change in the microstructure for **3.1**. For the OTS treated surface, a homogeneously distributed mixed fiber-sphere structure is obtained over large areas (see the homogenous macroscopic area in Figure 3.7b and for the mesoscopic scale Figure 3.9d, e, f) which also reveals a concentration dependence. At a lower concentration of 0.3 mg/ml almost only spherical units are formed with a broad size range from 50 to 900 nm. A thickness of only 6-8 nm is determined for the few fibers which are mostly located below the spherical objects (Figure 3.9d). Doubling the concentration gives rise to more well-defined fibers with an increased thickness of 80 nm and width of 200 nm being now identical for the spheres which have a mean size of 450 nm (Figure 3.10b). Both types of objects are distributed homogeneously over the surface and their dimensions are more uniform in comparison to the low concentration (Figure 3.9e). Interestingly, at a much higher concentration of 0.9 mg/ml the size of the spheres decreases to 200 nm, while the fiber density and width (350 nm) significantly increase (Figure 3.9f). The morphology difference between HMDS and OTS treated surface can be only attributed to the longer alky chains of OTS in comparison to HMDS leading to stronger hydrophobic interactions between OTS and the alky chains of **3.1** and finally to a more pronounced self-assembly of the molecules into well-defined anisotropic 1D fibers. In contrast to these objects, the isotropic sphere-like structures indicate less molecular interactions and are assumed to be generated mainly by dewetting. At higher concentrations, simply more building blocks directly interact with the OTS surface and further increase dominant role of the fiber in the thin layer, while the dewetting effect and the sphere density are reduced.

3.6 Conclusion

In conclusion, SVD is a powerful tool which allows a delicate control over the microstructure of organic semiconductors on the surface as presented in this chapter for HBC-PDI dayd **3.1**. Particularly, the large variety of processing parameters, such as surface energy and solvent polarity in the solution and vapor open the opportunity to fine balance dewetting effects and various forces, including solvent-molecule, solvent-substrate, and molecule-substrate interactions in order to achieve the desired microstructure and molecular organization on the surface. This processing approach to control the (macro)molecular self-assembly can be further exploited for a broad range of organic semiconductors and even proton/ion conducting materials, but also other systems for which the surface morphology plays an important role in the functionality of the thin layer. This can include for instance self-assembly structures to tailor the surface energy or photophysical properties of films. This work provides a fundamental understanding of the influences of a variety of parameters on the microstructure evolution of semiconductor molecules. It opens new avenues towards the self-assembly of semiconductor molecules into well defined microstructures, especially for those showing a low self-assembly tendency when processed by conventional solution processing. Based on the findings, this chapter represents a model strategy allowing highest control over the microstructure evolution during the solvent evaporation for solution processing of semiconductor molecules. To exploit this concept for other systems, in the following chapters, SVD is further applied for the self-assembly of dithieno[2, 3-*d*;2’, 3’-*d*’]benzo[1,2-*b*;4,5-*b*’]dithiophene (compound 4.1 in chapter 4) and Cyclopentadithiophene-benzothiadiazole copolymer (compound 5.1 in chapter 5) into highly ordered 1D structures.

REFERENCES

[1] H. Sirringhaus, *Adv. Mater*. **2005**, *17*, 2411.

[2] B. A. Jones, A. Facchetti, M. R. Wasielewski, T. J. Marks, *Adv. Funct. Mater.* **2008**, *18,* 1329.

[3] Y. Ito, A. A. Virkar, S. Mannsfeld, J. H. Oh, M. Toney, J. Locklin, Z. N. Bao, *J. Am. Chem. Soc.* **2009**, *131*, 9396.

[4]J. K. Lee, W. L. Ma, C. J. Brabec, J. Yuen, J. S. Moon, J. Y. Kim, K. Lee, G. C. Bazan, A. J. Heeger, *J. Am. Chem. Soc.* **2008**, *130*, 3619.

[5] H. Xin, F. S. Kim, S. A. Jenekhe, *J. Am. Chem. Soc.* **2008**, *130*, 5424.

[6] T. Someya, H. E. Katz, A. Gelperin, A. J. Lovinger, A. Dodabalapur, *Appl. Phys. Lett.* **2008**, *92*, 143322.

[7] R. Bourguiga, G. Horowitz, F. Garnier, R. Hajlaoui, S. Jemai, H. Bouchriha, *Eur. Phys. J. AP*, 2002, **19**, 117.

[8] L. Zang, Y. Che, J. S. Moore, *Acc. Chem. Res.*, **2008**, *41*, 1596.

[9] S. Xiao, J. Tang, T. Beetz, X. Guo, N. Tremblay, T. Siegrist, Y. Zhu, M. Steigerwald, C. Nuckolls, *J. Am. Chem. Soc.* **2006**, *128*, 10700.

[10] W. Pisula, A. Menon, M. Stepputat, I. Lieberwirth, U. Kolb, A. Tracz, H. Sirringhaus, T. Pakula, K. Müllen, *Adv. Mater.*, **2005**, *17*, 684.

[11] S. Sergeyev, W. Pisula, Y. H. Geerts, *Chem. Soc. Rev.*, **2007**, *36*, 1902.

[12] V. Palermo, P. Samorì, *Angew. Chem. Int. Ed.* **2007**, *46*, 4428.

[13] V. Biju, M. Micic, D. Hu, H. P. Lu, *J. Am. Chem. Soc.* **2004**, *126,* 9374.

[14] H. L. Yip, H. Ma, A. K. Y. Jen, J. C. Dong, B. A. Parviz, *J. Am. Chem. Soc.* **2006**, *128*, 5672.

[15] N. L. Liu, Y. Zhou, L. Wang, J. B. Peng, J. Wang, J. Pei, Y. Cao, *Langmuir* **2009**, *25*, 665.

[16] R. Dabirian, X. L. Feng, L. Ortolani, A. Liscio, V. Morandi, K. Müllen, P. Samorì, V. Palermo, Phys. Chem. Chem. Phys. **2010**, *12*, 4473.

[17] G. Wang, J. Swensen, D. Moses, A. J. Heeger, *J. Appl. Phys.*, **2003**, *93*, 6137.

[18] L. Li, P. Gao, K. C. Schuermann, S. Ostendorp, W. Wang, C. Du, Y. Lei, H. Fuchs, L. DeCola, K. Müllen, L. Chi, *J. Am. Chem. Soc.* **2010**, *132*, 8807.

[19] P. C. Ohara, J. R. Heath, W. M. Gelbart, *Angew. Chem. Int. Ed. Engl.* **1997**, *36*, 1077.

[20] P. Muller-Buschbaum, R. Gebhardt, E. Maurer, E. Bauer, R. Gehrke, W. Doster, *Biomacromolecules* **2006**, *7*, 1773.

[21] S. Herminghaus, K. Jacobs, K. Mecke, J. Bischof, A. Fery, M. Ibn-Elhaj, S. Schlagowski, *Science*, **1998**, *282*, 916.

[22] P. Viville, R. Lazzaroni, J. L. Brédas, P. Moretti, P. Samorì, F. Biscarini, *Adv. Mater.* **1998**, *10*, 57.

[23] P. Samorì, H. Engelkamp, P. A. J. de Witte, A. E. Rowan, R. J. M. Nolte, J. P. Rabe, *Adv. Mater.* **2005**, *17*, 1265.

[24] B. A. Gregg, *J. Phys. Chem.* **1996**, *100*, 852.

[25]J. C. Conboy, E. J. C. Olson, D. M. Adams, J. Kerimo, A. Zaban, B. A. Gregg, P. F. Barbara, *J. Phys. Chem. B* **1998**, *102*, 4516.

[26] G. De Luca, A. Liscio, P. Maccagnani, F. Nolde, V. Palermo, K. Müllen, P. Samorì, *Adv. Funct. Mater.* **2007**, *17*, 3791.

[27] G. De Luca, A. Liscio, F. Nolde, L. M. Scolaro, V. Palermo, K. Müllen, P. Samorì, *Soft Matter* **2008**, *4*, 2064.

[28] K. C. Dickey, J. E. Anthony, Y. L. Loo, *Adv. Mater.* **2006**, *18*, 1721.

[29] Y. Che, A. Datar, K. Balakrishnan, L. Zang, *J. Am. Chem. Soc.* **2007**, *129*, 7234.

[30] Y. Yamamoto, T. Fukushima, Y. Suna, N. Ishii, A. Saeki, S. Seki, S. Tagawa, M. Taniguchi, T. Kawai, T. Aida, *Science* **2006**, *314*, 1761.

[31] G. Yu, J. Gao, J. C. Hummelen, F. Wudl, A. J. Heeger, *Science*, **1995**, *270*, 1789.

[32] L. Schmidt-Mende, A. Fechtenkötter, K. Müllen, E. Moons, R. H. Friend, J. D. MacKenzie, *Science*, **2001**, *293*, 1119.

[33] E. J. Meijer, D. M. De Leeuw, S. Setayesh, E. Van Veenendaal, B. H. Huisman, P. W. M. Blom, J. C. Hummelen, U. Scherf, T. M. Klapwijk, *Nat. Mater.* **2003**, *2*, 678.

[34] J. S. Wu, W. Pisula, K. Müllen, *Chem. Soc. Rev.* **2007**, *36*, 1902.

[35] F. Würthner, *Chem. Commun.* **2004**, 1564.

[36] J. M. Mativetsky, M. Kastler, R. C. Savage, D. Gentilini, M. Palma, W. Pisula, K. Müllen, P.Samorì, *Adv. Funct. Mater.* **2009**, *19*, 2486.

[37]Y. K. Fang, C. L. Liu, C. X. Li, C. J. Lin, R. Mezzenga, W. C. Chen, *Adv. Mater*. **2010**, *20*, 3012.

[38] Y. Zhu, R. D. Champion, S. A. Jenekhe, *Macromolecules* **2006,** *39*, 8712.

[39] P. Wu, F. S. Kim, R. D. Champion, S. A. Jenekhe, *Macromolecules* **2008**, *41*, 7021.

[40] H. Imahori, T. Umeyama, *J. Phys. Chem. C* **2009,** *113*, 9029.

[41] J. Arias-Pardilla, W. Walker, F. Wudl, T. F. Otero, *J. Phys. Chem. B* **2010,** *114*, 12777.

[42] X. L. Feng, W. Pisula, L. J. Zhi, M. Takase, K. Müllen, *Angew. Chem. Int. Ed.* **2008**, *47*, 1703.

[43] T. C. Hsu, B. Hüser, T. Pakula, H. W. Spiess, M. Stamm, *Makromol. Chem.* **1990**, *191*, 1597.

[44] S. Laschat, A. Baro, N. Steinke, F. Giesselmann, C. Hägele, G. Scalia, R. Judele, E. Kapatsina, S. Sauer, A. Schreivogel, M. Tosoni, *Angew. Chem. Int. Ed.* **2007,** *46*, 4832.

[45] X. L. Feng, W. Piaula, K. Müllen, *Pure Appl. Chem.*, **2009**, *81*, 2203.

[46] W. Piaula, X. L. Feng, K. Müllen, *Adv. Mater.* **2010**, *22*, 3634.

[47] M. Kastler, W. Pisula, D. Wasserfallen, T. Pakula, K. Müllen, *J. Am. Chem. Soc.* **2005,** *127*, 4286.

[48] W. Pisula, M. Kastler, D. Wasserfallen, M. Mondeshki, J. Piris, I. Schnell, K. Müllen, *Chem. Mater.* **2006**, *18*, 3634.

[49] B. Tylleman, G. Gbabode, C. Amato, C. Buess-Herman, V. Lemaur, J. Cornil, R. G. Aspe, Y. H. Geerts, S. Sergeyev, *Chem. Mater.*, **2009**, *21*, 2789.

[50] N. Koneripalli, F. S. Bates, G. H. Fredrickson, *Phys. Rev. Lett.*, **1998**, *81,* 1861.

[51] J. Peng, Y. Han, W. Knoll, D. H. Kim, *Macromol. Rapid Commun.*, **2007**, *28,* 1422.

[52] M. Ramanathan, S. B. Darling, *Soft Matter*, **2009**, *5*, 4665.

[53]A. Sharma, R. Khanna, *Phys. Rev. Lett.*, **1998**, *81*, 3463.

[54] J. L. Masson, P. F. Green, *Phys. Rev. Lett.*, **2002**, *88,* 205504.

[55]N. E. Chayen, *J. Appl.Cryst.*, **1997**, *30*, 198.

[56] X. L. Feng, W. Pisula, T. Kudernac, D. Q. Wu, L. J. Zhi, S. D. Feyter, K. Müllen, *J. Am. Chem. Soc.* **2009**, *131*, 4439.

[57] A. M. Higgins, R. A. L. Jones, *Nature*, **2000**, *404*, 476.

[58] P. T. Boudreault, S. Wakim, N. Blouin, M. Simard, C. Tessier, Y. Tao, M. Leclerc, *J. Am. Chem. Soc.* **2007**, *129*, 9125.

[59] H. Usta, C. Risko, Z. M. Wang, H. Huang, M. K. Deliomeroglu, A. Zhukhovitskiy, A. Facchetti, T. J. Marks, *J. Am. Chem. Soc.* **2009**, *131*, 5586.

[60] R. Dabirian, V. Palermo, A. Liscio, E. Schwartz, M. B. J. Otten, C. E. Finlayson, E . Treossi, R. H. Friend, G. Calestani, K. Müllen, R. J. M. Nolte, A. E. Rowan, P. Samorì, *J. Am. Chem. Soc.* **2009**, *131*, 7055.

[61] S. Joshi, P. Pingel, S. Grigorian, T. Panzner, U. Pietsch, D. Neher, M. Forster, U. Scherf, *Macromolecules*, **2009**, *42*, 4651.

[62] K. X. Ma, C. H. Ho, F. Zhu, T. S. Chung, *Thin Solid Films*, **2000**, *371*,140.

[63] D. S. Park, S. J. Kang, H. J. Kim, M. H. Jang, M. Noh, K. H. Yoo, C. N. Whang, *J. Vac. Sci. Technol. B*, **2005**, *3*, 23 .

[64] S. C. Lim, S. H. Kim, J. H. Lee, M. K. Kim, D. J. Kim, T. Zyung, *Synthetic Metals*, **2005**, *148*, 75.

Chapter 4.

Microribbon Field-Effect Transistors Based on Dithieno [2,3-d;2,3’-d’]benzo[1,2-b;4,5-b’]dithiophene Processed by Solvent Vapor Diffusion

4.1 Introduction

Inspired by the SVD assisted self-assembly demonstrated in chapter 3, this chapter aims to exploit such a model strategy to control the self-assembly of semiconductor molecules into single crystals for their applications in high performance OFETs. Before choosing semiconductor candidates, the recent progress of the high performance OFETs should be stated as research background. Among one-dimensional (1D) nano- or microstructures, single crystal mircoribbons or microwires are free of grain boundaries and molecular disorder, facilitating directional charge transport and excition diffusion. [1-23] High-performance OFETs based on such nano- and micro-sized single crystal ribbons or wires have been reported for various small conjugated molecules. For instance, single-crystal OFETs based on copper phthalocyanine nanoribbon exhibited hole mobilities of 0.5 cm^{2}V^{-1}s^{-1}, [10] whereas single-crystal microwires self-assembled from bis-phenylethyl-perylene-tetracarboxylic diimide showed an electron mobility of 1.4 cm^{2}V^{-1}s^{-1}. [11] Recently, mobilities even beyond 2.0 cm^{2}V^{-1}s^{-1} were observed for n- as well as p-type OFETs based on single crystal ribbons of various small crystalline building blocks. [12-15] Although recently solution processing methods such as solvent vapor annealing

(SVA) [13, 22] and precipitation in solvent mixtures [1] have been successfully employed to induce 1D structures, so far it is still a challenge to grow organic single crystals directly on the substrate and to incorporate them into high performance OFETs yielding mobilities above 1 $cm^2V^{-1}s^{-1}$, which is desirable for the practical applications.

Here, high performance (dithieno[2, 3-*d*;2', 3'-*d*'] benzo[1,2-*b*;4,5-*b*']dithiophene -DTBDT, **4.1**, Scheme 4.1) is chosen for the following reasons: 1) thin film OFETs based on **4.1** exhibited hole mobilities of up to 0.01 $cm^2V^{-1}s^{-1}$. [34] Notably, this mobility is obtained on an untreated SiO_2 insulator surface and spin-coated films with only small crystalline domains, which hinder the charge transport due to numerous grain boundaries. This value was further increased to an average of 1.0 $cm^2V^{-1}s^{-1}$ via dip-coating by extending the size of the crystalline domains. [34] However, one can expect that this is not the ultimate device performance because the uniaxially oriented thin films still suffer from grain boundaries which inevitably affect the charge carrier transport between the electrodes. Based on these data, it can be anticipated that higher hole mobilities could be achieved by further elevating the structural order of the molecules for instance in single crystal ribbons. 2) Conventional solution processing methods could not yield single crystal ribbons for **4.1**. Moreover, applying solvent vapor annealing on the dry thin layer does not distinctly change the film microstructure. As an additional processing method, the precipitation in solvent mixtures also does not result in surface crystals. 3） Compound **4.1** represents heteroacene molecules showing great potential for creating crystalline films with satisfying performance in solution-processed organic electronic devices. Understanding how to control the processing parameters to self-assembly **4.1** into single crystals will allow the exploitation of such a strategy for a broad range of other molecular systems, e. g. other small heteroacene molecules possessing an extended aromatic core and solubilizing alkyl chains. Therefore, in this work, SVD is applied for the formation of crystal microribbons of **4.1**. Interestingly, more than hundreds of micrometers long crystals are assembled only in several minutes, resulting in high p-type charge-carrier mobilities up to 3.2 $cm^2V^{-1}s^{-1}$. The structural analysis indicates single crystallinity of these objects.

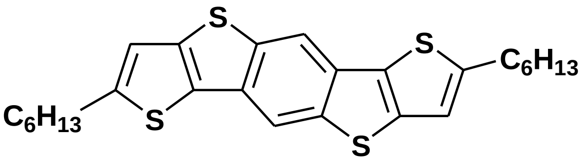

4.1

Scheme 4.1. Molecular structure of **4.1** (dithieno[2, 3-*d*;2', 3'-*d*']benzo[1,2-*b*;4,5-*b*'] dithiophene –DTBDT)

4.2. Self-assembly of crystal microribbons on the surface

In order to find the right solvent for SVD, the self-assembly behavior of **4.1** was systematically studied via screening various solution processing methods. Simple drop casting of **4.1** from solution does not yield crystal objects or well-ordered thin films.(Figure 4.1) Instead, inhomogeneous and disordered patches on the macroscopic scale appear when processed in this way from conventional solvents such as THF (Figure 4.1a), chloroform (Figure 4.1b), toluene and chlorobenzene on HMDS-treated SiO_2 surface. It is observed that drop casting from cyclohexane (Figure 4.2c) leads to **4.1** crystalline domains which shows a great potential for single crystal growth. After optimization of the SVD parameters such as solvent, concentration, vapor atmosphere, crystal microribbons on HMDS-treated SiO_2 silicon wafer were obtained in short time (5 minutes) by using cyclohexane as solvent for **4.1** solution at a concentration of 0.1~1.0 mg/ml and THF as solvent vapor. Thereby, THF vapor penetrates the cyclohexane solution and interacts with both **4.1** and cyclohexane. This reduces the evaporation rate of the drop cast solution and provides polar/apolar co-solvent conditions under which the increase in solvent polarity forces solvophobic association between the alkyl side chains in a similar manner like during 1D self-assembly of surfactants and other amphiphilic molecules. [9] As a great advantage of this method, the length of the microribbons is well-controlled from few tens to several hundred of micrometers by simply tuning the concentration of the compound in cyclohexane. At 0.1 mg/ml an average microribbon length of around ca. 20μm is apparent (Figure 4.1d), while at 1.0 mg/ml, microribbons longer than 200 μm are grown (Figure 4.1f).

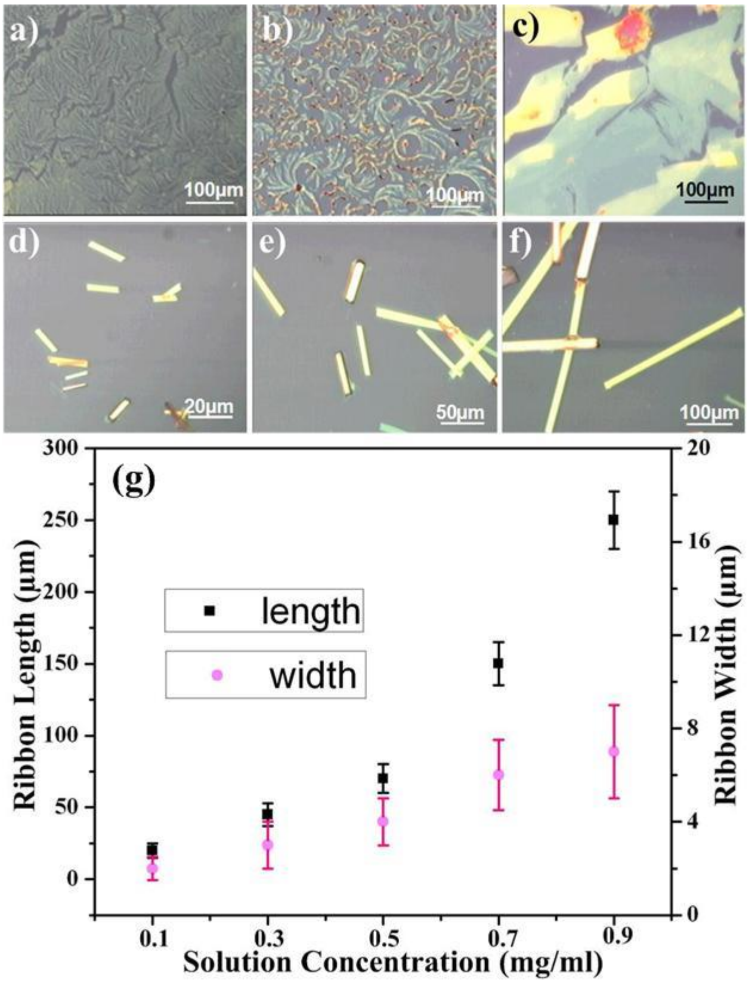

Figure 4.1. Reflection optical microscopy (OM) images of drop cast **4.1** from a) THF, b) chloroform, c) cyclohexane on HMDS-treated silicon wafer; OM images of SVD **4.1** from cyclohexane under THF vapor at a concentration of d) 0.1 mg/ml, e) 0.5 mg/ml and f) 1.0 mg/ml, and g) ribbon dimensions as a function of the solution concentration.

The ribbon thickness also increases for higher concentration, but not to the same extent as the length (Figure 4.2). The thickness expands from an average value of 27 nm for 0.2 mg/ml to 68 nm for 1.0 mg/ml. Additionally, the variation of the thickness enlarges with increasing concentration. It has to be noted that the plot in Figure 2g does not take into account the number of formed ribbons for each concentration, but only displays the relation between dimensions of single ribbons and the concentration.

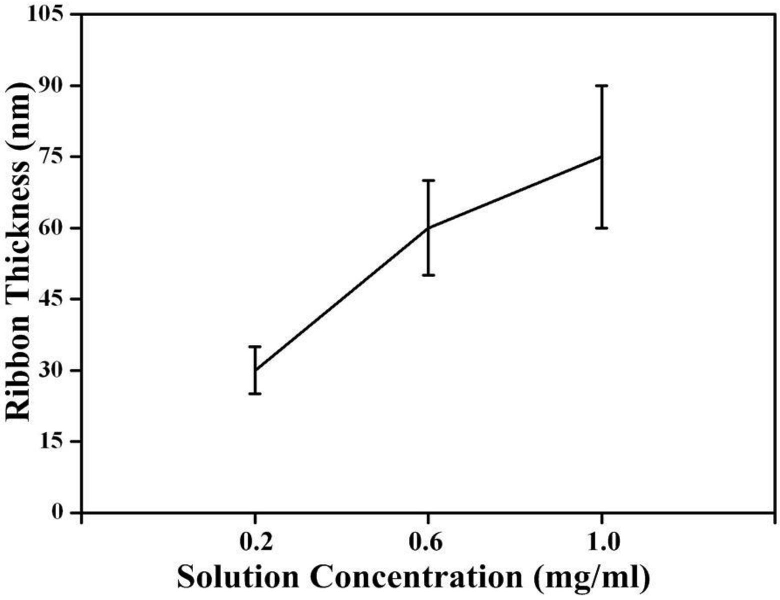

Figure 4.2. Ribbon thickness as a function of concentration.

4.3. Structural analysis of the microribbons

Under the cross-polarized optical microscope, the microribbons exhibit a pronounced homogenous birefringence and strong optical anisotropy indicating high molecular order and uniform orientation within the ribbon. (Figure 4.3a) A typical microribbon scanned by an atomic force microscope (AFM) reveals also a uniform width of ca 2 µm and height of 30 nm with an extremely low top surface roughness, which is an ideal candidate for FET applications (Figure 4.3c, 4.3d).

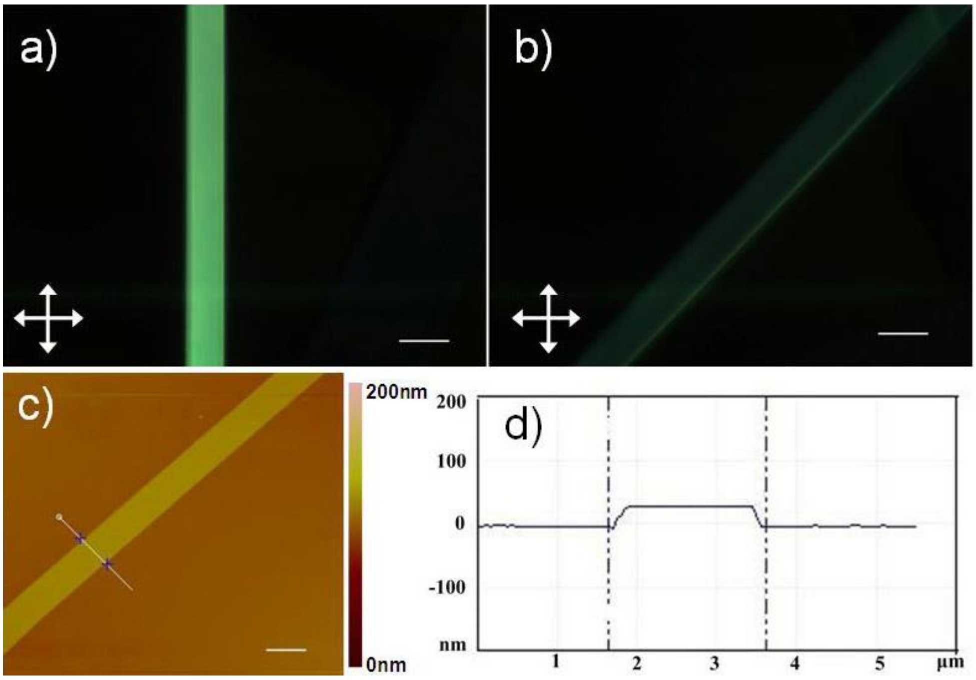

Figure 4.3. Cross polarized optical images of microribbons obtained by SVD from **4.1** at a) 0° and b) 45° rotation towards the polarizers (scale in both POM images corresponds to 10 µm), c) AFM image of a microribbon crystal (scale corresponds to 2 µm) and d) height profile. The width and the height of the crystal are *ca* 2 µm and 30 nm, respectively.

In order to elucidate the molecular packing of the crystal ribbons, a surface X-ray diffraction (XRD) in reflection mode was firstly performed for a macrosopically large area with randomly deposited ribbons (Figure 4.4a). Interestingly, although numerous ribbons scatter the X-ray at the same time, only peaks corresponding to a spacing of 1.85 nm appear. An identical diffractogram has been obtained for the dip-coated thin film of **4.1** indicating the same molecular arrangement on the surface.[34, 35] For the ribbons, the spacing is close to the unit-cell parameter *c* of the single crystal[34] and is oriented perpendicular to the surface. To further evaluate the exact arrangement of the two other crystal planes *a* and *b* within the ribbons, which are oriented parallel to the surface plane, transmission electron microscopy (TEM) was used. The corresponding image of the crystal microribbions is shown in Figure 4.4b confirming once again their regular rectangular shape. A deeper insight into the molecular organization is obtained from selected-area-diffraction (SAED) pattern for one ribbon (Figure 4.4c). No change of the SAED pattern is observed for different parts of the same ribbon, indicating single crystallinity of the 1D object. The analysis of the pattern revealed almost the same *a* = 0.57 nm and *b* = 0.63 nm unit parameters as found in the single crystal reported previously, [34] whereby *a* and *c* are slightly larger in the ribbon. This minor increase can be related to the different processing SVD method yielding the ribbons. The crystal arrangement, in which the *a* plane is oriented along the ribbon axis, is illustrated in Figure 4.5a and is favorable for transistor applications since it coincidences with the stacking direction and the charge carrier transport. [13,35]

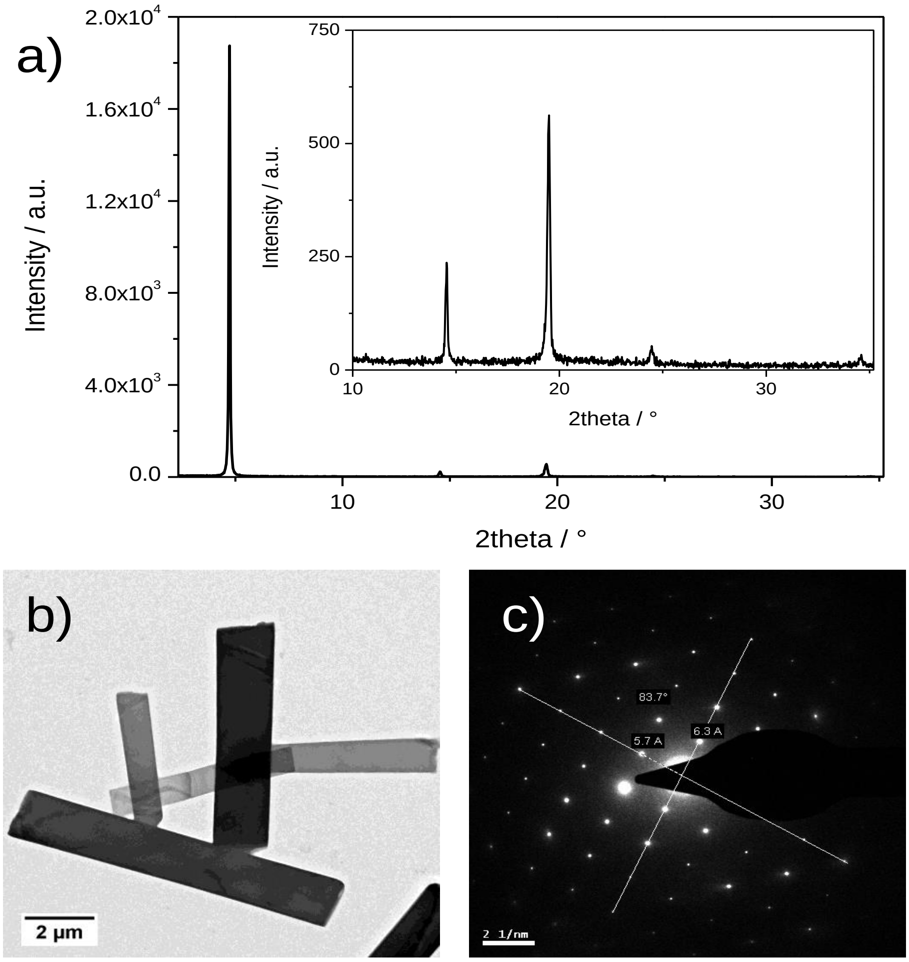

Figure 4.4. Structural investigation of the microribbons of **4.1** by a) XRD, b) TEM image and c) SAED pattern of one single ribbon.

4.4. Transistors based on single crystal microribbons

Crystal microribbons of **4.1** were processed at a concentration of 0.3 mg/ml for the FET applications yielding a length of 45±8 μm, width of 4±2 μm, and thickness of 40±5 nm. The resulting microribbons were contacted using a shadow mask under an optical microscopy and OFETs were fabricated on HMDS treated SiO_2 by evaporating source and drain gold electrodes, in this way establishing a bottom-gate, top-contact geometry (Figure 4.5b). All transistors exhibited typical *p*-channel field-effect characteristics. An average mobility of 1.8±0.3 $cm^2V^{-1}s^{-1}$, and an average on/off ratio of (6±2) $\times 10^6$ are determined for 20 individual devices, with the highest mobility of 3.2 $cm^2V^{-1}s^{-1}$ achieved and an on/off ratio up to 6×10^6. Standard transfer and output curve are shown in Figure 4.5c and 4.5d. Both the average and the highest mobility values represent approximately two-fold improvement in comparison to the dip-coated film which is attributed to the increased molecular order and apparent reduction of domain boundaries within the transistor channel. Moreover, lower threshold voltages of -24±5 V are obtained in comparison to the dip coated film (-39±6 V) because of decreased charge trapping at the organic/insulator interface and within the semiconductor layer itself. [37]

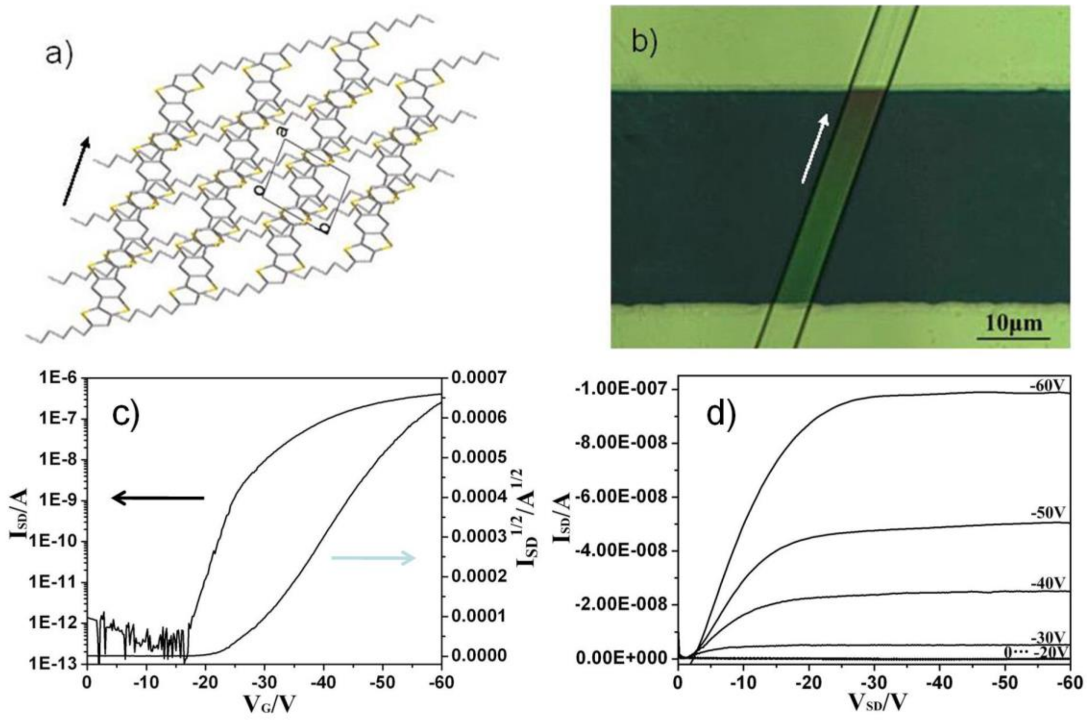

Figure 4.5. a) the crystal structure in top view within the microribbon (black arrow indicates the ribbon axis), b) optical microscopy image of the individual ribbon OFET (white arrow indicates the crystal *a* axis) and, and corresponding c) transfer and d) output curves.

4. 5 Conclusion

In conclusion, solvent vapor diffusion was successfully utilized to fabricate hundreds of micrometers long DTBDT crystal microribbons directly on SiO_2 surface. The dimensions of the ribbons are tunable simply by controlling the concentration of the solution. The structural study indicates that the *a* plane in the single crystal is oriented along the ribbon axis, which is considered to be favorable for the carrier transport along ribbon axis. In the device, individual crystal DTBDT OFETs exhibit mobilities as high as 3.2 $cm^2V^{-1}s^{-1}$ and on/off ratio up to 10^6. It has to be emphasized that few examples of 2D single crystals lead to significantly higher mobilities, but their processing and device implementation is more demanding.[24-32] It is convincing that

SVD could be further exploited to control over the microstructure of crystalline semiconductors into well-defined 1D objects, yielding unprecedented performance. Interestingly, for compound **4.1**, we can clearly compare how different processing methods influence the film morphology and molecular packing on the surface, which then determine the device performance of transistors. As is shown in Figure 4.6, spin coating results in film structure with a high number of small crystalline domains and a high density of grain boundaries which act as structural trapping sites on the surface.

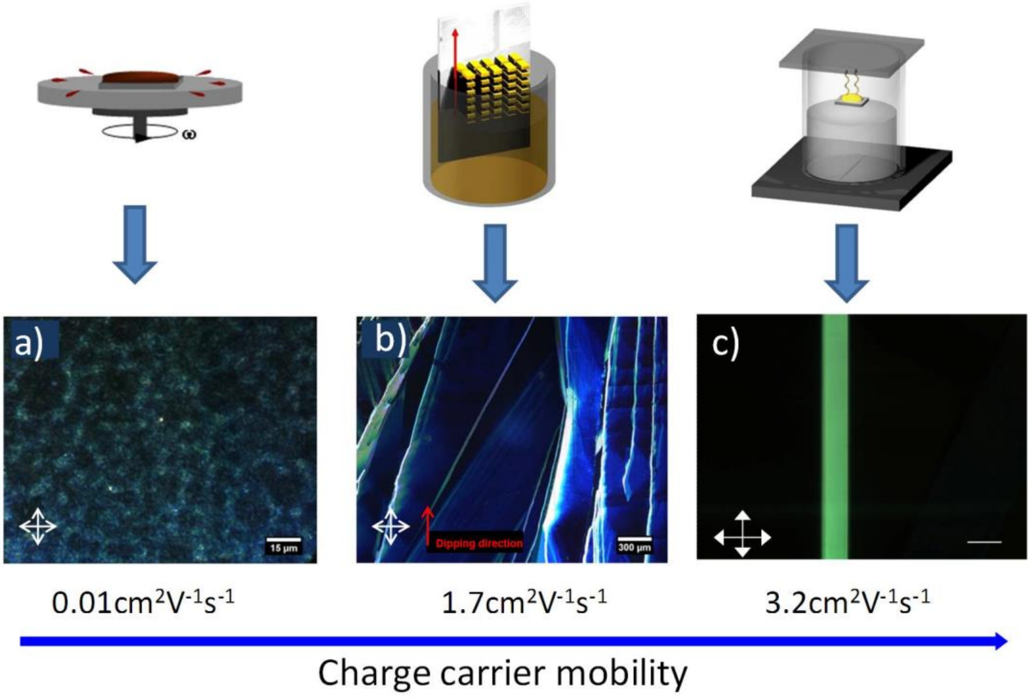

Figure 4.6. Influence of different processing methods on the film morphology and the corresponding charge carrier mobilities. a) Spin coating b) dip coating, and c) solvent vapor diffusion.

In comparison, the morphology and molecular packing are improved via dip coating, that the size of crystalline domains is greatly enlarged, which leads to a significant increase in charge carrier mobility by 2 orders of magnitudes. However, grain boundaries still exist even in such uniaxially oriented thin films which affect the properties of semiconductors and reduce the charge carrier transport. Hereby, both spin coating and dip coating were performed on untreated SiO_2 insulator surfaces. In this work, SVD was applied to further improve the structural order of DTBDT. Defect-free DTBDT crystal microribbons were fabricated on HMDS modified SiO_2 surface, exhibiting further improved charge carrier mobilities, one time higher than the device based on the dip coating films. Together with the example in chapter 3, this study on self-assembly of DTBDT into single crystals again verified that solvent vapor diffusion can be further exploited for a broad range of other (macro) molecular semiconductors and additionally bears potential for practical applications. In chapter 5, solvent vapor diffusion is further utilized for the single fiber growth of cyclopentadithiophene-benzothiadiazole copolymer.

REFERENCES

[1] K. Balakrishnan, A. Datar, W. Zhang, X. Yang, T. Naddo, J. Huang, J. Zuo, M. Yen, J. S. Moore, L. Zang, *J. Am. Chem. Soc.* **2006**, *128*, 6576.

[2] S. Xiao, J. Tang, T. Beetz, X. Guo, N. Tremblay, T. Siegrist, Y.i Zhu, M. Steigerwald, C. Nuckolls, *J. Am. Chem. Soc.* **2006**, *128*, 10700.

[3] A. L. Briseno, S. C. B. Mannsfeld, X. Lu, Y. Xiong, S. A. Jenekhe, Z. Bao, Y. Xia, *Nano Lett.* **2007**, *7*, 668.

[4] S. Berson, R. D. Bettignies, S. Bailly, S. Guillerez, *Adv. Funct. Mater.* **2007**, *17*, 1377.

[5] S. Samitsu, T. Shimomura, S. Heike, T. Hashizume, K. Ito, *Macromolecules,* **2010**, *43*, 7891.

[6]X. Mu , W. Song , Y. Zhang , K. Ye , H. Zhang , Y. Wang, *Adv. Mater.* **2010**, *22,* 4905.

[7] J. A. Lim, J. H. Kim, L. Qiu, W. H. Lee, H. S. Lee, D. Kwak, K. Cho, *Adv. Funct. Mater.* **2010**, *20,* 3292.

[8] F. S. Kim, G. Ren, S. A. Jenekhe, *Chem. Mater.* **2011**, *23,* 683.

[9] Y. Che, A. Datar, K. Balakrishnan, L. Zang, *J. Am. Chem. Soc.* **2007**, *129*, 7234.

[10] Q. Tang, H. Li, Y. Song, W. Xu, W. Hu, L. Jiang, Y. Liu, X. Wang, D. Zhu, *Adv. Mater.* **2006**, *18*, 3010.

[11] J. H. Oh, H. W. Lee, S. Mannsfeld, R. M. Stoltenberg, E. Jung, Y. W. Jin, J. M. Kim, J. Yoo, Z. Bao, *Proc. Natl. Acad. Sci.* **2009**, *106*, 6065.

[12] Y. Zhou, T. Lei, L. Wang, J. Pei, Y. Cao, J. Wang, *Adv. Mater.* **2010**, *22,* 14841.

[13] C. Liu , T. Minari , X. Lu , A. Kumatani , K. Takimiya , K. Tsukagoshi, *Adv. Mater.*, **2011**, *23*, 523.

[14] W. Jiang, Y. Zhou, H. Geng, S. Jiang, S. Yan, W. Hu, Z. Wang, Z. Shuai, J. Pei, *J. Am. Chem. Soc.* **2011**, *133*, 11.

[15] Md. M. Islam, S. Pola, Y. T. Tao, *Chem. Commun.* **2011**, *47*, 6356-6358.

[16] Y. Zhou, L. Wang, J. Wang, J. Pei, Y. Cao, *Adv. Mater.* **2008**, *20,* 3745.

[17] J. Liu, M. Arif, J. Zou, S. I. Khondaker, L. Zhai, *Macromolecules,* **2009**, *42,* 9390.

[18] R. Li, W. Hu, Y. Liu, D. Zhu, *Acc. Chem. Res.* **2010**, *43,* 529. (j) L. Jiang, H. Dong, W. Hu, *J. Mater. Chem.*, **2010**, *20*, 4994.

[19] R. Li, H. Dong, X. Zhan, Y. He, H. Li, W. Hu, *J. Mater. Chem.*, **2010**, *20*, 6014..

[20] Q. Tang, H. Li, M. He, W. Hu, C. Liu, K. Chen, C. Wang, Y. Liu, D. Zhu, *Adv. Mater.* **2006**, *18*, 65.

[21] D. J. Mascaro, M. E. Tompson, H. I. Simth, V. Bulovic, *Org. Electronics* **2005**, *6*, 211.

[22] K. C. Dickey, J. E. Anthony, Y. Loo, *Adv. Mater.* **2006**, *18*, 1721.

[23] H. Jiang, K. J. Tan, K. K. Zhang, X. Chen, C. Kloc, *J. Mater. Chem.* **2011**, *21*, 4771.

[24] O. D. Jurchescu, J. Baas, T. T. M. Palstra, *Appl. Phys. Lett.* **2004**, *84*, 3061. [25] Y. Takahashi, T. Hasegawa, S. Horiuchi, R. Kumai, Y. Tokura, G. Saito, *Chem. Mater.* **2007**, *19*, 6382.

[26] Th. B. Singh, N. S. Sariciftci, H. Yang, L. Yang, B. Plochberger, H.Sitter, *Appl. Phys. Lett.* **2007**, *90*, 213512-3.

[27] J. Takeya, M. Yamagishi, Y. Tominari, R. Hirahara, Y. Nishikawa, T. Kawase, T. Shimoda, S. Ogawa, *Appl. Phys. Lett.* **2007**, *90*, 102120-3.

[28] M. Leufgen, O. Rost, C. Gould, G. Schmidt, J. Geurts, L. W. Molenkamp, N. S. Oxtoby, M. Mas-Torrent, N. Crivillers, J. Veciana C. Rovira, *Org. Electronics* **2008**, *9*, 1101.

[29] D. Shukla, S. F. Nelson, D. C. Freeman, M. Rajeswaran, W. G. Ahearn, D. M. Meyer, J. T. Carey, *Chem. Mater.* **2008**, *20*, 7486.

[30] O. D. Jurchescu, S. Subramanian, R. J. Kline, S. D. Hudson, J. E. Anthony, T. N. Jackson, D. J. Gundlach, *Chem. Mater.* **2008**, *20*, 6733.

[31] L. Jiang, W. Hu, Z. Wei, W. Xu, H. Meng, *Adv. Mater.* **2009**, *21*, 3649.

[32] A. S. Molinari, H. Alves, Z. Chen, A. Facchetti, A. F. Morpurgo, *J. Am. Chem. Soc.* **2009**, *131*, 2462.

[33] S. H. Wang, L. Dössel, A. Mavrinskiy, P. Gao, X. L. Feng, W. Pisula, K. Müllen, *Small*, **2011**, *7*, 2841.

[34] P. Gao, D. Beckmann, H. N. Tsao, X. Feng, V. Enkelmann, M. Baumgarten, W. Pisula, K. Müllen, *Adv. Mater.*, **2009**, *21*, 213.

[35] L. Li, P. Gao, K. C. Schuermann, S. Ostendorp, W. Wang, C. Du, Y. Lei, H. Fuchs, L. D. Cola, K. Müllen, L. Chi, *J. Am. Chem. Soc.* **2010**, *132*, 8807.

[36] T. Izawa, E. Miyazaki, K. Takimiya, *Adv. Mater.* **2008**, *20*, 3388.

[37] S. Scheinert, G. Paasch, M. Schrödner, H.-K. Roth, S. Sensfuß, T. Doll, *J. Appl. Phys.* **2002**, *92*, 330.

[38] Y. Xu, F. Zhang, X. Feng, *Small* **2011**, *10*, 1338.(b) S. C. B. Mannsfeld, A. Sharei, S. Liu, M. E. Roberts, I. McCulloch, M. Heeney, Z. Bao, *Adv. Mater.* **2008**, *20*, 4044.

Chapter 5.

Organic Field-Effect Transistors Based on Highly Ordered Single Cyclopentadithiophene-Benzothiadiazole Copolymer Fibers

5.1 Introduction

As revealed in the former two chapters, **3.1** and **4.1** were self-assembled into highly ordered microstructures although both compounds showed low self-assembly tendency (the ability to self-assembly into highly ordered microstructures) when processed by conventional solution methods. Here, based on the understanding on optimizing the parameters in the microstructure evolution during SVD from the above mentioned examples, this chapter aims to further exploit SVD to deposit the conjugated polymers into highly ordered structures for high performance OFETs. It is worth to mention that as demonstrated in chapter 4, in contrast to OFETs based on organic thin films, single crystals possess higher molecular ordering and fewer grain boundaries, showing unprecedented performance in OFETs.[1-7] Hereby, one-dimensional (1D) organic polymer fibers are expected to reveal significantly enhanced charge carrier transport as a result of strong intermolecular coupling between closely packed molecules and of a lower density of structural defects.[8-11] For instance, in the case of P3HT single fibers, it is observed that the molecules are packed with π-π stacking direction perpendicular to the length axis of the crystals and main chains parallel to the substrate, showing a significantly improved charge carrier mobility in comparison to the low ordered thin films.[12] On the other hand, it is necessary to note that although crystallinity is of vital importance in determining the device performance of small conjugated molecules,[13] it seems to play a less essential role for macromolecules since macroscopically low ordered polymers recently reached values above 0.5 cm²/Vs.[14, 15] Thereby, one has to keep in mind that in organic macromolecular semiconductors the fast charge transport takes place along the backbone,[16] while the limiting factor for the bulk electronic properties is the hopping between the conjugated backbones. This behavior has been not only observed for isolated polymer chains, but also in macroscopically oriented thin films, which are obtained e.g. by pre-aligned PTFE or by a concentration gradient, where typically higher mobilities were determined in the direction of the backbones. [17]

5.2 Self-assembly Control of Copolymer Fibers

In this chapter, OFET applications were studied based on a high performance donor-acceptor copolymer system in self-assembled single fibers fabricated via solvent vapor diffusion. It is proven that inside the single fibers the polymer chains are highly oriented in the direction of the charge carrier transport. Cyclopentadithiophene-benzothiadiazole copolymer (CDT-BTZ, **5.1**, Mn = 50K using PS/THF standards, Figure 5.1a) was chosen due to its outstanding device performance in low structurally ordered thin films.[18-20] Moreover, **5.1** with Mn=50K showed fibrous structures directly after dip coating. [14] Such a morphology yielded hole mobilities as high as 1.4 cm²/Vs. Therefore, **5.1** “Mn=50K” is chosen as a good candidate for single fiber growth and application in high performance single fiber OFETs. Here, solvent vapor diffusion is applied, to tune the molecular self-assembly of **5.1** on the surface yielding single copolymer fibers of controlled dimensions. In order to grow single fibers on the surface, the self-assembly of **5.1** is firstly studied using drop casting and solvent vapor annealing.

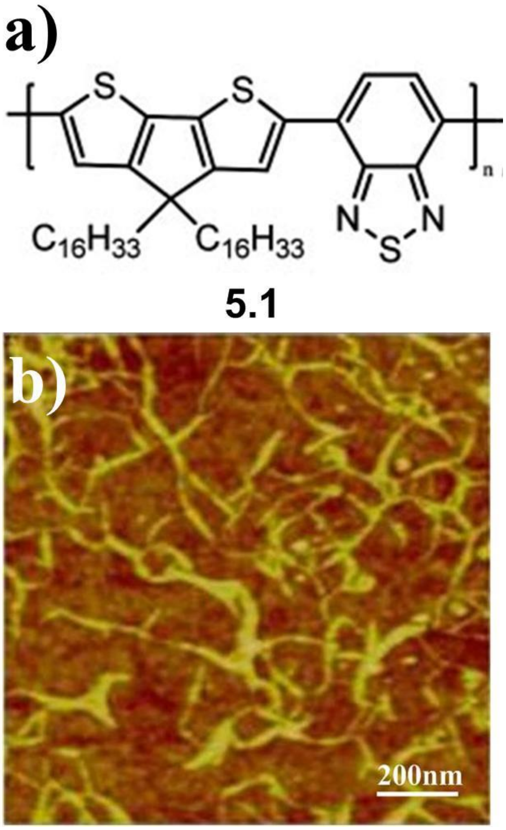

Figure 5.1. a) Molecular structure of cyclopentadithiophene-benzothiadiazole (CDT-BTZ, **5.1**). In this work **5.1** with Mn of 50K (PS/THF standards) has been used. b) AFM image of **5.1** nanofibers grown after drop casting on SiO_2 substrate at concentrations of 0.001 mg/ml.

The employment of SVD was necessary since all other solution-based procedures described above generate only fibers within a nanometer range and of large size distribution. For instance, drop casting **5.1** at low concentrations, like 0.001mg/ml, at ambient temperatures on a SiO_2 substrate leads after solvent evaporation to such nanometer scaled fibers. The representative atomic force microscopy (AFM) image in Figure 1b reveals an average diameter of approximately 10 nm, while the fiber length varies from a few nanometers to several tens of nanometers. Such a fiber microstructure is not applicable in single fiber OFET devices due to inhomogeneous and too small object dimensions. Moreover, it is also not favorable for thin film OFET devices due to the pronounced grain boundaries which serve as trapping sites for charge transport. Reducing the solvent evaporation rate by simply adding a cover over the droplet does not distinctly change the film microstructure. Solvent vapor annealing (SVA) of the drop cast film also does not improve the surface microstructure (Figure 5.2). Here it should be emphasized that SVA is normally used to trigger the rearrangement of the molecules in disorderd microstructures.[6] However, SVA as a post deposition treatment could not boost the molecular order in the well-defined fibrous structures, in which the intermolecular interactions are well balanced.[7] Previously SVA was applied to the spin coated fibers of hexa-peri-hexabenzocoronenes (HBCs). [7] It was observed that instead of increasing the fiber dimensions, HBCs fibers disappeared after SVA and the surface was substituted by aggregated islands.[7] Figure 5.2d shows a similar aggregation tendency. The fibrous structures are partially broken and islands with spherical structures appeared on the surface. Since these post-treatments fail to enhance the film microstructure of **5.1**, the formation of defined fibers can only be achieved during the solvent evaporation process.

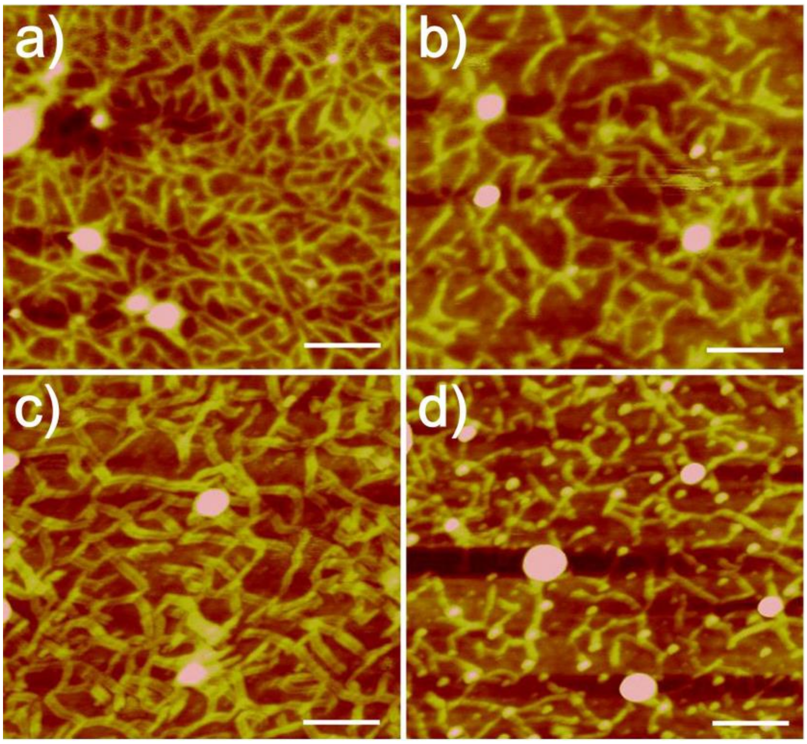

Figure 5.2. AFM images solvent vapor annealing of the drop cast film by different solvent: a) THF, b) chloroform, c) hexane, d) toluene. The scale bar is corresponding to 500nm.

Therefore, SVD is employed which can provide fine adjustment of the solution evaporation rate simply by the right choice of the saturated solvent vapor. This opens the opportunity to excellently balance dewetting effects and intermolecular forces including solvent-molecule, solvent-substrate, and molecule-substrate interactions for the desired microstructure and polymer organization on the surface. These effects have been previously proven on the example of different conjugated semiconductors for which the surface microstructure was modified by using similar approaches. [22-27]

Through a careful choice of solvent, concentration, vapor atmosphere, finally dichlorobenzene was chosen as good candidate for both solvent and solvent vapor. Several droplets of a 0.05 mg/ml dichlorobenzene solution of **5.1** were drop cast on a SiO_2 surface which was exposed to saturated solvent vapor atmosphere in an airtight container. The container was kept at 60 ^{o}C to ensure a saturated vapor atmosphere. Hereby, the solvent vapor significantly reduces the evaporation rate of the solution, providing the molecules more time for the self-assembly and sufficient mobility to reach high structural order.

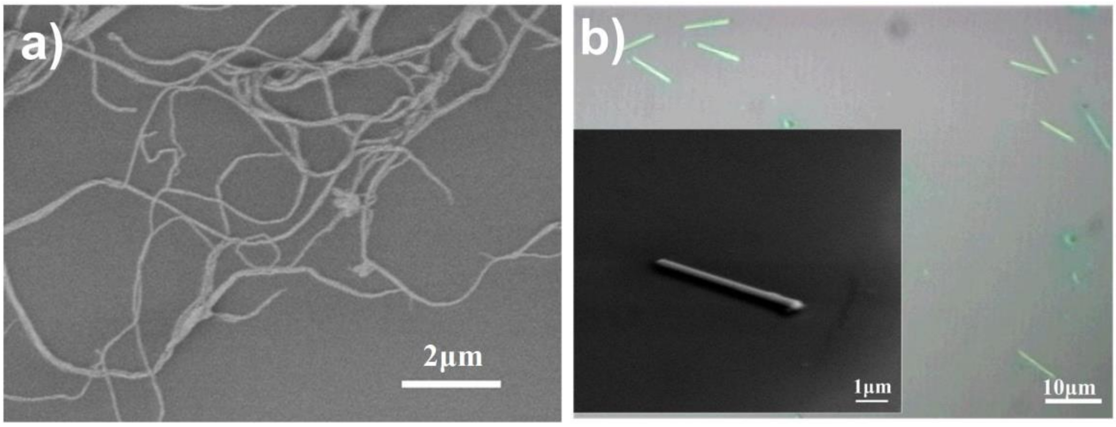

Figure 5.3. a) SEM image of **5.1** self-assembly on a SiO_2 substrate, b) optical microscopy image of **5.1** fibers self-assembled on HMDS treated SiO_2 substrate (inset: SEM image of single **5.1** fiber on HMDS treated SiO_2 substrate).

The scanning electron microscopy (SEM) image in (Figure 5.3a) displays fibrils of **5.1** composed of entangled nanofibers and bundles which are formed on bare Si wafers. A self-assembled monolayer of hexamethyldisilazane (HMDS) was deposited from the vapor phase to achieve a natural affinity of the substrate with the **5.1** molecules by reducing the surface energy. This treatment changes the microstructure and leads to well-defined fibers which are ideal for OFET applications (Figure 5.3b). The typical SVD fiber dimensions under these processing conditions are: width between 0.3 μm and 0.6 μm, thickness between 80 nm and 150 nm, and length from 5 μm to 20 μm. One should keep in mind that such fiber dimensions are suitable for charge transport studies, and the method is simple compared to the previously reported conjugated polymer fibers which were prepared by complicated template-assisted synthesis, and nanolithography directly from solution processing.[28] Recently, fibers based on poly(3-octylthiophene) (P3OT) were successfully obtained by controlling solvent evaporation.[12] The structural analysis indicated the π-π stacking direction perpendicular to the current flow direction and the main chains parallel to the substrate. It is noteworthy to mention that an effective mobility of 0.62 $cm^2V^{-1}s^{-1}$ was obtained for the OFETs based on P3OT single fiber. This is a significant contrast to the corresponding P3OT thin film transistors which showed a much lower mobility on the order of 10^{-3} $cm^2V^{-1}s^{-1}$. A high anisotropy ratio over 2 orders of magnitude was observed, indicating the charges transport preferentially along the backbone direction.

5.3 Structural analysis for single fibers

Deeper insight into the macromolecular organization is obtained from selected area electron diffraction (SAED) for one single fiber (Figure 5.4a, 5.4b). No change in the SAED pattern is observed for different parts of the same fiber. The pattern reveals two distinct reflections which are attributed to the π-stacking distance of 0.37 nm between packed polymer chains. An identical value has been determined for the bulk material.[14] The strong anisotropy of the reflections indicates pronounced alignment of the backbones along the fiber axis which is considered to be favorable for the charge carrier transport in the same direction (see schematic illustration in Figure 5. 4c). Additional scattering intensities around the spacing of 0.43 nm are related to ordered alkyl side chains and suggest higher overall crystallinity in the fiber. Characteristically, the side chains of **5.1** in bulk and thin film are disordered and appear as an amorphous halo in the diffraction pattern.[14] This stands in contrast to the self-assembled SVED fibers in which apparently a significantly higher crystallinity is reached and in which the alkyl chains are highly ordered in the periphery of the conjugated backbones.

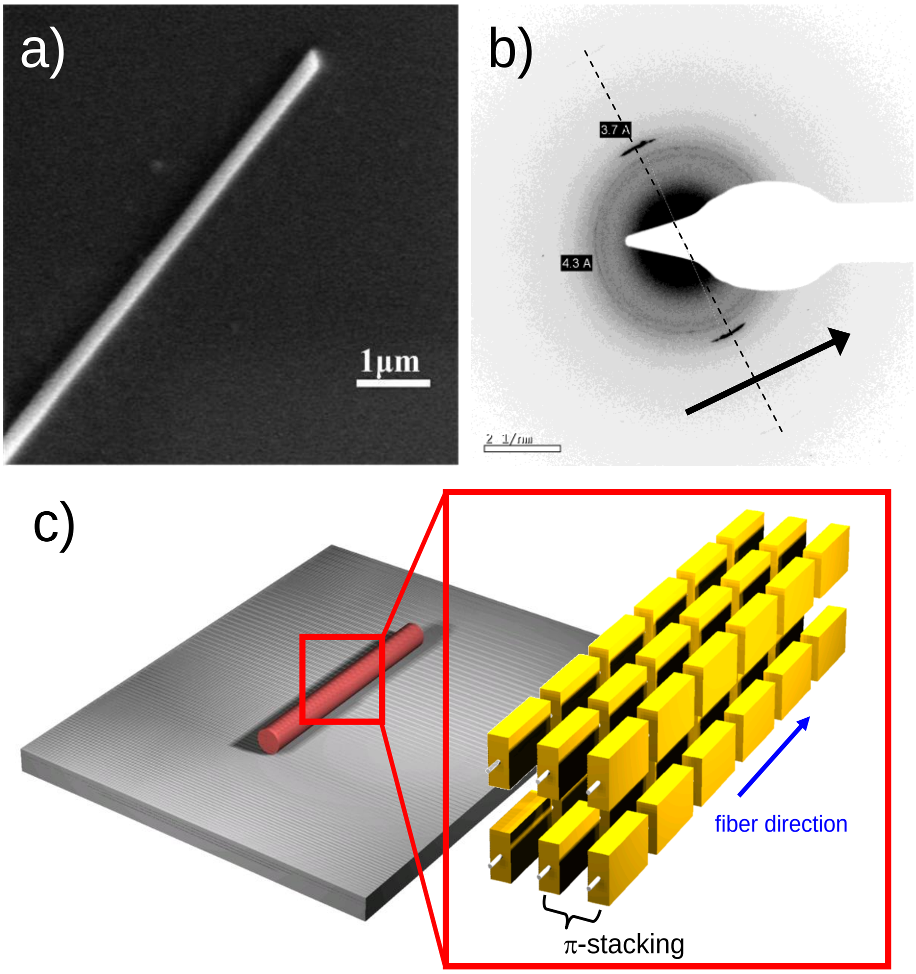

Figure 5.4. Analysis of single **5.1** fiber on HMDS: a) SEM and b) SAED (arrow indicates the fiber axis), c) schematic illustartion of the polymer organization in the SVED fiber.

5.4. Transistors based on single copolymer fibers

Transistor substrates consisting of highly n-doped Si wafers were covered by 300 nm of SiO_2 on top. Before depositing electrodes, the SiO_2 surface was functionalized with HMDS to induce single fiber growth and to minimize interfacial trapping sites for charges during device operation. For contacting, Au electrodes were deposited on the surface around the polymer fibers with distances of 25 µm (Figure 5.5a). This distance is much larger than the fiber length. Focused ion beam (FIB) is usually used to fabricate small channel length devices. Previously, FIB has been successfully applied to connect two terminal devices of C60 nanorods. [29]OFETs based on individual **5.1** copolymer fiber were fabricated by embedding an individual fiber between two Pt electrodes using FIB (see experimental details in chapter 10),[29, 30] which were connected with the Au electrodes, as shown in Figure 5b with a transistor channel length of 3 µm and width of 0.3 µm in this case.

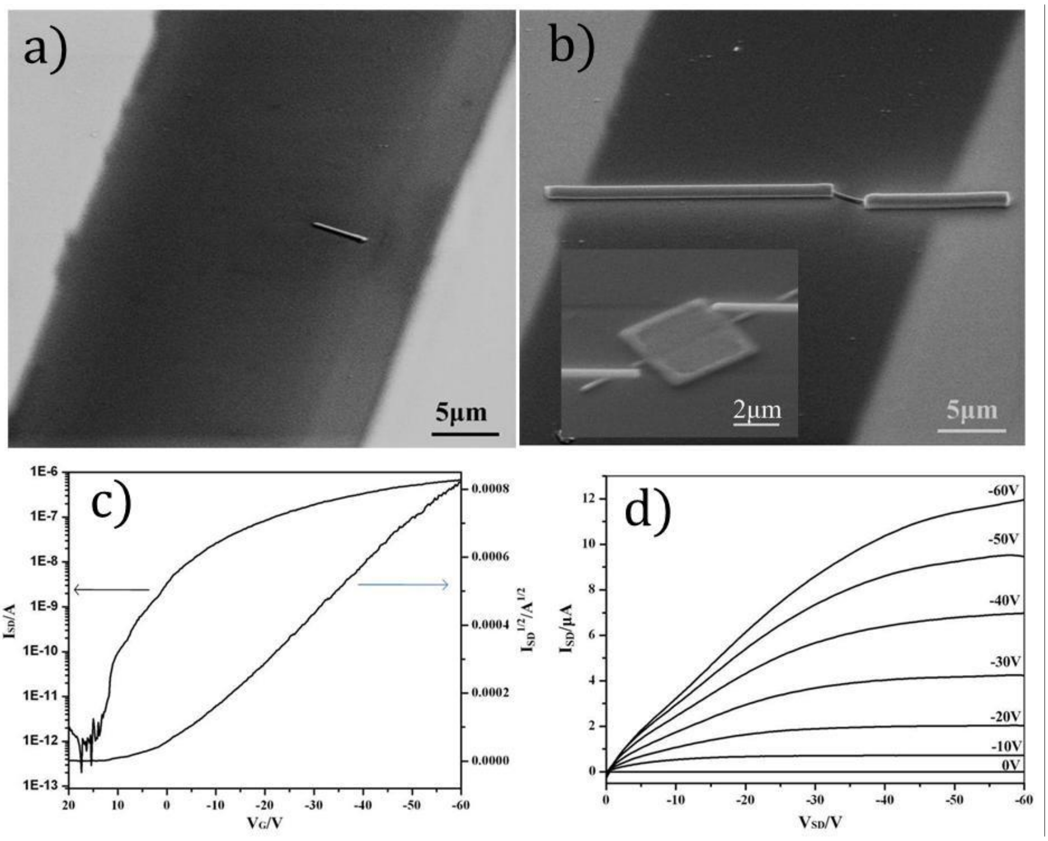

Figure 5.5. a) SEM images a) before and b) after FIB contact deposition (Inset: the middle part of the **5.1** fiber was covered with a 3µm × 3µm patch of SiO_2 with a

thickness of 60 nm), c) transfer curve at source-drain voltage VSD=-60 V, d) output curves at various gate voltages V_G for the single **5.1** fiber OFETs.

All tested devices exhibited p-type transistor behavior as determined under glove-box conditions after annealing at 200 °C for 2h in nitrogen atmosphere. Excellent hole mobilities of (3.3±0.3) $cm^2V^{-1}s^{-1}$, and on/off ratios of 10^6 were obtained. The best device exhibited a hole mobility of 4.6 $cm^2V^{-1}s^{-1}$. Here it should be also emphasized that gas assisted FIB deposition of Pt always creates a very thin layer of Pt that extends beyond the area of the write pattern of the ion beam. In order to exclude any influence of this overspray, a major part of the **5.1** fiber is covered with a 3 µm × 3 µm patch of SiO_2 with a thickness of 60 nm (also achieved by gas assisted FIB deposition). In this way the fibers are additionally protected from oxygen during the transfer from the FIB to the glovebox. The SiO_2 covered transistors were measured under the same conditions as the uncovered ones, with an average mobility of 4.3 $cm^2V^{-1}s^{-1}$ and the highest value as high as 5.5 $cm^2V^{-1}s^{-1}$. Standard transfer and output curves are shown in Figure 5.5c and 5.5d. The effect of the contact resistance is indicated by the output curves and the slight hysteresis in the transfer curve (Figure 5.6) and is expected to have a limiting influence on the charge carrier injection leading most probably to an underestimation of the device performance.

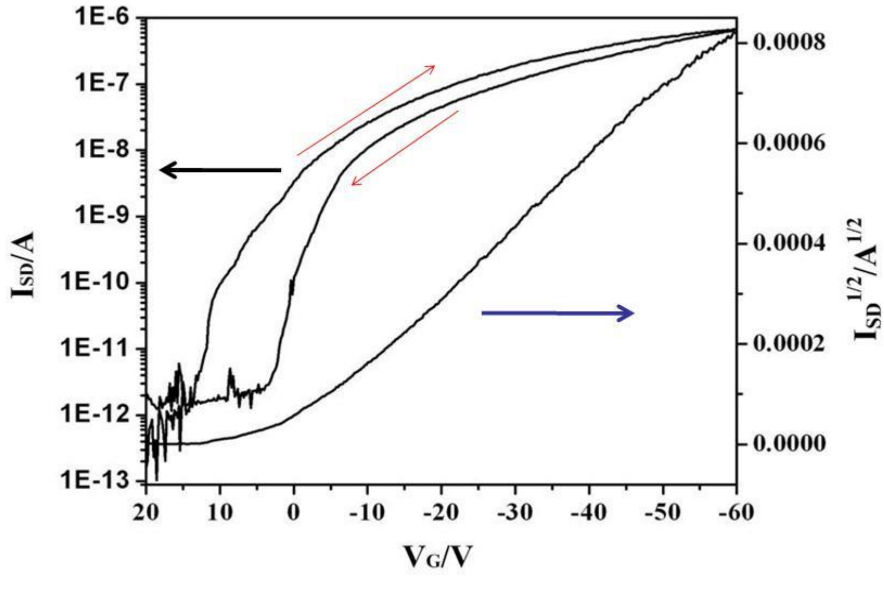

Figure 5.6. The Hysteresis of the transfer curve corresponding to Figure 5.5c.

Moreover, all transistors exhibited a low threshold voltage of (10±2) V. The low off-current and the high on/off ratio confirm no connection of the deposited Pt electrodes by overspray. For comparison, the copolymer with the same Mn reveals charge carrier mobilities of 0.67 $cm^2V^{-1}s^{-1}$ after spin-coating and 1.4 $cm^2V^{-1}s^{-1}$ after directional alignment by dip-coating.[14] Since the π-stacking distance remains unchanged in the fiber compared to macorscopically low ordered polymer films, the remarkable increase in mobility is related to four main factors: 1) high molecular order; as in a crystal, the increased crystallinity in the fiber is especially obvious for the alkyl side chains appearing as sharp reflections in the electron diffraction pattern leading to a decrease of structural defects as trapping sites. 2) In conjugated polymers the charge migration is much faster along the backbone. [31, 32] Therefore, the alignment of **5.1** backbones along the fiber axis favors the charge carrier transport in the same direction. 3) The number of structural defects is additionally reduced due to the relatively short transistor channel promoting an undistributed charge carrier transport between the electrodes. 4) An additional improvement is achieved by the SiO_2 protection layer deposited on top of the **5.1** fiber.

5. 5 Conclusion

In conclusion, high mobility OFETs based on a CDT-BTZ donor-acceptor copolymer have been fabricated by reaching high molecular order and pronounced alignment in single fibers within a short OFET channel via solvent vapor diffusion. In comparison, the macroscopically low ordered thin films, in which the polymer chains are arranged in a rather random fashion, the macromolecules directionally self-assemble during SVD in a quasi crystal-like order in the fibers providing in this way an unhindered charge carrier pathway with mobilities as high as 5.5 $cm^2V^{-1}s^{-1}$. It is assumed that this strategy is also applicable to other high performance conjugated polymers which form typically disordered thin films after traditional solution processing. Different processing methods are compared for their influence on the film morphology and molecular packing on the surface, which then determine the device performance of transistors. As is shown in Figure 5.7, spin coating results in polymer films with a high density of disordered patches which act as structural trapping sites on the surface. In comparison, the morphology and molecular packing are improved via dip coating, and a fibrous structure could be observed along the dip coating direction, which leads to a two fold increase in charge carrier mobility. In this work, SVD was applied to further improve the structural order of **5.1**. Polymer single fibers with high molecular order and pronounced alignment were fabricated, exhibiting charge carrier mobilities three times higher than the device based on the dip coating films.

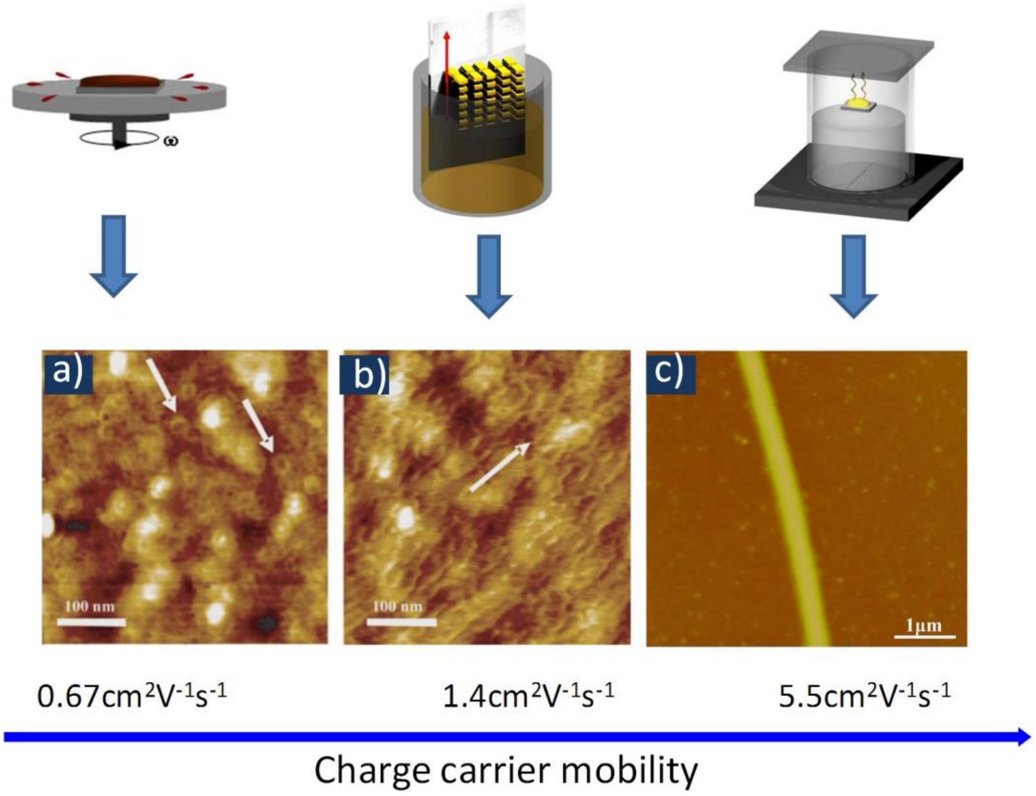

Figure 5.7. Influence of different processing methods on the film morphology and the corresponding charge carrier mobilities. a) Spin coating b) dip coating, and c) solvent vapor diffusion.

Here it is also important to note that the self-assembly of polymers strongly depends on the design of the backbone and the attached substituents, as well as the molecular weight of the polymer. It is reported that polymer chain length dictates the morphology, [33] thus determing the device performance. The same macromolecule with different molecular weights could show significantly different morphologies. [33] For instance in the well recognized case of P3HT, under the same processing method, crystalline fibers are formed for small molecular weight. However, nodular structures are formed for higher molecular weight. [34] As a result, differences in the development of the film morphology could be expected for other molecular weights for **5.1**. Interestingly, when changing the molecular weight from 50k to 28k, a quite similar microstructure was obtained after SVD with all other parameters unchanged. From the OM image shown in Figure 5.8, it can be clearly observed that 1D fiber/ribbon nuclei start to appear on the substrate. But in comparison to the fibers obtained from 50k, the fibers in Figure 5.8 are much shorter, and not well-defined in size. Unfortunately, these fibers are too short for OFET fabrication via focused ion beam.

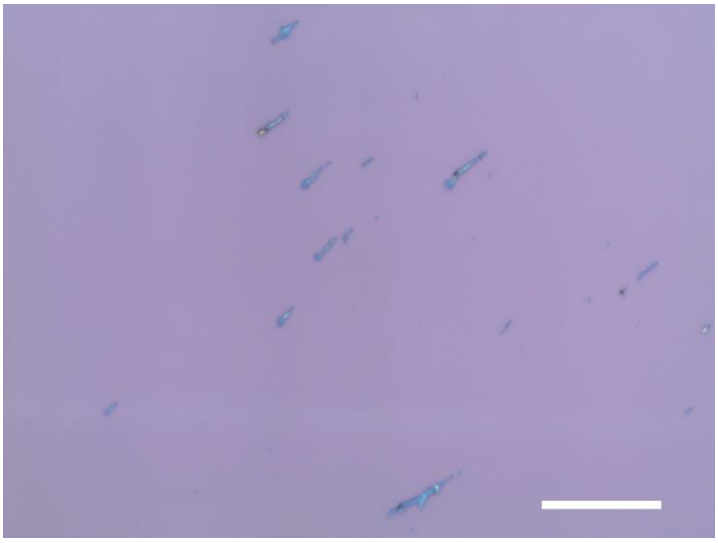

Figure 5.8. Optical microscopy image of **5.1** fibers self-assembled on HMDS treated SiO_2 substrate (Mn= 28K).The scale bar is related to 10μm.

In comparison to other 1D objects such as carbon nanotubes, polymer fibers possess advantages, such as diversity of the molecular structures which can be adapted to the requirements of specific device applications. One challenge for future work is a further applicability of this basic idea in a fast continuous process for practical applications in fabrication. Especially, technical questions concerning micromanipulation and precise positioning of high performance mesoscopic fibers on more complex circuits in multi-array devices must be answered. An implementation of such high-performance polymer fibers in multi-array devices requires surface patterning to accurately place and align the objects towards the contacts. [35, 36]

REFERENCES

[1] Q. Tang, H. Li, Y. Song, W. Xu, W. Hu, L. Jiang, Y. Liu, X. Wang, D. Zhu, *Adv. Mater*. **2006**, *18*, 3010.

[2] J. H. Oh, H. W. Lee, S. Mannsfeld, R. M. Stoltenberg, E. Jung, Y. W. Jin, J. M. Kim, J. Yoo, Z. Bao, *Proc. Natl. Acad. Sci.* **2009**, *106*, 6065.

[3] Y. Zhou, T. Lei, L. Wang, J. Pei, Y. Cao, J. Wang, *Adv. Mater.* **2010**, *22*, 14841.

[4] C. Liu , T. Minari , X. Lu , A. Kumatani , K. Takimiya , K. Tsukagoshi, *Adv. Mater.*, **2011**, *23*, 523.

[5] W. Jiang, Y. Zhou, H. Geng, S. Jiang, S. Yan, W. Hu, Z. Wang, Z. Shuai, J. Pei, *J. Am. Chem. Soc.* **2011**, *133*, 11.

[6] G. De Luca, W. Pisula, D. Credgington, E. Treossi, O. Fenwick, G. M. Lazzerini, R. Dabirian, E. Orgiu, A. Liscio, V. Palermo, K. Müllen, F. Cacialli, P. Samorì, *Adv.Funct. Mater.* **2011**, *21*, 1279.

[7] E. Treossi, A. Liscio, X. Feng, V. Palermo, K. Müllen, P. Samorì, *Small*, **2009**, *1*, 112.

[8] K. Balakrishnan, A. Datar, R. Oitker, H. Chen, J. Zuo, L. Zang, *J. Am. Chem. Soc*. **2005**, *127*, 10496.

[9] M. D. Curtis, J. Cao, J. W. Kampf, *J. Am. Chem. Soc.* **2004**, *26*, 4318.

[10] K. Xiao, J. Tao, Z. Pan, A. A. Puretzky, I. N. ivanov, S. J. Pennycook, D. B. Geohegan, *Angew. Chem. Int. Ed.* **2007**, *46*, 2549.

[11] J. H. Liu, M. Arif, J. H. Zou, S. I. Khondaker, L. Zhai, *Macromolecules*, **2009**, *42*, 9390.

[12] X. L. Xiao, Z. B. Wang, Z. J. Hu, T. B. He, *J. Phys. Chem. B* **2010**, *114*, 7452.

[13] C. Liu , T. Minari , X. Lu , A. Kumatani , K. Takimiya , K. Tsukagoshi, *Adv. Mater.*, **2011**, *23*, 523.

[14] H. N. Tsao, D. Cho, J. W. Andreasen, A. Rouhanipour, D. W. Breiby, W. Pisula, K. Müllen, *Adv. Mater.* **2009**, *21*, 209.

[15] H. N. Tsao, D. Cho, I. Park, M. R. Hansen, A. Mavrinskiy, D. Y. Yoon, R. Graf, W. Pisula, H. W. Spiess, K. Müllen, *J. Am. Chem. Soc.* **2011**, *133*, 2605.

[16] P. Prins, F. C. Grozema, J. M. Schins, S. Patil, U. Scherf, L. D. A. Siebbeles, *Phys. Rev. Lett.* **2006**, *96*, 146601.

[17] W. Pisula, M. Zorn, J. Y. Chang, K. Müllen, R. Zentel, *Macromol. Rapid Commun*. **2009**, *30*, 1179.

[18] J. Y. Liu, R. Zhang, G. Sauve, T. Kowalewski, R. D. McCullough, *J. Am. Chem. Soc.* **2008**, *130*, 13167.

[19] W. Zhang, J. Smith, S. E. Watkins, R. Gysel, M. McGehee, A. Salleo, J. Kirkpatrick, S. Ashraf, T. Anthopoulos, M. Heeney, I. McCulloch, *J. Am. Chem. Soc.* **2010**, *132*, 11437.

[20] H. Yan, Z. Chen, Y. Zheng, C. Newman, J. R. Quinn, F. Dotz, M. Kastler, A. Facchetti, *Nature*, **2009**, *457*, 679.

[21] C. Chen, S. Chan, J. Li, K. Wu, H. Chen, J. Chen, W. Huang, S. Chen, *Macromolecules*, **2010**, *43*, 7305.

[22] S. H. Wang, L. Dössel, A. Mavrinskiy, P. Gao, X. L. Feng, W. Pisula, K. Müllen, *Small*, **2011**, *7*, 2841.

[23] D. H. Kim, J. T. Han, Y. D. Park, Y. Jang, J. H. Cho, M. Hwang, K. Cho, *Adv. Mater*. **2006**, *18*, 719.

[24] X. L. Xiao, Z. J. Hu, Z. B. Wang, T. B. He, *J. Phys. Chem. B* **2009**, *113*, 14604.

[25] H. E. Katz, T. Siegrist, M. Lefenfeld, P. Gopalan, M. Mushrush, B. Ocko, O. Gang, N. Jisrawl, *J. Phys. Chem. B* **2004**, *108*, 8567.

[26] L. Zeng, F. Yan, S. K. H. Wei, S. W. Culligan, S. H. Chen, *Adv. Funct. Mater.* **2009**, *19*, 1978.

[27] J. Park, S. Lee, H. H. Lee, *Organic Electronics* **2006**, *7*, 256.

[28] K. C. Dickey, J. E. Anthony, Y. Loo, *Adv. Mater.* **2006**, *18*, 1721.

[29] H. X. Ji, J. S. Hu, L. J. Wan, Q. X. Tang, W. P. Hu, *J. Mater. Chem.* **2008**, *18*, 328.

[30] Y. Long, K. Huang, J. Yuan, D. Han, L. Niu, *Appl. Phys. Lett.* **2006**, *88*, 162113.

[31] P. Prins, F. C. Grozema, J. M. Schins, S. Patil, U. Scherf, L. D. A. Siebbeles, *Phys. Rev. Lett.*, **2006**, *96*, 146601.

[32] P. Prins, F. C. Grozema, L. D. A. Siebbeles, *Phys. Chem. B,* **2006**,*110*, 14659.

[33] H. N. Tsao, K. Müllen, *Chem. Soc. Rev.*, **2010**, *39*, 2372.

[34] R. J. Kline, M. D. McGehee, E. N. Kadnikova, J. Liu, J. M. J. Fréchet, *Adv. Mater.* **2005**, *15*, 1519.

[35] S. C. B. Mannsfeld, A. Sharei, S. Liu, M. E. Roberts, I. McCulloch, M. Heeney, Z. Bao, *Adv. Mater.* **2008**, *20*, 4044.

[36] Y. Xu, F. Zhang, X. Feng, *Small* **2011**, *10*, 1338.

Chapter 6.

Probing the Key Role of the First Monolayer in Solution Processed Polymeric Field-Effect Transistors

6.1 Introduction

Ultrathin film OFETs with few semiconducting monolayers are of vital importance, because charge carriers are directly transported to conduction channels without diffusion through a dense film. For small conjugated molecules [1-9] and very recently for a conjugated polymer [10] it has been proven that the main charge carrier transport in transistors occurs in few molecular layers near the dielectric surface. This is also in line with theory which predicts high density of charges and thus of the charge carrier mobility in the first few nanometers of the active film. [11] Therefore, particular emphasis was put on the molecular order within this thin accumulation layer processed e.g. by vacuum deposition [2, 6], LB deposition [3], and electrostatic force-based self-assembly. [4] However, vacuum deposition typically yields discontinuous patches due to 3D island growth. The LB technique and the electrostatic force-based self-assembly are restrcited to compounds with special functional groups (e.g. compounds with amphiphilic groups are usually required for LB technique). This requirement may compromise molecular packing and device performance. Little is known about the influence of solution processing, which is considered to be the future process in roll-to-roll fabrication of electronic devices, on the molecular organization in ultrathin films after solvent evaporation.

There are only few studies for conjugated polymers in ultra-thin film FETs, consisting of multilayers of poly (3-hexylthiophene) [12, 13,15] and polydiacetylene [14]. Both cases showed a performance being inferior to their corresponding thick film OFETs, proving a long way to potential applications. It is a great challenge to fabricate conjugated polymers into one single monolayer and its subsequent layers directly on the surface by solution processing. Therefore such work is so far rarely reported. Especially, the first question concerning how to process conjugated polymers from monolayer to multilayer still needs to be answered. This would allow a fundamental study of the role of the first monolayer on the evolution of the bulk polymer microstructure and the charge carrier transport in the transistor.

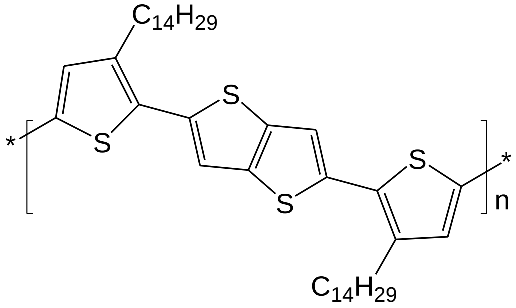

Scheme 6.1. Molecular structure of **PBTTT**, compound **6.1**

Therefore, in this chapter, ultrathin films from monolayer to multilayer were fabricated with a controllable growth via facile solution processing. As model compound, well-known high performance p-type polymer (PBTTT, Scheme 6.1, compound **6.1**) has been used. [4] Here it has to be noted that PBTTT possesses a liquid crystalline state. OFETs devices based on simply heating the spin-coated PBTTT film up to the liquid crystalline state and cooling down to room temperature gave hole mobilities up to 0.6 $cm^2V^{-1}s^{-1}$. [4] The corresponding XRD study indicated better molecular packing for liquid crystalline mediated films. This was also verified by the AFM images that larger domain sizes were observed for the liquid crystalline films than that for films prior to the heating treatment. [4]

In this chapter, a monolayer and its subsequent microstructure of **6.1** on a rigid OFET surface are successfully obtained from solution. It is proven that the first monolayer has essential importance for the bulk microstructure evolution, whereby a critical multilayer network is necessary for creating the required percolation pathways for the charge carriers in thin film polymer OFETs. Remarkably, at a low dip coating speed, the polymer chains are uniaxially oriented, yielding pronounced structural anisotropy and high charge carrier mobilities in the alignment direction.

6.2 Controllable growth of polymer monolayer

During the dip coating process, the pulling speed was gradually changed and had a great impact on the growth of **6.1**, mainly on the network density in the corresponding molecular layers, as well as on the morphology development. Remarkably, monolayers and subsequent networks were formed over large areas by dip coating, as proven by AFM images (Figure 6.2).

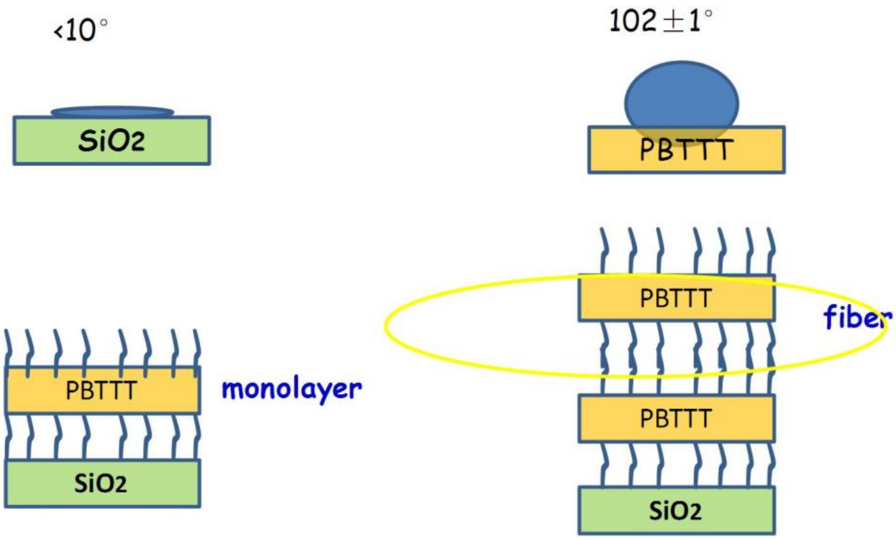

Figure 6.1. Schematic illustration for the striking difference between the first and the subsequent microstructure.

As shown in Figure 6.3a and 6.4a, a discontinuous monolayer network of **6.1** of a thickness of 1.8 nm is formed on SiO_2 surface when pulling the substrate at the highest speed of 1 mm/s. This height is in agreement with the chain-to-chain distance determined by X-ray scattering for a bulk film (see below). On top of this 2D monolayer, 1D fiber nuclei (thickness of 4-6 nm) start to grow, only on top of the **6.1** monolayer and not on SiO_2 surface (Figure 6.2a). This is noteworthy since the subsequent microstructure begins to develop while the first monolayer is not fully established (approx. 30% coverage). Moreover, a striking difference between the first and the subsequent microstructure is obvious, which is attributed to the different surface tension of **6.1** molecules and SiO_2. The difference of the contact angle is <10° for SiO_2 and 102±1° for the **6.1** layer. More precisely, in comparison to bare SiO_2 surface, long alkyl chains of **6.1** lead to stronger hydrophobic interactions between the deposited polymer and the first layer. [17, 18] As a result, **6.1** self-assembles into isolated anisotropic 1D fibers on top of the first monolayer (Figure 6.1). The occurance of different morphologies in the first monolayer and the subsequent microstructures is similar to the previous findings on small molecules. [6, 19] For instance in the case of pentacene, the first monolayer shows higher nucleation density than the subsequent monolayers, since the diffusion coefficient of pentacene molecules on SiO_2 is lower than that on pentacene. [19]

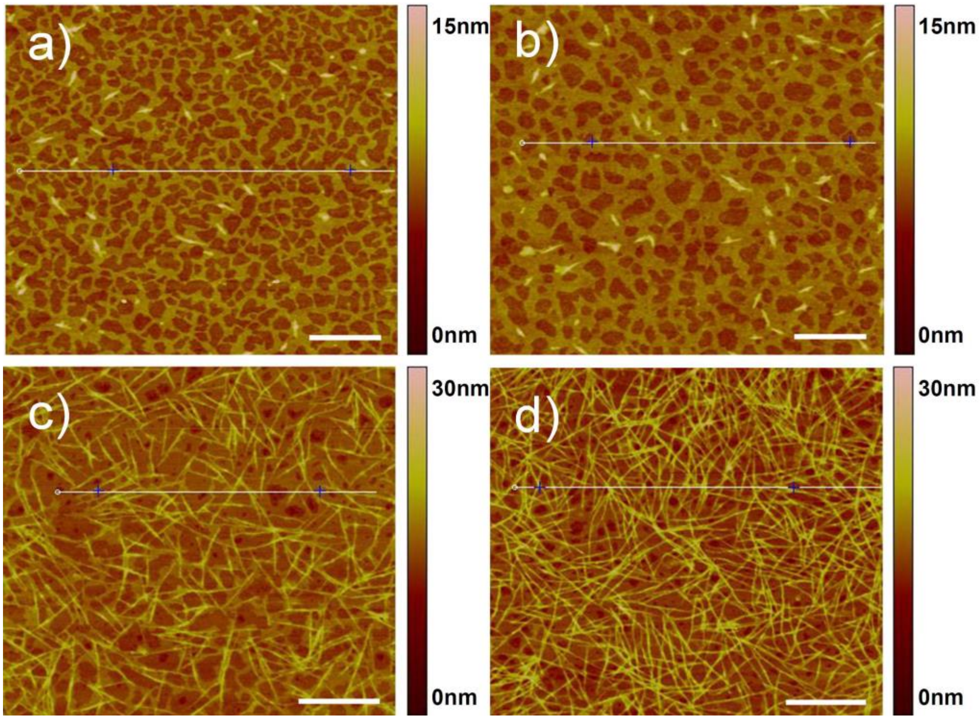

Figure 6.2. Tapping-mode AFM images of **6.1** on SiO_2 surface obtained by dip coating under different pulling speeds: a) 1 mm/s, b) 200 µm/s, c) 40 µm/s, and d) 10 µm/s. In a) and b), the scale bar corresponds to 500 nm; in c) and d), the scale bar corresponds to 1 µm. The line in each AFM image corresponds to height profiles in Figure 6.3.

6.3 Controllable growth of Polymer multilayers and their application in OFETs

The well-controlled growth of the polymer film allows a systematic investigation of the charge carrier transport in the charge accumulation and transporting layer of an OFET. Details of the device fabrication are described in the experimental part in chapter 11. The OFET devices were studied only in a top-contact configuration to exclude differences in surface energy between bottom Au electrodes and the SiO_2 surface to avoid any discontinuities in the film. For instance, in the case of untreated SiO_2, nucleation of pentacene takes place preferentially at the electrodes, which causes discontinuities and clustering in the pentacene film.[6] Almost no field-effect characteristics (<10^{-6} cm^{2}V^{-1}s^{-1}) are observed for the monolayer shown in Figure 2a. It has to be emphasized that a prerequisite for efficient charge carrier transport is a continuous long-range percolation path between the source and drain electrode with intimately connected molecules. However, this is not the case for the layer in Figure 6.2a.

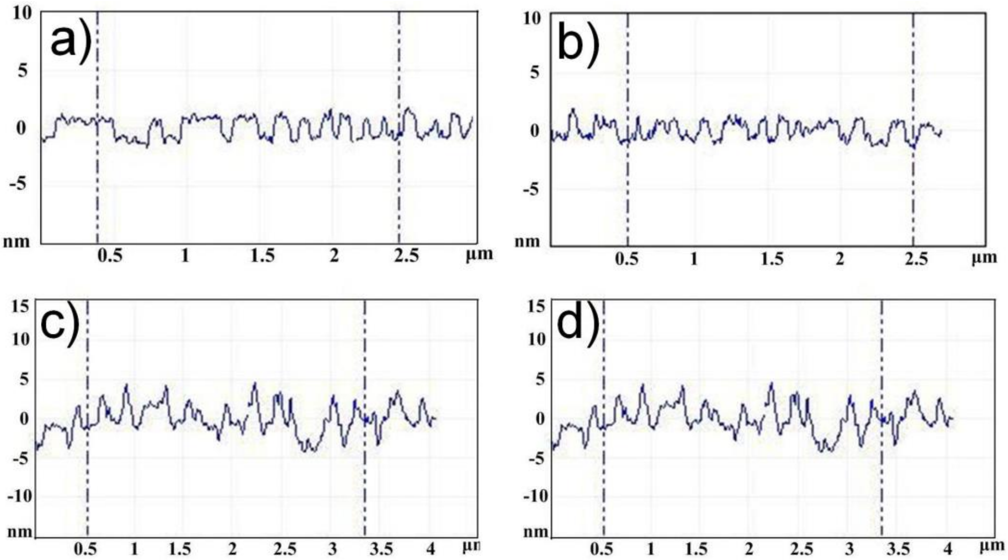

Figure 6.3. Height plots for the corresponding AFM images in Figure 6.3.

Lowering the pulling speed to 200 µm/s leads to a larger area covered by the first monolayer and therefore a more continuous film (Figure 6.2b and Figure 6.3b). In addition, the subsequent fiber nuclei (thickness does not change) become longer, but are still not interconnected. The extended first monolayer and grown subsequent fiber nuclei are attributed to the lower substrate speed which ensures more molecules for building up of the microstructures on the SiO_2 surface. It is also known from literature that only an ineffective connection between the electrodes and a single layer of molecules can be achieved limiting the charge carrier injection.[20, 21] These are the reasons for a low charge carrier mobility of 1.6×10^{-4} cm^{2}V^{-1}s^{-1} and an on/off ratio of ~10^2 for the corresponding transistor (Figure 6.4). A further proof of an ineffective charge carrier injection is the relatively high threshold voltage of -20 V. These results are in agreement to previous findings which showed that a monolayer of a small molecular semiconductor is not sufficient for a high performance.[20, 21] Despite the low performance, we define this mobility as an on-set value for a minimal film thickness/microstructure of **6.1** for a working transistor.

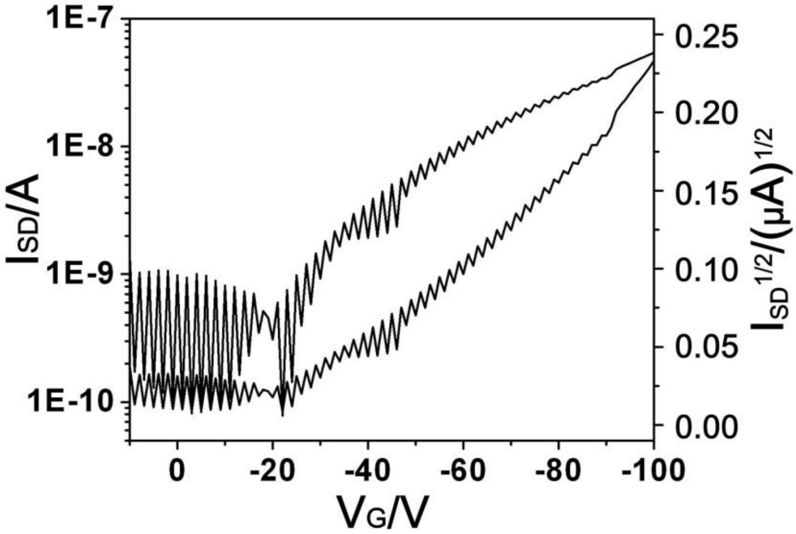

Figure 6.4. Transfer curve corresponding to the **6.1** films processed by dip coating at 200 µm/s.

Upon a further decrease of the pulling speed to 40 µm/s, the **6.1** monolayer almost completely covers the SiO_2 surface (Figure 6.2c). In comparison to Figure 2b, the nucleation centers of the subsequent microstructure further develop into long fibers which form a dense network with interconnections. As a result, the charge carrier mobility is one order of magnitude higher, 2.0×10^{-3} $cm^2V^{-1}s^{-1}$, with an on/off ratio of ~10^4 in comparison to the previous film. (Figure 6.5a, 6.5b) Additionally, the threshold voltage is reduced from -20 V to -12 V. The effect of contact resistance and problems with charge injection are clearly indicated by both the transfer and output curves. (Figure 6.5a, 6.5b)

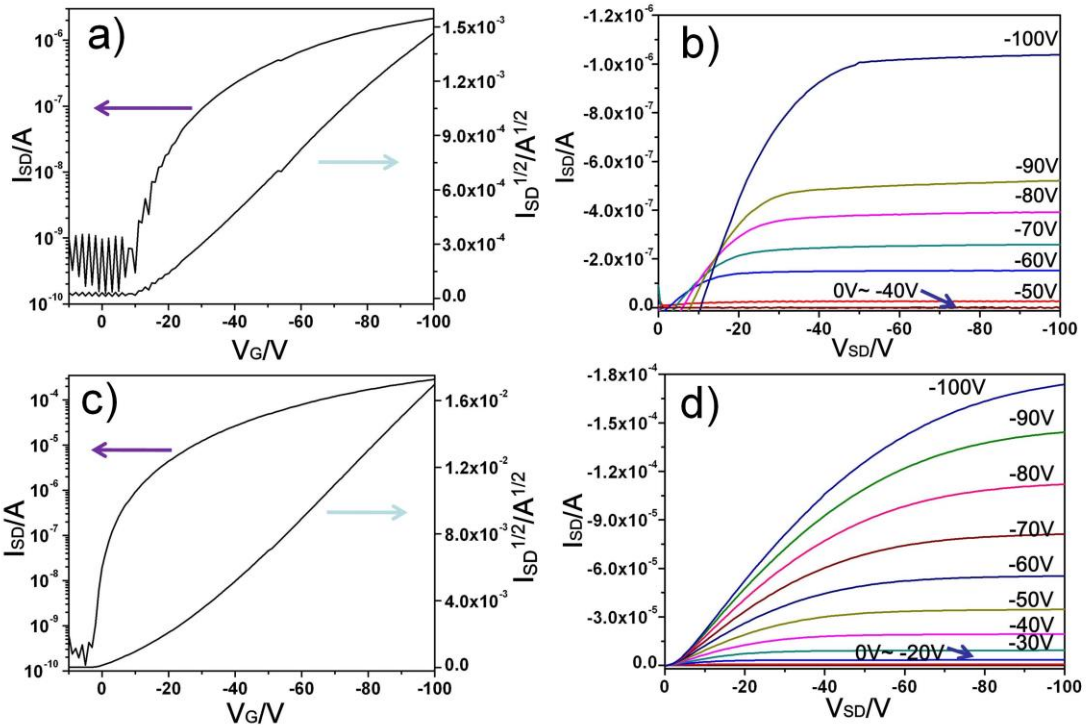

Figure 6.5. Transfer and output curves corresponding to the **6.1** films processed by dip coating at a) and b) 40 µm/s, c) and d) 10 µm/s.

When the speed of the substrate is further reduced to 10 µm/s a closed first layer and a continuous subsequent fibrous multilayer are obtained (Figure 6.2d). As shown in Figure 6.5c and 6.5d, a mobility of 0.36 $cm^2V^{-1}s^{-1}$ with on/off ratio of $1×10^6$ are determined. Moreover, the threshold voltage is again lowered from -12 V to -5 V. The significantly improved mobility and threshold voltage of this multilayer are attributed to the formation of a dense fibrous network layer. Such a network structure is ideal for OFET applications because the interconnected fibers enhance the charge carrier transport within the FET channel.

Finally, at the lowest speed of 2 µm/s long-range aligned, continuous polymer fibrous layers are obtained for films with a total thickness of ca. 15 nm over a macroscopic scale (Figure 6.6a and Figure 6.7). This pronounced orientation is induced by the low pulling speed and by the gradient which is established in the meniscus at the solvent-substrate interface. We have previously proven that under optimized dip coating conditions (e.g. slow pulling speed) conjugated donor-acceptor polymer chains are directed in the processing direction in which the maximum charge carrier mobility was recorded.[22] Previously, **6.1** was oriented via a flow-coating method.[23] In the case of dip-coating by 2 μm/s, the long-range aligned **6.1** films yield in high average mobility of 0.7±0.2 $cm^2V^{-1}s^{-1}$ with a highest mobility of 1.3 $cm^2V^{-1}s^{-1}$ and current on/off ratio of 5×10^6 measured parallel to the coating direction.

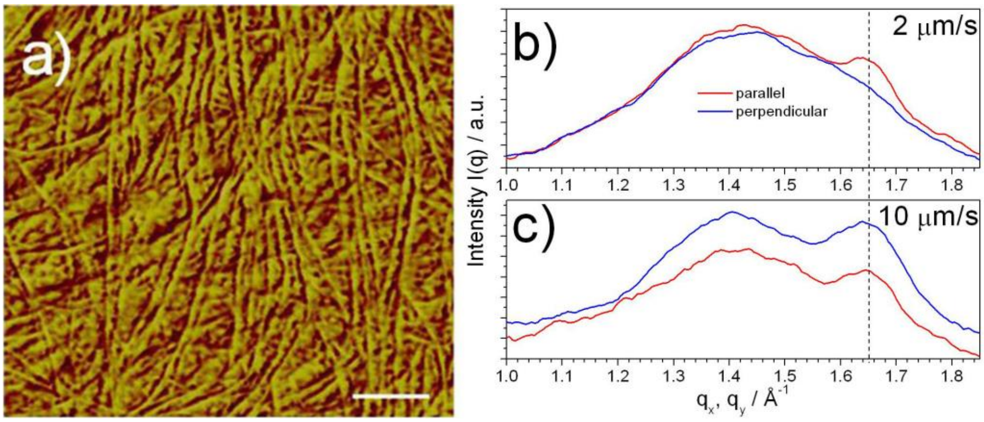

Figure 6.6. a) AFM image of the uniaxially oriented film dip-coated at 2 μm/s (the scale bar corresponds to 1 μm) and b) q_x/q_y integrations for the scattered intensities recorded perpendicularly (blue) and parallel (red) to dip direction. Films obtained at 2 μm/s and 10 μm/s. Dashed line indicates position of π-stacking reflections.

It has to be emphasized that this value is among the highest mobilities so far published for **6.1**-based OFETs. Remarkably enough, the dip coated films were simply deposited on untreated SiO_2 dielectric, which is known as a serious charge carrier trap.[24]

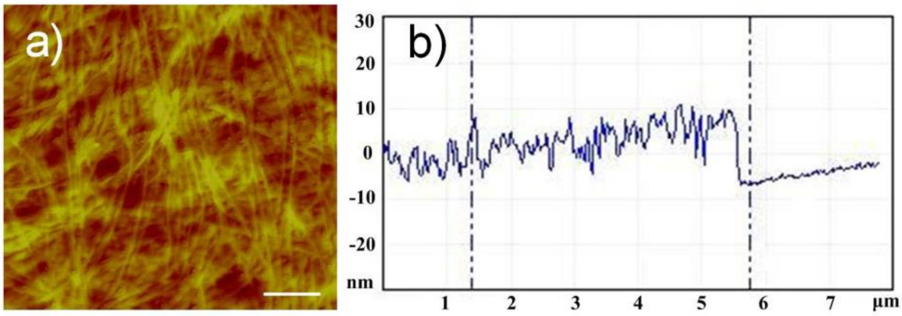

Figure 6.7. a) Tapping-mode AFM height image of **6.1** film and b) Height profile at a scratch in the film fabricated by dip coating at a speed of 2 μm/s.

Furthermore, the films were annealed far below the liquid crystalline phase transition above which typically the molecular packing improves significantly and leads for **6.1** to better device performance. However, in this case the film dewets at an annealing temperature of 180 °C. The conducting channel established by the interconnected fibrous structures is destroyed due to the low thickness forming a discontinuous network (Figure 6.8) and revealing much lower charge carrier mobility of 0.02 $cm^2V^{-1}s^{-1}$.

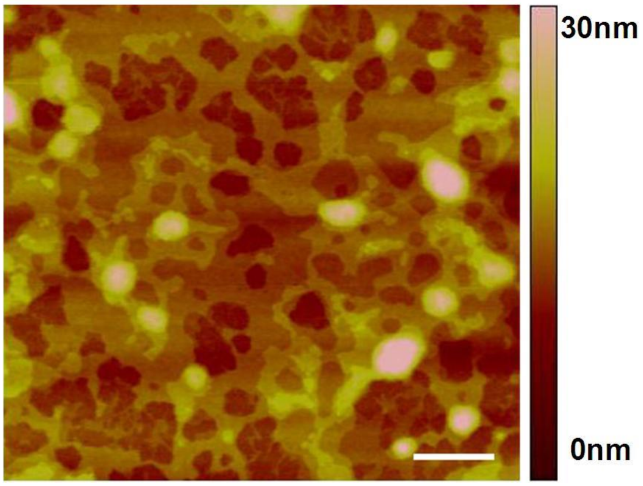

Figure 6.8. AFM image of the **6.1** film on SiO_2 surface fabricated by dip coating at a speed of 2 µm/s, after thermal annealing at 180 °C for 30 min. Scale bar corresponding to 500 nm.

Such a film topography of **6.1** after heating to the liquid crystalline phase is in agreement with literature [25, 26] (Figure 6.9). As shown in figure 6.9, the dewetting morphologies were obtained after heating above the mesophase transistion. The resulting device performance is also in the same range, around 0.02 $cm^2V^{-1}s^{-1}$.

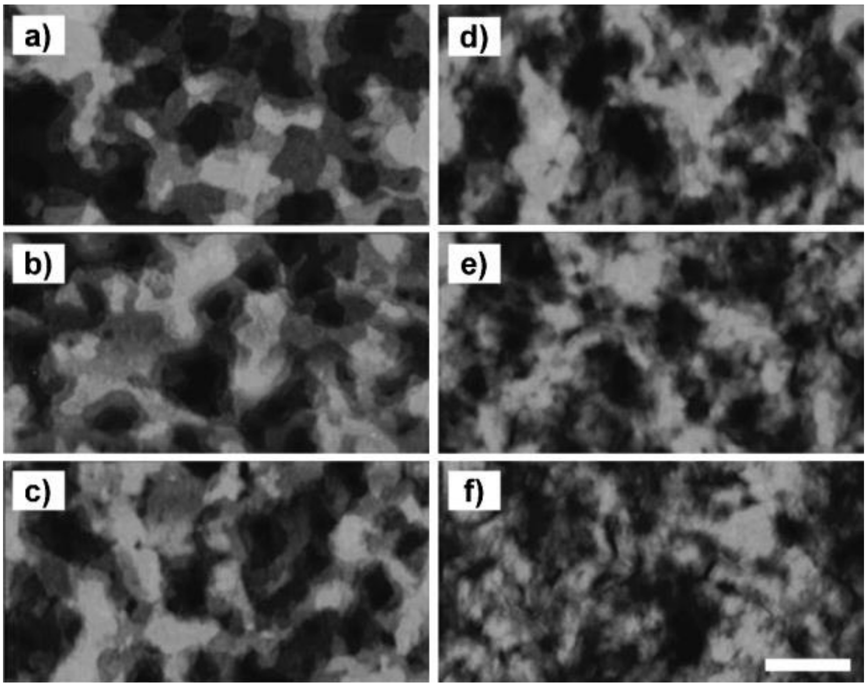

Figure 6.9. AFM images of the **6.1** film on SiO_2 surface after heating above the mesophase transistion. a) to f) films obtained on different substrates roughnesses. Scale bar corresponding to 400 nm. [26]

6.4 Structural analysis for fibrous layers

Another remarkable effect is the pronounced anisotropy of the electronic properties. The FET measurement perpendicular to the alignment direction gives charge carrier mobilities of only 6.2×10^{-2} $cm^2V^{-1}s^{-1}$. This is a significantly larger anisotropy ratio of ca. 20 in comparison to our previous work with only 2 for a donor-acceptor polymer. [22] To prove the structural isotropy for the layers processed by 10 µm/s or faster in comparison to the anisotropy obtained by dip-coating at 2 µm/s, the films were studied by grazing incidence wide-angle X-ray scattering (GIWAXS). All patterns reveal reflections on the q_z line of identical positions characteristic for a chain-to-chain distance of 2.2 nm of edge-on arranged **6.1** polymer chains (Figure 6.10).

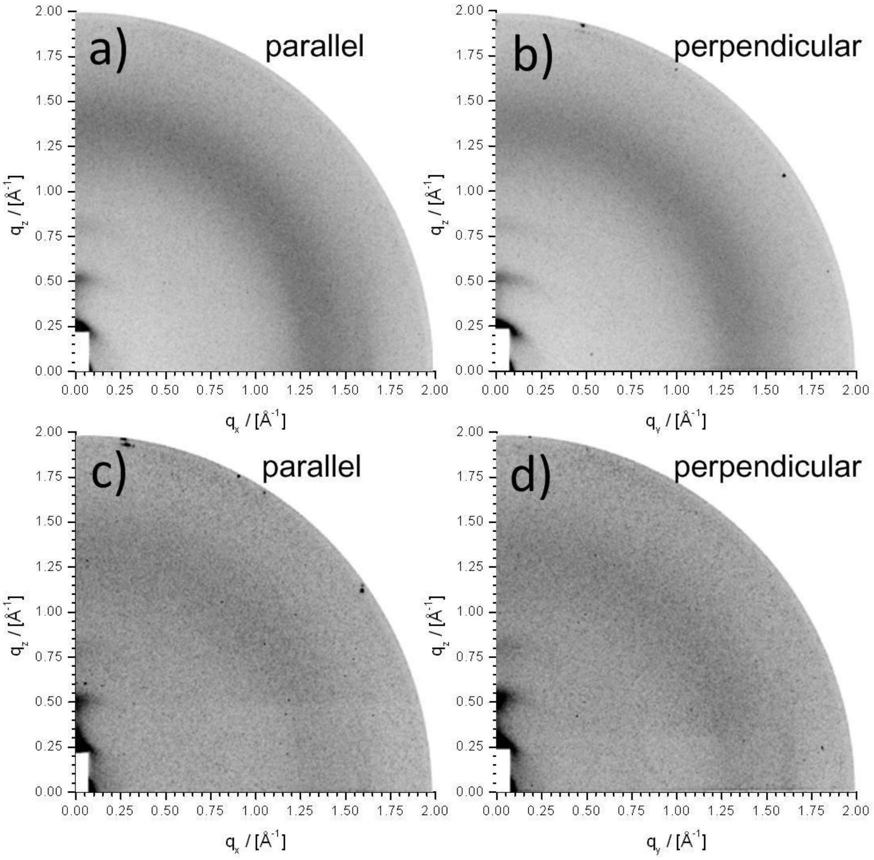

Figure 6.10. GIWAXS for films dip-coated at a), b) 2 µm/s and c), d) 10 µm/s measured parallel and perpendicular to the dip-coating direction.

However, differences are obvious for the reflections attributed to the π-stacking of 0.38 nm which are located on the q_y line. Due to the uniaxial orientation of the conjugated polymers along the drawing direction of the substrate at the processing speed of 2 µm/s, the scattering intensity is significantly higher for the measurement parallel to the dip-coating direction, while it disappears when the sample is investigated perpendicular (Figure 6.6b). In contrast to this, the intensity of the π-stacking reflection for the film processed at 10 µm/s does not change for both directions (Figure 6.6c) confirming structural isotropy. This isotropy is in good agreement with the microstructure in the AFM image in Figure 2d. Previously, PBTTT was heated to the liquid crystalline state and the domain sizes became larger than those prior to heating treatment, thus resulting in greatly improved charge carrier mobility. [4] Obviously, the higher mobility came from the larger grain sizes thus better connectivity of the crystalline domains. Hereby, heating the PBTTT to the liquid crystalline state is similar to a self-healing effect. In other words, small defects within the film (here we mainly consider the grain boundaries) were reduced or even cured in this way. In our case, for the fibrous film processed at 10 μm/s, the first monolayer is continuous and the subsequent interconnected fibrous layers greatly enhance the charge carrier transport, yielding mobilities in the same range as in the heating treated devices. [4]

For the aligned film obtained by dip-coating at 2 μm/s, the fibrous structures are homogeneous and continuous over a long range. The anisotropy effect is in agreement with all the former studies which indicate the limiting factor for device performance is the hopping between the conjugated backbones, and higher mobilities were observed in the direction of the backbones. Here one question must be raised: Are there other factors contributing to such a high anisotropy ratio? Especially in the previous study, anisotropy ratio of only 2 is observed for the dip coated CDT-BTZ copolymer film. [22] Here one should keep in mind that such a conclusion is only valid when the density of grain boundaries is the same in both directions. However, apparently, this is not the case for the aligned film obtained by dip-coating at 2 μm/s. Here it is obvious that the film is continuous over a longer range in the aligned direction than it is in the perpendicular direction. This is simply because the diameter of the individual aligned fibers is much smaller than their lengths, thus causing much higher density of grain boundaries between fibers along the perpendicular direction. (Figure 6.6a). These grain boundaries act in the devices as trapping sites, thus additionally reducing the performance in the same direction. Therefore, it is reasonable to account this effect as another reason for the much lower charge carrier mobility along the perpendicular direction.

By contrast, the dip coated CDT-BTZ copolymer film consists of multiple fibers domains [22] (Figure 1.9 in chapter 1). The fibers are much shorter and grain boundaries are comparable in both parallel and perpendicular directions. Therefore, one can expect that the charge carriers are also severely trapped by the grain boundaries along the dip coating direction, which is also the backbone direction since the charge carriers will be inevitably blocked from one fiber to another. Indeed this assumption is true since in continous fibers over a long range there is less trapping effect. A direct proof of this conclusion can be found in chapter 5. The mobility for CDT-BTZ single fibers is 3 times higher than that in the dip coated film (both are along backbone direction). It is assumed that structural defects are significantly reduced within a single fiber, promoting charge carrier transport between the electrodes. Therefore, based on the above findings, the high anisotropy ratio results mainly from two reasons: 1) charge transport along the polymer backbone direction is faster than it is along the π-π stacking direction; 2) the grain boundaries are much smaller in the backbone direction than in the π-π stacking direction. The second factor plays a larger role in determing the anisotropy ratio.

The anisotropy effect mainly caused by grain boundaries was also observed from small conjugated molecules. The aligned N,N'-bis(n-octyl)- (1,7: 1,6)-dicyanoperylene- 3,4:9,10-bis(dicarboximide) (PDI8–CN_2) films obtained by solution shearing revealed a high anisotropy ratio, with carrier mobility approximately two orders of magnitude higher in the aligned direction than that in the perpendicular direction. [27] Since the exact single-crystal mobility anisotropy of PDI8–CN_2 was calculated to be smaller than 12 (much smaller than the aligned film anisotropy ratio), the authors excluded single-crystal anisotropy as the main contributor to the reported anisotropy owing to the orientation of the main crystallite population with respect to the probed transport directions. They claimed that grain boundaries are the dominant factors in the observed electrical anisotropy of aligned PDI8-CN_2 films.

Very recently, PBTTT film is successfully aligned via zone casting by means of directed solidification of the solution during deposition. [28] In this study maps of the rate of change of backbone angles indicate that the presence of high-angle domain boundaries may serve as deep trapping sites. The backbone orientation in aligned nanoribbon films shows that the backbone orientation is not necessarily parallel to the zone-casting direction, but always perpendicular to orientation of the ribbons, which can divert up to 45° from the zone casting direction. In their cases, little optical anisotropy is observed in the bulk of as-cast films, and the as-zone-cast morphology does not exhibit any apparent topological features, as determined by AFM which is shown in Figure 6.11a, similar to its isotropic counterpart. After annealing through the second phase transition, the characteristic aligned nanoribbons are formed and seen in the topography image in Figure 11b. Regardless of the broad domain boundaries being observed in AMF image, as is shown in Figure 6.11b, a high anisotropy ratio of ca. 10 is detected. Interestingly, the mobility perpendicular to the dip coating direction in our case is within the same range as that perpendicular to the zone casting direction. However, the mobility parallel to the dip coating direction shows a twofold increase compared to that parallel to the zone casting direction. This is attributed to higher density of grain boundary in the zone casting direction than in the dip coating direction, as indicated by the AFM images(Figure 6.11b and Figure 6.6a). In other words, the dip coating film is well ordered in a longer range than the zone casting film.

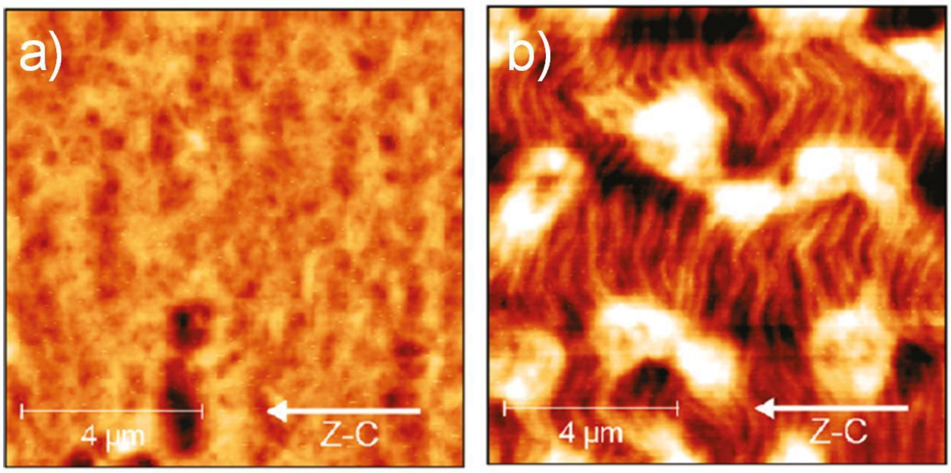

Figure 6.11. AFM image of PBTTT film on SiO_2 surface after heating above the mesophase transistion 180 °C for 30 min. Scale bar corresponding to 400 nm. [28]

The GIWAXS analysis allows to draw the following model for the organization in the various layers of the thin film which is presented schematically in Figure 6.12. The monolayer at the dielectric surface consists of edge-on arranged polymer chains as suggested from the AFM images (thin film deposited at 1 mm/s and 200 µm/s,). The thickness is in agreement with this structural analysis. On top of this first layer fibers are formed in which the edge-on polymer backbones are oriented along the fiber axis. This corresponds also to the fiber growth direction and the faster charge carrier migration. In these 4-6 nm thick fibers the polymer out-of-plane chain-to-chain spacing is 2.2 nm which is in an identical range to the monolayer thickness, as indicated in the illustration. This means that in the fiber 2-3 polymer chains are arranged on top of each other as illustrated in Figure 6.12 (corresponding to the thin film deposited at 10 µm/s).

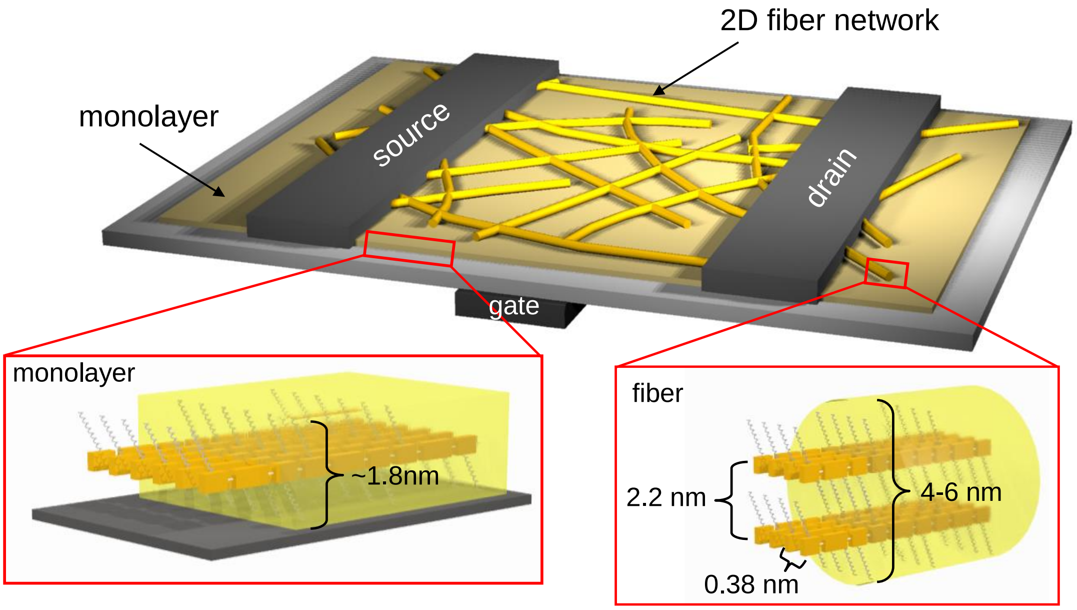

Figure 6.12. Schematic illustration for the molecular organization in the thin film deposited at 10 µm/s in an OFET.

Interestingly, when changing the solvent from chloroform to chlorobenzene with all other parameters unchanged, a quite similar microstructure was observed after dip coating. This is because the evaporation rate can be adapted in terms of the molecular interactions by choosing a proper solvent. In this case, chlorobenzene has a much higher boiling point than chloroform, which gives the **6.1** molecules more time to self-assemble into longer fibers before the solvent is fully evaporated. As shown in Figure 6.13, the first monolayer is covered with a film, while the subsequent fibers are much longer than the first layer. While the subsequent fibers have a lower density but are longer in comparison to Figure 6.2c.

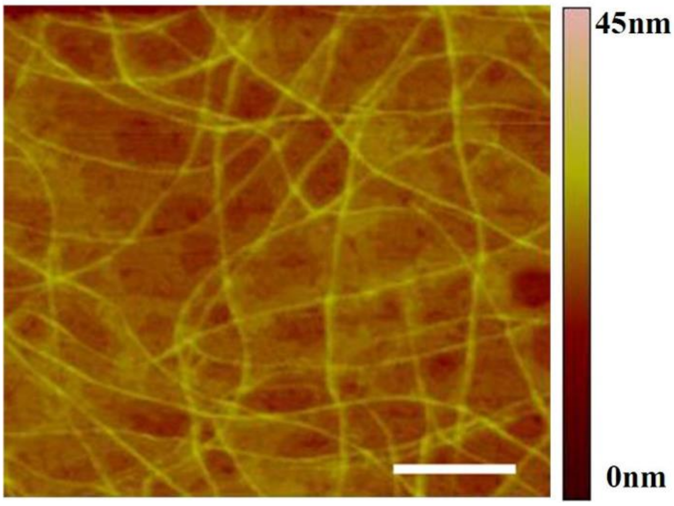

Figure 6.13. AFM image of the **6.1** film on SiO_2 surface prepared by dip coating from 0.5mg/ml chlorobenzene solution. Scale bar corresponds to 500nm.

6.5 Conclusion

In conclusion, a monolayer and its subsequent microstructure of a conjugated polymer on a rigid surface are precisely controlled by dip coating. These results point towards an essential role of the first polymer monolayer on the microstructure evolution in the bulk film during solution processing and on the charge carrier transport in the transistor. For a sufficient charge carrier transport a critical multilayer network is necessary to create the required percolation pathways. Hereby, the morphology difference between the first and the subsequent microstructure is obvious. The first monolayer greatly reduces the grain boundaries in comparison to the case when fibers are already formed in the first monolayer since the interconnection between fibers acts as charge trapping sites. This approach opens a new pathway for the bottom-up fabrication of conjugated polymer ultrathin films and provides new insights into the fundamental understanding of solution processable OFETs based on polymer thin films. Since the self-assembly of polymers strongly depends on the design of the backbone and the attached substituents, differences in the development of the film structure could be expected for other systems. The same question arises concerning the solution deposition technique with different processing parameters.

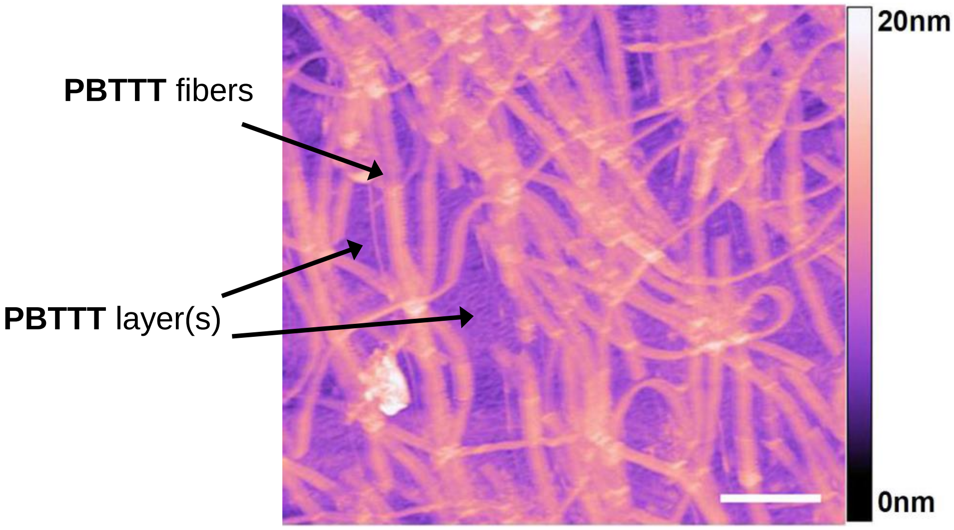

Figure 6.14. AFM image of the **6.1** film on SiO_2 surface prepared by spin coating at a speed of 3000rpm. Scale bar corresponds to 1µm.

The preliminary AFM images (Figure 6.14) for spin-coated films indicate an identical mechanism taking place during the microstructure evolution as for dip-coating. Long, thick fibers are formed on top of a layer of **6.1**. Unfortunately, spin-coating does not allow a defined control of the process conditions as it is the case during dip-coating. In this study, the start-of-art characterization of the microstructure evolution of PBTTT films, controlling alignment and their corresponding device performances provide a fundamental understanding of solution processable OFETs based on polymer thin films, and this method could be further exploited for a broad range of other conjugated polymers.

REFERENCES

[1] A. Dodabalapur, L. Torsi, H. Katz, *Science* **1995**, *268*, 270.

[2] H. Sirringhaus, P. J. Brown, R. H. Friend, M. M. Nielsen, K. Bechgaard, B. M. W. Langewvld-Voss, A. J. H. Spiering, R. A. J. Janssen, E. W. Meijer, P. Herwig, D. M. de Leeuw, *Nature* **1999**, *401*, 685.

[3] K. Xiao, Y.Q. Liu, X. B. Huang, Y. Xu, G. Yu, D. B. Zhu, *J. Phys. Chem. B* **2003**, *107,* 9226.

[4] J. Locklin, K. Shino, K. Onishi, F. Kaneko, Z. N. Bao, R. C. Advincula, *Chem. Mater.* **2003**,*15*, 1404.

[5] F. Dinelli, M. Murgia, P. Levy, M. Cavallini, F. Biscarini, D. M. de Leeuw, *Phys. Rev. Lett.* **2004**, *92*, 116802.

[6] A. Ruiz, A. Papadimitratos, A. C. Mayer, G. G. Malliaras, *Adv. Mater.* **2005**, *17*, 1795.

[7] J. Huang, J. Sun, H. E. Katz, *Adv. Mater.* **2008**, *20*, 2567.

[8] S. G. J. Mathijssen, E. C. P. Smits, P. A.v. Hal, H. J. Wondergem, S. A. Ponomarenko, A. Moser, R. Resel, P. A. Bobbert, M. Kemerink, R. A. J. Janssen, D. M. D. Leeuw, *Nature Nanotech.* **2009**, *4*, 674.

[9] L. Li, P. Gao, K. C. Schuermann, S. Ostendorp, W. Wang, C. Du, Y. Lei, H. Fuchs, L. D. Cola, K. Müllen, L. Chi, *J. Am. Chem. Soc.* **2010**, *132*, 8807.

[10] S. Fabiano, C. Musumeci, Z. Chen, A. Scandurra, H. Wang, Y. Loo, A. Facchetti, B. Pignataro, *Adv. Mater.*, **2012**, *24*, 951.

[11] C. Tanase, E. J. Meijer, P. W. M. Blom, D. M. d. Leeuw, *Org. Electron.* **2003**, *4*, 33.

[12] G, Xu. Z. Bao, J. T. Groves, *Langmuir* **2000**, *16*, 1834.

[13] H. G. O. Sanderg, G. L. Frey, M. N. Shkunov, H. Sirringhaus, R. H. Friend, M. M. Nielsen, C. Kumpf, *Langmuir* **2002**, *18*, 10176.

[14] J. C. Scott, J. D. J. Samuel, J. H. Hou, C. T. Rettner, R. D. Miller, *Nano Lett.* **2006**, *6*, 2916.

[15] B. Park, A. Aiyar, J. Hong, E. Reichmanis, *ACS Appl. Mater. Interfaces* **2011**, *3*, 1574.

[16] I. Mcculloch, M. Heeney, C. Bailey, K. Genevicius, I. Macdonald, M. Shkunov, D. Sparrowe, S. Tierney, R. Wagner, W. Zhang, M. L. Chabinyc, J. R. Kline, M. D. Mcgehee, M. F. Toney, *Nature Mater.* **2006**, *5*, 328.

[17] J. M. Mativetsky, M. Kastler, R. C. Savage, D. Gentilini, M. Palma, W. Pisula, K. Müllen, P.Samorì, *Adv. Funct. Mater.* **2009**, *19*, 2486;

[18] S. Wang, L. Dössel, A. Mavrinskiy, P. Gao, X. Feng, W. Pisula, K. Müllen, *Small*, **2011**,*7*, 2841.

[19]R. Ruiz, B. Nickel, N. Koch, L. C. Feldman, R. F. Haglund, A. Kahn, G. Scoles, *Phys. Rev. B* **2003**, *67*, 125406.

[20] F. Dinelli, M. Murgia, P. Levy, M. Cavallini, F. Biscarini, D. M. de Leeuw, *Phys. Rev. Lett.* **2004**, *92*, 116802.

[21] A. Ruiz, A. Papadimitratos, A. C. Mayer, G. G. Malliaras, *Adv. Mater.* **2005**, *17*, 1795.

[22]H. N. Tsao, D. Cho, J. W. Andreasen, A. Rouhanipour, D. W. Breiby, W. Pisula, K. Müllen, *Adv. Mater.* **2009**, *21*, 209.

[23]D. M. Delongchamp, R. J. Kline, Y. Jung, D. D. Germack, E. K. Lin, A. J. Moad, L. J. Tichter, M. F. Toney, M. Heeney, I. Mcculloch, *ACS Nano* **2009**, *3*, 780.

[24]S. C. Lim, S. H. Kim, J. H. Lee, M. K. Kim, D. J. Kim, T. Zyung, *Synthetic Metals* **2005**, *148*, 75.

[25] R. J. Kline, D. M. DeLongchamp, D. A. Fischer, E. K. Lin, M. Heeney, I. Mcculloch, M. F. Toney, *Appl. Phys. Lett.* **2007**, *90*, 062117.

[26] Y. Jung, R. J. Kline, D. A. Fischer, E. K. Lin, M. Heeney, I. Mcculloch, D. M. DeLongchamp, *Adv. Funct. Mater.* **2008**, *18*, 742.

[27] J. Rivnay, L. H. Jimison, J. E. Northrup, M. F. Toney, R. Noriega, S. Lu, T. J. Marks, A. Facchetti, A. Salleo, *Nat. Mater.*, **2009**, *8*, 952.

[28] T. Schuettfort, B. Watts, L. Thomsen, M. Lee, H. Sirringhaus, C. R. McNeill, *ACS. Nano.* **2012**, *6*, 1849.

Chapter 7.

Nanofiber Growth and Alignment in Solution Processed n-Type Naphthalene-Diimide-Based Polymeric Organic Field-Effect Transistors

7.1 Introduction

As indicated in chapter 5 and chapter 6, one-dimensional (1D) micro- and nanostructures of polymer, have attracted extensive attention due to their unique properties and promising applications in high performance organic electronics. As a result, research interest is being directed towards fabricating 1D micro- and nanostructures of polymer in OFETs and the study of their corresponding self-organization behavior. Nevertheless, not much attention has been paid to the processing methods which could allow to fabricate 1D objects over large areas in a well-controlled and straightforward fashion. Most importantly, questions concerning how the morphology, thickness and alignment influence the electronic properties remain not fully answered.

Herein, I depart from the conventional bulk polymeric film study and attempt to fabricate polymer nanofibers with a controllable growth via facile solution processing. n-Type organic semiconductors are indispensable for complementary circuits with high operation speed and low power consumption. Recently, achievements have been made in the synthesis of n-type polymers. [1-9] As model compound in the continuation of my former work in chapter 6, well-known n-type conjugated polymer poly{[*N* , *N* ′ -bis(2-octyldodecyl)-naphthalene-1,4,5,8- bis(dicarboximide)-2,6-diyl]-*alt*-5,5′-(2,2′-bithiophene)}, ((**P(NDI2OD-T2)**, Scheme 7.1, compound **7.1**) is chosen for this study, due to its high performance and remarkable stability, as well as its high tendency of self-assembly into fibers. [1-6] Top-gate bottom-contact transistors based on **P(NDI2OD-T2)** exhibit electron mobilities up to ~0.85 $cm^2V^{-1}s^{-1}$ under ambient conditions and under different relative humidities, [2] holding great promise for practical applications. The solubilities of **P(NDI2OD-T2)** in conventional organic solvents such as chloroform, xylene and dichlorobenzene are as high as 60 gL^{-1}. [2] Recently, **P(NDI2OD-T2)** showed an edge-on conformation order when processed by Langumuir-Schafer (LS) technique. [1] The LS allowed to fabricate highly reproducible monolayer OFETs which gave high electron mobility in a top-gate bottom-contact architecture. Hereby, the authors studied the relationship between transistor performances and the number of LS layers. It was observed that the mobility increased with the number of layers and saturates upon completion of the third layers with an average mobility of ~0.02 $cm^2V^{-1}s^{-1}$. Previously however, the same group demonstrated that this polymer showed a face-on predominantly orientation when processed via spin coating. [4, 7] Here the charge transport in the spin coated film was three-dimensionally driven and charge carriers moved along efficient transport pathways to subsequent layers coupled by the out-of-plane π-π stacking. Such a transporting mode enhanced electron mobility both in plane and out of plane. By contrast, the anisotropy of LS thin films limited the charge transport to the in-plane direction with the insulating long octyl-decyl side chains preventing charge hopping along the out-of-plane direction. [1] As a result, the transistors based on spin-coated films gave electron mobility up to one order of magnitude larger than those measured for LS/edge-on multilayers. [1] Very recently, instead of using GIWAXS, researchers performed a near-edge X-ray absorption fine-structure (NEXAFS) spectroscopy to observe the molecular orientation of spin-coated **P(NDI2OD-T2)** films. [8] Interestingly , by NEXAFS experiments a distinct edge-on preferential orientation of the conjugated backbones was detected at the surface of spin-coated with an average tilt angle of the backbone of α=36°from the surface normal. This is in contrast to the bulk face-on molecular orientation observed by GIWAX where α was approximately 50°.[8] The authors confirmed that the distinct edge-on orientation in spin coated **P(NDI2OD-T2)** films accounted for the high electron mobilities observed in top-gate transistors. Therefore, further consideration should be taken when using GIWAXS and NEXAFS separately to build the connection between molecular orientation and device performance. [8]

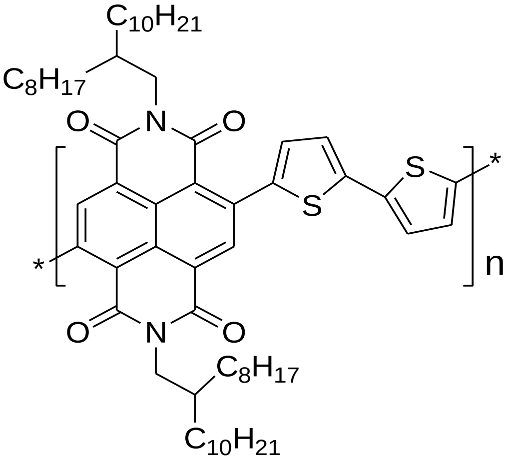

Scheme 7.1. Molecular structure of **P(NDI2OD-T2),** compound **7.1**.

This chapter focuses on the controllable nanofibrous growth of the polymer film during solution processing of **7.1**. The formation of the ultra-thin fibrous layer is precisely controlled via a facile dip-coating process, which is well known for microstructure alignment, [10-12] by tuning the pulling speed of the substrate from the solution reservoir. The influence of the dip coating speed on the microstructure evolution, especially in the early stages of polymer nanofibers formation, is studied by AFM. Hereby, the nanofibers obtained by dip coating at different pulling speed are highly reproducible. Furthermore, the effect on the charge carrier transport in OFETs is analyzed. Comparisons between dip coated films and LS multilayers are also made in this work.

7.2 Controllable growth of polymer monolayer

During the dip coating process, the pulling speed was gradually changed and had a great impact on the growth of compound **7.1**, mainly on film microstructure and the alignment of the nanofibrous structures. Hereby, dip coating is a powerful evaporation-controlled process and allows to establish a fine control of the evaporation rate of solvent at the contact line, substrate speed, and self-assembly propensity of the molecules. During processing, when the substrate is pulled out of the solution, a meniscus is formed at the substrate-solution interface. Below a critical substrate speed, a concentration gradient within this meniscus is established which acts as a driving force for the molecular alignment. Remarkably, monolayer and subsequent fibrous layers are formed for compound **7.1** over large areas by dip coating, as proven by atomic force microscopy (AFM) images (Figure 7.1).

Interestingly, a fibrous monolayer of compound **7.1** is formed on a SiO_2 surface (Figure 7.1a) when pulling the substrate at the highest speed of 2 mm/s, under which the substrate is fully pulled out of the solution within only 5 sec and still stays wet directly after this process. The AFM image displays a thickness of ca. 3.1 nm, and an average width of ca. 60 nm of the fibrous structures (Figure 7.1a). This microstructure is different from the former findings in chapter 6 on polymer (poly(2,5-bis(3-alkylthiophen-2-yl)thieno[3,2-b]thiophene), **PBTTT**, compound **6.1**. [13] In our recent study, a striking difference between the first monolayer and the subsequent microstructure was observed. The first monolayer shows a 2D microstructure, while the subsequent layers exhibited 1D fibers, which were considered to be the result of the different surface tension of **6.1** and SiO_2. In contrast to **6.1**, compound **7.1** does not reveal microstructure differences between different layers, which additionally verifies the hypothesis in our former study that the self-assembly of polymers from solution into the first few layers strongly depends on the design of the backbone and the attached substituents.

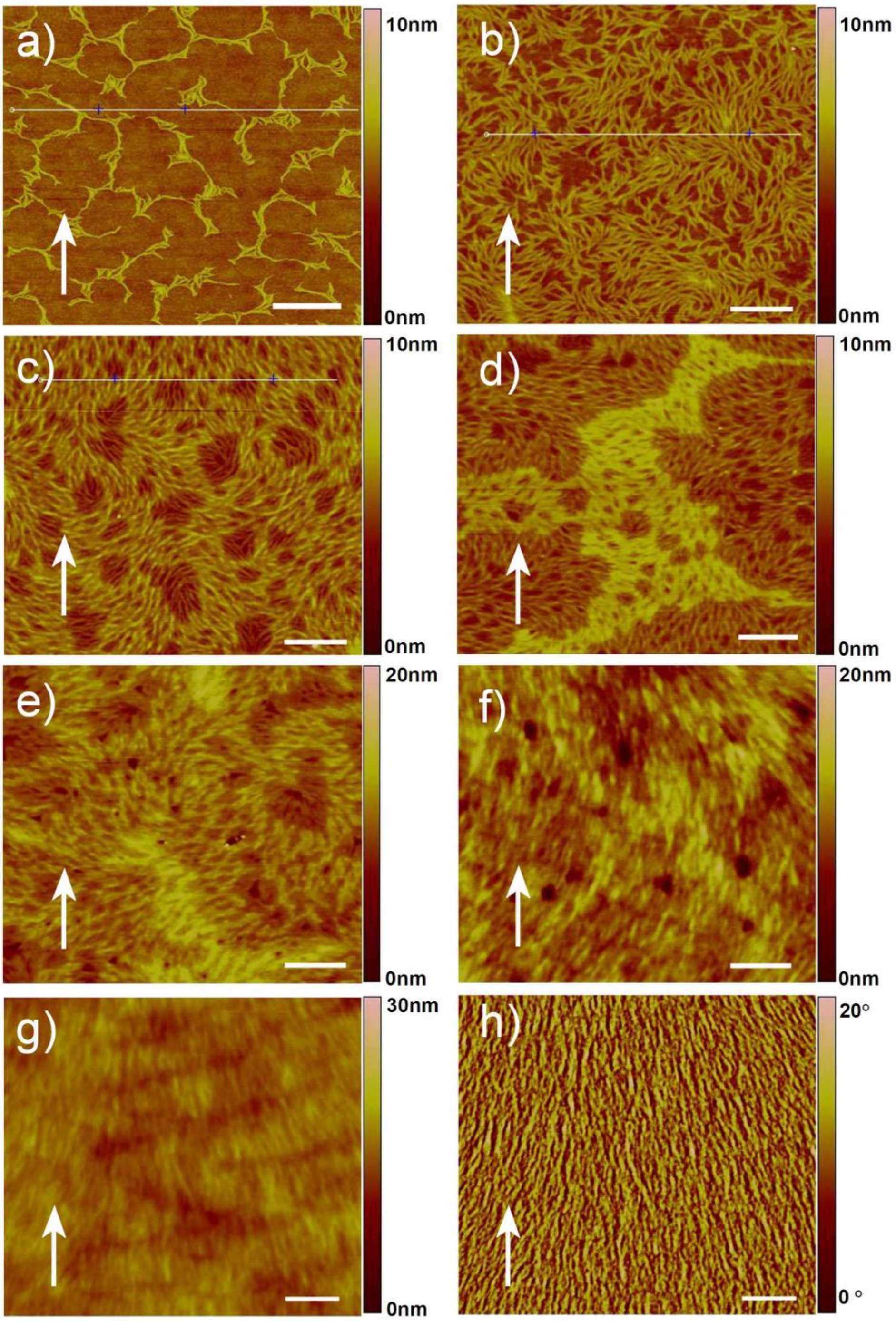

Figure 7.1. Tapping-mode AFM height images of compound **7.1** on SiO_2 surface obtained by dip coating under different pulling speeds: a) 2 mm/s, b) 200 µm/s, c) 40 µm/s, d) 30 µm/s, e) 20 µm/s, f) 10 µm/s, and g) 2 µm/s. h) phase image corresponding to figure g). The scale bar corresponds to 1 µm. White arrow indicates the dip coating direction.

Since the surface tensions are quite similar for both polymers, compound **7.1** and **PBTTT** (the contact angle is 99±1° for the former and 102±1° for the latter), the variation of the self-assembly behavior between compound **7.1** and **6.1** can be attributed only to their different backbone structure and substituents leading to a change in macromolecular interactions.[14] More precisely, in comparison to **6.1**, the bulky branched side chains of compound **7.1** lead to stronger hydrophobic interactions between the molecules, which is assumed to result in direct self-assembly of the molecules into well-defined 1D fibers in the first monolayer on top of the SiO_2 surface. It was previously reported that bulky side chains were favorable for solvophobically hydrophobic interactions thus leading to the lateral growth directly into fibers.[14] Moreover, in contrast to **6.1**, the fibrous microstructure of compound **7.1** is independent of the pulling speed and of the film thickness. In other words, the fibrous structure remains unchanged in each layer, from a not fully covered monolayer to multilayer. This allows one to directly compare OFETs of different thicknesses and to establish a relation between thickness and charge-carrier mobility.

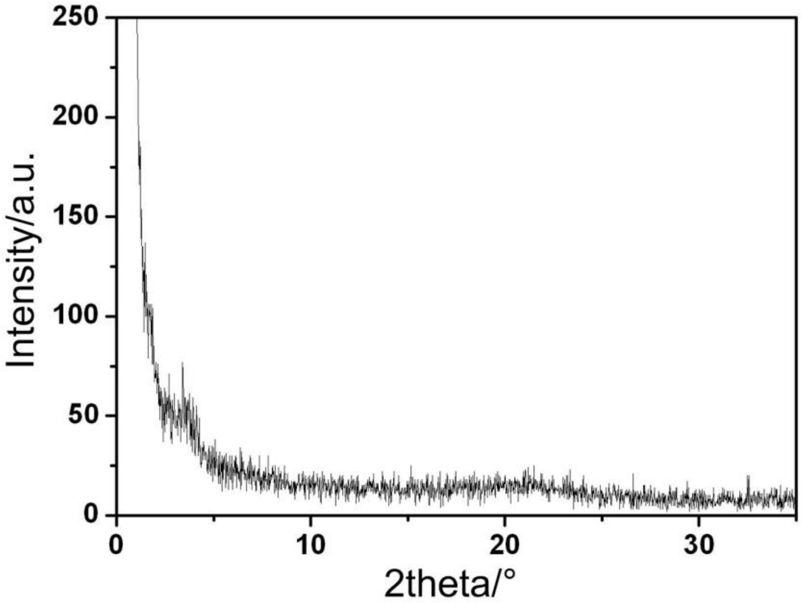

Figure 7.2. XRD of the compound **7.1** dip coated film corresponding to Figure 7.1f.

7.3 Thickness dependence from polymer monolayer to multilayers

Lowering the pulling speed to 200 µm/s leads to a larger area covered by the fibrous monolayer (Figure 7.1b). The thickness remains unchanged, while the average fiber width (~80 nm) slightly increases. The well-controlled growth of the polymer nanofibers provides an elegant platform for a systematic investigation of the charge carrier transport in the charge accumulation and transporting layer of an OFET. The OFET devices were fabricated in a top-contact bottom-gate (TGBC) configuration. Details of the device fabrication are described in the experimental section. Before the OFET measurements, the thin films were thermally annealed at 150 °C for 30 min to remove residual solvent. It is important to emphasize that the microstructure before and after annealing remains unchanged, which is in agreement with the literature. [1] Previously it was observed that thermal annealing at 150 °C for overnight had no distinguishable effects on the morphology of **P(NDI2OD-T2)** films processed by LS technique. [1] Even though the fiber nuclei become longer in Figure 1b, they are still not fully interconnected. Therefore, almost no field-effect response ($<10^{-6}$ $cm^2V^{-1}s^{-1}$) is detected for these layers (Figure 1a and 1b). At a further decrease of the pulling speed to 40 µm/s, the compound **7.1** monolayer completely covers the SiO_2 surface (Figure 7.1c). In comparison to Figure 1b, the fiber nuclei become long enough to form a continuous fibrous monolayer. Deeper insight into the macromolecular organization is obtained from XRD in reflection mode. Interestingly, although high molecular order is expected from the fibrous microstructure in Figure 1,[4] only one weak scattering peak corresponding to a chain-to-chain distance of 2.55 nm appears indicating low order of possibly edge-on arranged backbones (Figure 7.2). As a result, low mobility of 6×10^{-4} $cm^2V^{-1}s^{-1}$ and high threshold voltage are observed for the layer processed by 40 µm/s (Figure 7.3a). The on/off ratio is ranged between 10^3 and 10^4. As shown in Figure 1c, we assume the boundaries between fibers might act as structural trapping sites leading to lower mobilities and low on/off ratio. This is also verified by the ill-defined output curve shown in Figure 7.4a. Even though the performance is low under these device conditions, we define this mobility as an on-set value for compound **7.1** in a working transistor. In other words, the minimum thickness acting as the channel of an OFET is just one monolayer. [1] A former study also showed that one monolayer of LS processed **P(NDI2OD-T2)** was the minimum thickness to give field effect. [1]

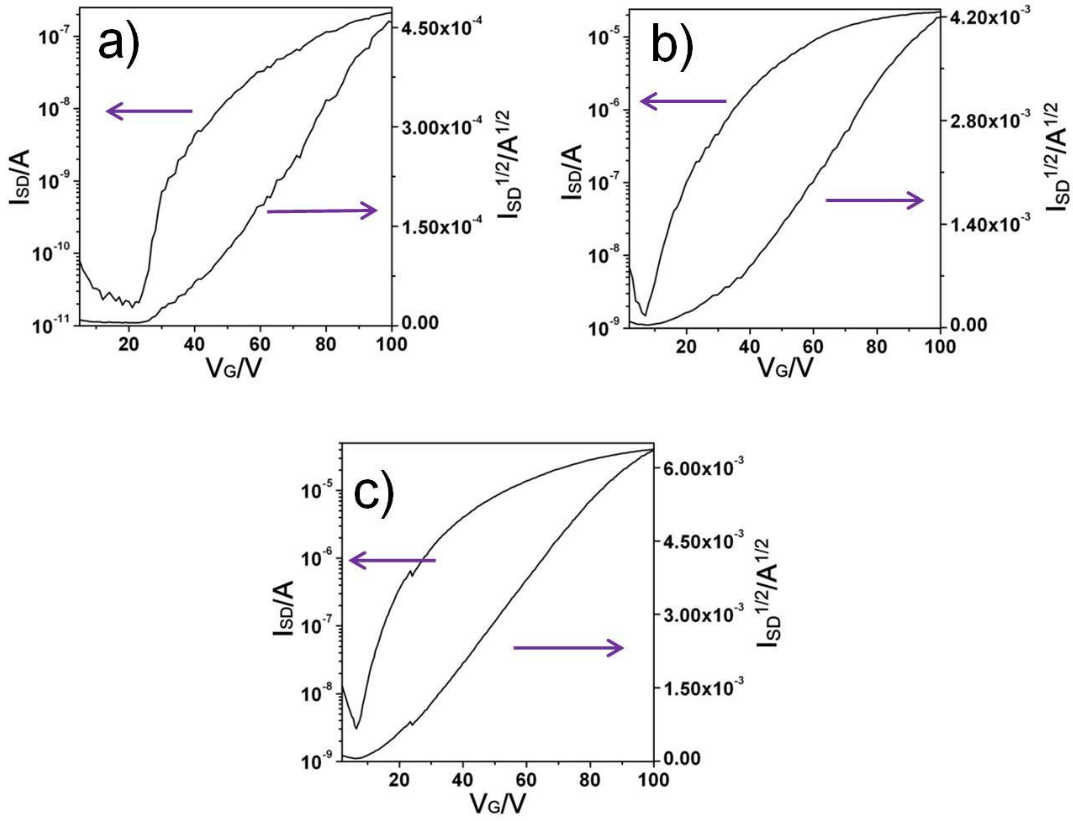

Figure 7.3. Transfer curves corresponding to compound **7.1** films processed by dip coating at a) 40µm/s, b) 10 µm/s, and c) 2 µm/s.

The well-controlled growth of the polymer nanofibers was further investigated by tuning the pulling speed which appeared to have a great influence on the fiber growth of **7.1**, mainly on the fibrous film thickness. This allows establishing the connection between the film thickness and the device performance. Figure 7.5a describes the relationship between the polymer fibrous film thickness (number of molecular layers) and the pulling speed (U), whereby the thickness decreases with increasing substrate speed. At a pulling speed higher than 60 µm/s only a not fully covered fibrous layer is formed, while below 30 µm/s, two and more molecular layers are obtained. Interestingly, a speed below 10 µm/s induces additionally alignment of the polymer chain in the film. As a result, greatly improved charge carrier mobility of 0.025 $cm^2V^{-1}s^{-1}$ is observed for the layer processed at 10 µm/s (Figure 7.3b). The on/off ratio is between 10^4 and 10^5.

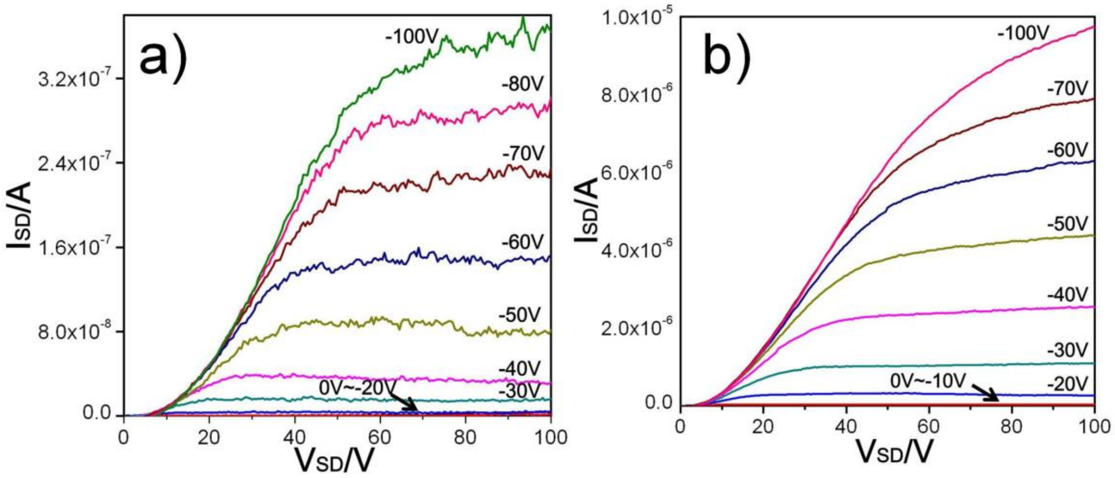

Figure 7.4. Output curves corresponding to compound **7.1** films processed by dip coating at a) 40µm/s, b) 10 µm/s.

Correspondingly, Figure 7.5b shows the evolution of the field-effect mobility as a function of the fibrous film thicknesses. The mobility increases with the increasing thickness until an almost saturation at a thickness of 6 molecular layers. At 4 molecular layers, from which the polymer starts to align along the dip coating direction, the mobility rises particularly sharply. Although just the first fibrous layer is sufficient for a working OFET, the improvement of the mobility from 1 fibrous layer to 3 layers indicates that in addition to the first fibrous layer, the subsequent several fibrous layers provide alternative pathways for the charge transport. Recent studies showed the same tendency that the charge carrier mobilities were greatly improved for the OFETs based on 2~3 layers, compared to those based on monolayers. [1, 13]

As the charge carrier transport mainly occurs in few molecular layers near the dielectric surface, the charge carrier mobility usually comes to saturation after the closing of these few layers. For instance, it was observed that the mobility saturated upon completion of the bottom three monolayers of LS film. [1] Therefore it could be expected that the slope of mobility will become smaller with the increasing thickness. However, in comparison to the increase of mobility from two to three layers, the value jumps significantly strongly from 3 layers to 4 layers mainly due to the combined effect of increased thickness and the fiber alignment. In addition, the threshold voltage decreases from 35 V for the monolayer to 18 V for eight layers (Figure 7.5c). This again verifies that the subsequent 3~4 layers could provide alternative pathways for charge transport, in this way reducing the threshold voltage.

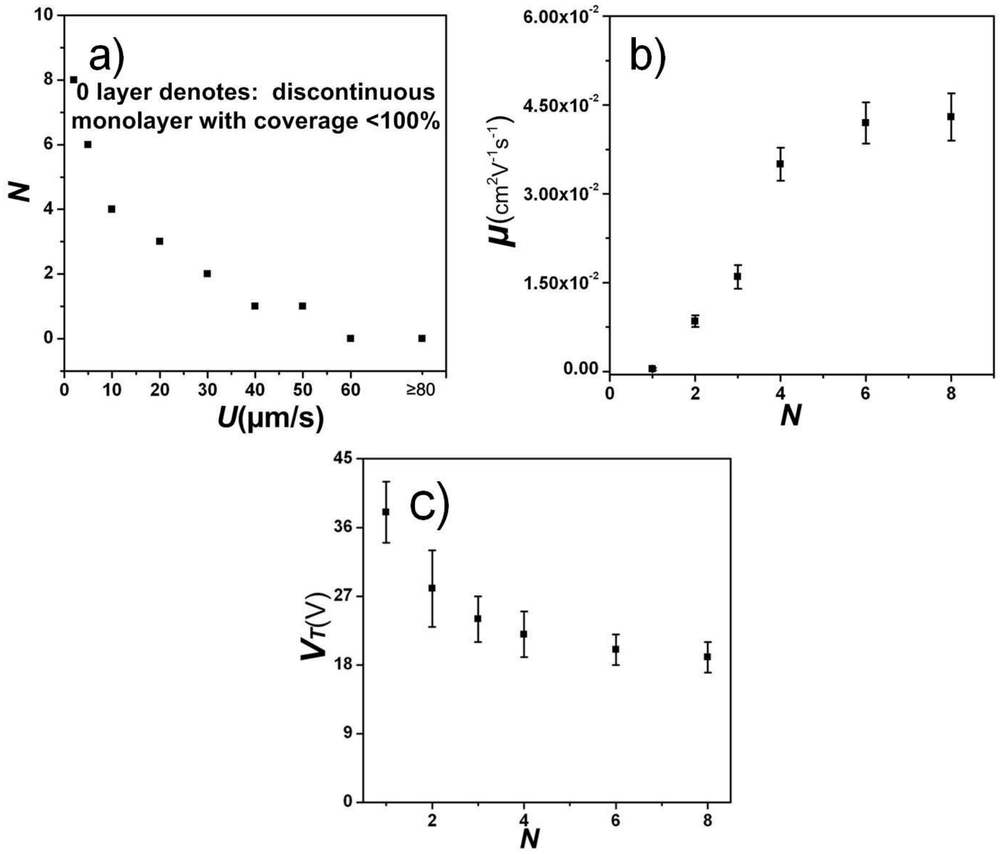

Figure 7.5. a) Evolution of fibrous film thicknesses (the number of compound **7.1** molecular layers)(N) with pulling speed (U), b) relation between the number of molecular layers (N) to b) charge carrier mobility (μ) and c) threshold voltage (V_T).

At the lowest pulling speed of 2 µm/s long-range aligned, fibrous layers are obtained over a macroscopic scale with a total film thickness of ca. 25 nm (Figures 7.1f and 7.1h), yielding in average mobility of 0.043±0.004 $cm^2V^{-1}s^{-1}$ along the dip coating direction with a highest mobility of 0.06 $cm^2V^{-1}s^{-1}$ (Figure 7.3c). Although this performance is one order of magnitude lower in comparison to top-gate devices, it is close to the best mobility reported for bottom contact, bottom gate transistors (~0.1 $cm^2V^{-1}s^{-1}$). [15] One should keep in mind that in the above mentioned work, OTS was used to modify the SiO_2 surface. However, in this work, the films were directly dip coated on plasma treated SiO_2 surface because OTS treatment is detrimental to the layer formation due to the hydrophobic surface repelling the organic solvents. It was reported that SiO_2 contained polar silanol groups especially trapping electrons within the organic semiconductor.[16] The pronounced polymer fibers orientation is induced by the low pulling speed and by the gradient which is established in the meniscus at the solvent-substrate interface. Under optimized dip coating conditions (e.g. slow pulling speed), the fibers were directed in the dip coating direction which yielded consequently the improved charge carrier mobility due to enhanced charge carrier transport along the conjugated backbones.

A previous study showed that the aligned films were highly anisotropic. [4] The in-plane polymer ordering was unprecedented for semiconducting polymer thin films, especially due to the inherent disorder and fluctuations often found in the crystalline phases of these materials. [4] However, in our study, due to the low order already observed for higher dip coating speeds, GIWAXS reveals no in-plane π-stacking reflection which could allow to determine the polymer orientation in the film and thus in the fibers. This result is in agreement with recent findings which revealed in addition to the edge-on structure, other potential packing motifs of different polymers can lead to high charge-carrier mobility. [17] For instance, it is reported that poly(3,4-dialkylterthiophenes) (P34ATs) have comparable transistor mobilities (0.17

$cm^2V^{-1}s^{-1}$) and greater environmental stability (less degradation of on/off ratio) than regioregular poly(3-alkylthiophenes) (P3ATs). Though, P34ATs do not show a strong and distinct π-π stacking in X-ray diffraction. [17]

It has to be noted that LS processed monolayers give a sufficient field-effect response with pronounced mobility already for one monolayer.[1] On the other hand, the processing conditions and the resulting microstructure of the layers differ significantly between LS and dip-coating. In the first fabrication method, the solution is deposited on a water surface on which the self-assembly occurs followed by subsequent compressing into a homogenous and continuous film. Afterwards, this monolayer is transferred onto a solid substrate. This procedure can be repeated to reach a multilayer film arrangement. During dip coating the polymer self-assembles and forms the corresponding microstructure including distinct domains and grain boundaries directly on the surface, while the film thickness is controlled by the drawing velocity of the substrate. The microstructure, which is not well pronounced in LS films, significantly influences the charge carrier transport. In the dip coated layers, the boundaries between fibers might act as structural trapping sites leading to lower mobilities in comparison to LS layers. Moreover, in contrast to the LS technique, which leads to a homogenous film, it is assumed that during the directional substrate movement via dip coating, nucleation centers are created at the contact line between the solvent and the surface. An identical contact line can be formed in an evaporating droplet deposited by e.g. drop-casting or inkjet printing. [18-21] This prevents 2D structure formation thus yielding anisotropic fibers on a macroscopic scale. For instance, contact line was formed via drop casting of a soluble acenes 6,13,-triisopropylsilylethynyl pentacene (TIPS_PEN) on the surface, resulting in single crystals. [18] Inkjet printing of 2,7-dioctyl[1]benzothieno[3,2-b][1]benzothiophene(C8-BTBT) resulted in single crystals, yielding average carrier mobilities as high as 16.4 $cm^2V^{-1}s^{-1}$. [21]

7.4 Conclusions

In conclusion, nanofibers of compound **7.1** as an n-type conjugated polymer have been successfully grown by facile solution-based dip coating. The growth of nanofibers is precisely tunable simply by controlling the pulling speed of the dip coating process. The corresponding OFET study indicates a morphology, thickness and alignment dependence of the device performance. The fibrous structure remains unchanged from fast pulling speed (a not fully covered monolayer) to low pulling speed (multilayer). This finding suggests that the self-assembly of polymers into the first few layers strongly depends on the molecular interactions. The first fully covered monolayer is the minimum thickness for a charge carrier migration in a film with a fibrous microstructure. The subsequent 3~4 fibrous layers could provide alternative pathways for charge transport. Our approach provides new insights into the fundamental understanding of solution processable OFETs based on polymer fibrous thin films. Very recently, researcher successfully fabricated **P(NDI2OD-T2)** fibers by means of electronspinning with blending poly(ethyleneoxide) (PEO) as supporting polymer. [22] This is the first report for n-channel polymeric fiber-based OFETs. Such devices showed electron mobilities as high as 0.05-0.09 $cm^2V^{-1}s^{-1}$. These single fibers were also deposited directly on bare SiO_2 without OTS modification. Such a device performance is comparable to that obtained from our dip coating aligned fibrous films. Remarkably, researchers observed that the mobility was unchanged both before and after PEO removal, both with and without OTS treatment. [22] As a disadvantage of this technique, conjugated polymers are characterized by a more rigid backbone in comparison to traditional polymers, which could limit the number of entanglements that assist the fibers formation during electrospinning. Therefore, it is necessary to blend a second polymer, which supports the fiber formation. [22, 23] However, the supporting polymer is likely to negatively affect the charge transport in the fibers, although the above mentioned researchers were lucky in this aspect. This is also the reason why such work is so far rarely reported. In comparison, our method does not require the addition of a second polymer therefore it can be further exploited for a broad range of other high performance conjugated polymers. Especially in light of inducing well aligned fibrous films with good alignment over long range, our results represent a useful strategy for both fundamental studies and practical device applications.

REFERENCES

[1] S. Fabiano, C. Musumeci, Z. Chen, A. Scandurra, H. Wang, Y. Loo, A. Facchetti, B. Pignataro, *Adv. Mater.*, **2012**, *24*, 951.

[2] H. Yan, Z. Chen, Y. Zheng, C. Newman, J. R. Quinn, F. Dötz, M. Kastler and A. Facchetti, *Nature*, **2009**, *457*, 679.

[3] R. Steyrleuthner, M. Schubert, F. Jaiser, J. C. Blakesley, Z. Chen, A. Facchetti and D. Neher, *Adv. Mater.*, **2010**, *22*, 2799.

[4]J. Rivnay, M. F. Toney, Y. Zheng, I. V. Kauvar, Z. Chen, V. Wagner, A. Facchetti and A. Salleo, *Adv. Mater.*, **2010**, *22*, 4359.

[5] M. Caironi, M. Bird, D. Fazzi, Z. Chen, R. Di Pietro, C. Newman, A. Facchetti and H. Sirringhaus, *Adv. Funct. Mater.*, **2011**, *21*, 3371.

[6] Z. Chen, Y. Zheng, H. Yan and A. Facchetti, *J. Am. Chem. Soc.* **2009**, *131*, 8.

[7] R. Steyrleuthner, T. Schubert, I. Howard, B. Klaumunzer, K. Schilling, Z. H. Chen, P. Saalfrank, F. Laquai, A. Facchetti, D. Neher, *J. Am. Chem. Soc.* **2012**, *134*, 18303.

[8] T. Schuettfort, L. Thomsen, C. R. McNeill, *J. Am. Chem. Soc.* **2013**, *135*, 1092.

[9]Y. Qiao, Y. Guo, C. Yu, F. Zhang, W. Xu, Y. Liu and D. Zhu, *J. Am. Chem. Soc.* **2012**, *134*, 4084.

[10] N. L. Liu, Y. Zhou, L. Wang, J. B. Peng, J. Wang, J. Pei and Y. Cao, *Langmuir* **2009**, *25*, 665.

[11] S. H. Wang, M. Kivala, I. Lieberwirth, K. Kirchhoff, X. Feng, W. Pisula and K. Müllen, *ChemPhysChem*, **2011**, *12*, 1648.

[12] J. Jang, S. Nam, K. Im, J. Hur, S. N. Cha, J. Kim, H. B. Son, H. Suh, M. A. Loth, J. E. Anthony, J. Park, C. E. Park, J. M. Kim, K. Kim, *Adv.Funct. Mater.*, **2012**, *22*, 1005.

[13] S. Wang, A. Kiersnowski, W. Pisula, K. Müllen, *J. Am. Chem. Soc.* **2012**, *134*, 4015.

[14] K. Balakrishnan, A. Datar, W. Zhang, X. Yang, T. Naddo, J. Huang, J. Zuo, M. Yen, J. S. Moore, L. Zang, *J. Am. Chem. Soc.* **2006**, *128*, 6576.

[15] J. C. Scott, J. D. J. Samuel, J. H. Hou, C. T. Rettner, R. D. Miller, *Nano Lett.* **2006**, *6*, 2916.

[16]L. L. Chua, J. Zaumseil, J. -F. Chang, E. C. -W. Ou, P. K. -H. Ho, H. Sirringhaus, R. H. Friend *Nature*, **2005**, *434*, 194.

[17] S. Ko, E. Verploegen, S. Hong, R. Mondal, E. T. Hoke, M. F. Toney, M. D. McGehee, Z. Bao, *J. Am. Chem. Soc.* **2011**, *133*, 16722.

[18] J. A. Lim, H. S. Lee, W. H. Lee, K. Cho, *Adv.Funct. Mater.*, **2009**, *19*, 1515.

[19] E. Tekin, E. Holder, D. Kozodaev, U. S. Schubert, *Adv. Funct. Mater*. **2007**, *17*, 277.

[20] R. van Hameren, P. Schön, A. M. van Buul, J. Hoogboom, S. V. Lazarenko, J. W. Gerritsen, H. Engelkamp, P. C. M. Christianen, H. A. Heus, J. C. Maan, T. Rasing, S. Speller, A. E. Rowan, J. A. A. W. Elemans, R. J. M. Nolte, *Science*, **2006**, *314*, 1433.

[21] J. A. Lim, W. H. Lee, H. S. Lee, J. H. Lee, Y. D. Park, K. Cho, *Adv. Funct. Mater*. **2008**, *18*, 229.

[22] E. V. Canesi, A. Luzio, B. Saglio, A. Bianco, M. Caironi, C. Bertarelli, *ACS Marco Lett.* **2012**, *1*, 366.

[23] V. Vohra, G. Galzaferri, S. Destri, M. Pasini, W. Porzio, C. Botta, *ACS Nano.* **2010**, *4*, 1409.

Chapter 8.

Influence of Surface Roughness on the Microstructure Evolution and Device Performance of PDI8-CN$_2$ from Monolayer to Bi/tri Layers

8.1 Introduction

As demonstrated in chapter 6 and chapter 7, the main charge carrier transport in transistors (the so-called conducting channel) occurs in few molecular layers near the dielectric surface. As a result, ultra-thin film organic transistors with few semiconducting monolayers are particularly appealing, because charge carriers are directly transported to conduction channels, which allow establishing connections between ultrathin film microsturcture and device performance. [1-3] Besides, due to minimum materials consumption, ultra-thin films also hold great promise for the field of miniaturized organic and supramolecular electronics.

Fabrication of semiconductor monolayers is highly desirable. Particularly, arranging the semiconductor molecules of the first monolayer into high order would greatly enhance the device performance. However, up to now, most work is performed to improve the molecular order of bulk films. Research on improving the molecular order of the first monolayer is still rarely reported since downscaling thin films into monolayers is still challenging. For vacuum sublimation, modifying the dielectric surface by silanes usually leads to better molecular order in the ultra-thin films, resulting in improved charge carrier mobility. [4-6] However, the role of silane treatment is still not fully revealed. For instance, it is observed that pentacene devices with OTS-modified dielectric layers exhibit much worse device stability than those with bare SiO_2 since the OTS-modified SiO_2 dielectric layer favors pentacene aggregation. [7] No obvious aggregation was observed for devices with bare SiO_2. Therefore, hydrophobicity alone cannot explain the improvement of the device performance. The same question arises for solution-processed ultra thin films for which silane treatment is usually detrimental to the layer formation. The hydrophobic surface repels the organic solvents, usually resulting in no film formation. This is especially true for dip coating and zone casting, which are well recognized as effective ways to align thin films. Therefore, SiO_2 without silane treatment is typically employed for both methods. Hereby, surface roughness becomes the essential factor in determing the microstructure evolution and their corresponding performance.

Up to now, there are only few reports on the effect of surface roughness on the film growth during vacuum deposition. For instance, a dramatic reduction in pentacene grain size was observed with increasing dielectric surface roughness from 0.16 to 0.22nm, which decreased the charge carrier mobility from 0.17 to 0.0075 $cm^2V^{-1}s^{-1}$. [8] It was observed that the Vt shift remained not greatly influenced by variation of pentacene grain sizes. The significant decrease in mobility was also much larger than that due to the grain size effect. This suggested that 2 factors contributed to the decrease of mobility: 1. the increase in the grain boundary; 2. the increase in the lattice distortion of pentacene due to the larger roughness of the SiO_2 surface.

Nevertheless, the effect of surface roughness on solution-processed ultrathin layers are still poorly understood, especially no study has been performed to monitor the microstructure evolution from monolayer to few layers. In contrast to vacuum deposition during which the thickness is precisely controlled, downscaling the semiconductor films to a monolayer and few layers by solution processing is a challenging task. Therefore, the effect of surface roughness on the microstructure evolution from monolayer to multilayer via solution processing and the corresponding device performance are so far not reported, but is an essential issue allowing a fundamental understanding, deserving particular attention.

This chapter focuses on probing the effects of surface roughness in the microstructure evolution from monolayer to bi/tri layers via solution processing. As model compound, well-known high performance n-type **PDI8-CN$_2$** (Scheme 8.1, compound **8.1**) has been used. **8.1** holds great promise for practical applications because of the unique combination of high-yield and scalable synthesis, chemical stability, satisfying field-effect mobility, and solution processibility.[9-10] Previously researchers reported that aligned PDI8–CN$_2$ films obtained by solution shearing revealed high anisotropy ratio, with carrier mobility approximately two orders of magnitude higher in the aligned direction than that in the perpendicular direction. [11] It was observed that instead of single-crystal anisotropy, grain boundaries were the dominant factors in the observed electrical anisotropy of aligned PDI8-CN$_2$ films. The authors demonstrated that when the complete elimination or even reducing of grain boundaries were impossible, an alternative strategy was to control grain boundary orientation. [11] In this study monolayers of **8.1** were fabricated on substrates with different surface roughnesses. It is proven that by reducing the surface roughness, one can reduce the grain boundaries, as well as improve the film alignment.

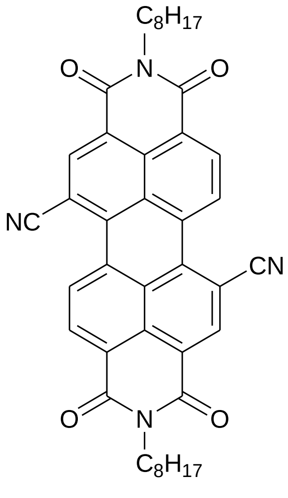

Scheme 8.1. Molecular structure of PDI8-CN$_2$, compound **8.1**.

8.2 Controllable growth of 8.1 monolayer and bi/tri layers on substrates with different surface roughness

A monolayer and its subsequent microstructure of **8.1** are successfully obtained from solution onto rigid OFET surfaces with different surface roughnesses. It is observed that a rough surface leads to small grain size due to 3D nucleation(growing into 3D crystalline domain) and hinders the long-range continuous alignment. On the other hand, a smoother surface is beneficial for larger grain growth via 2D nucleation(growing into 2D crystalline domain) and leads to improved crystalline ordering, as well as long-range alignment, being all favorable for the charge carrier transport. Remarkably enough, the film alignment on smoother surfaces occurs already for the monolayer, and is further extended to bi/tri layers. Hereby, the thickness from monolayer to bi/tri layers is precisely controlled by tuning the coating velocities. For all experiments, **8.1** was dissolved in chloroform to obtain a concentration of 1mg/ml and heavily doped silicon wafers with a thermally grown silicon dioxide layer 300 nm thick were used as substrates. The substrates were firstly cleaned using sonication in acetone for 10 min, following by sonication in isoproponal for 10 min (further experimental details can be found in the experimental section chapter 9.4).

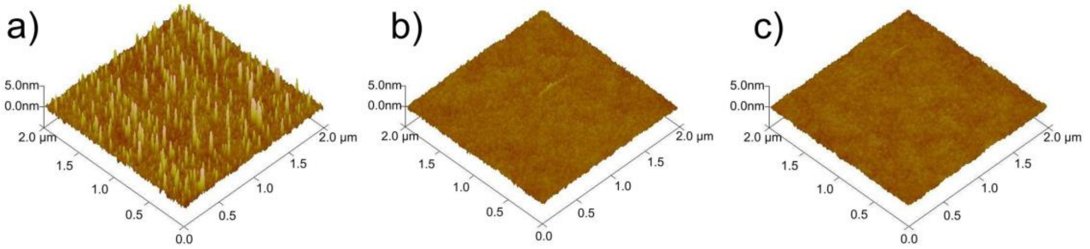

Figure 8.1. Tapping-mode 3-D AFM images of different surfaces: a) CVD modified SiO2 surface (rms=0.69nm), b) bare SiO2 surface (rms=0.24nm) c) plasma-treated surface (rms=0.19nm).

The as-prepared wafer surface was labelled as surface B, with an average roughness (rms) of 0.24 nm. For surface A, the as-prepared wafers (surface B) were placed in a desiccator together with two open vessels, one containing tetraethoxylilane (TES) (2 ml) and the other aqueous ammonia solution (2 ml). Chemical vapor deposition of TES was performed for 30 min at ambient temperature to grow a SiO_2 sub-monolayer. Thereafter, the samples were placed in a vacuum chamber (circa 1 mbar) for 2 h to remove TES or ammonia residuals. Chemical vapor deposition was performed by Xu Deng. The surface roughness was determined to be 0.69 nm. For surface C, as-prepared wafers (surface B) were further treated with oxygen plasma for 10 min, with an average rms of 0.19nm. Figure 1 showed the tapping-mode 3-D AFM images of different surfaces. All surface roughnesses were estimated from the images (1 × 1μm^2) obtained from average value of 5 points, and determined by root mean square (rms) of the AFM images.

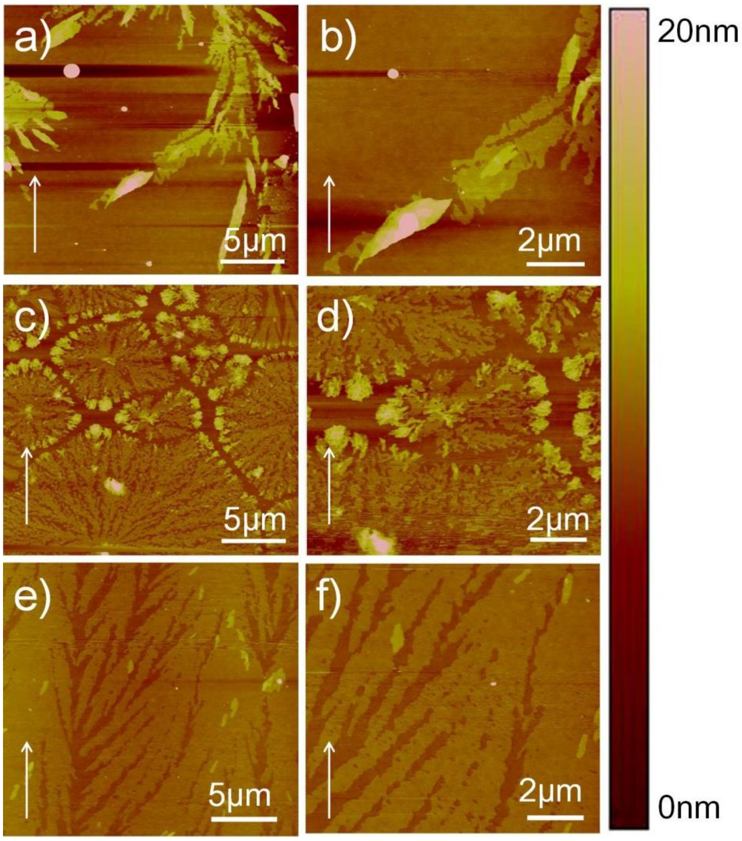

Figure 8.2. Tapping-mode AFM images of **8.1** monolayers obtained by dip coating on different surfaces: a) and b) surface A, c) and d) surface B, e) and f) surface C. White arrow indicates the dip coating direction.

As shown in Figure 8.2, monolayer films are fabricated onto the above mentioned three rigid OFET surfaces (Surface A: figure 1a, b B: figure 1c, d C: figure 1e, f) when pulling the substrate out of the solution at the speed of 1 mm/s. Figures 8.2a and 8.2b reveal a low surface coverage (approx. 15%) on surface A via 3D growth, resulting in a highest point ca. 8 nm, which is over 5 molecular layers. Interestingly, figures 8.2c and 8.2d show a higher surface coverage (approx. 60%) on the smoother surface B, forming dendritic microstructures with a high density of grain boundaries. Remarkably, deposition of **8.1** on surface C leads to a more homogeneously covered monolayer film. Moreover, this monolayer is already aligned along the dip coating direction, as shown in Figures 8.2e and 8.2f. However, a prerequisite for efficient charge carrier transport is a continous path between the source and drain electrode, and it is indicated in literature that a single layer of molecules is not sufficient for effective charge carrier transport. [11-12] Therefore, no field effect could be detected for these not fully covered monolayers. This result is in agreement with previous findings that a monolayer of small conjugated molecules is not sufficient for generating a field effect. [13-14] However, in contrast, a monolayer of conjugated polymer was proven sufficient to give field effect. In chapter 6, dip coating induced PBTTT monolayer gave a low charge carrier mobility of 1.6×10^{-4} $cm^2V^{-1}s^{-1}$. In chapter 7, dip coated P(NDI2OD-T2) monolayer showed a low charge carrier mobility of 6×10^{-4} $cm^2V^{-1}s^{-1}$. These low mobilities were attributed to the not fully covered monolayer of PBTTT and the grain boundary between fibers of P(NDI2OD-T2) monolayer. Previously it was also reported that a homogenous and continuous monolayer of P(NDI2OD-T2) can be obtained by LS technique, yielding a sufficient field-effect with pronounced mobility. These results are also in agreement with literature that for conjugated polymers, one layer is enough for creating field effect. [15] This can be attributed to the film characteristics of polymers that a continuous percolation can be formed between source and drain electrodes even when the first monolayer is not fully covered.

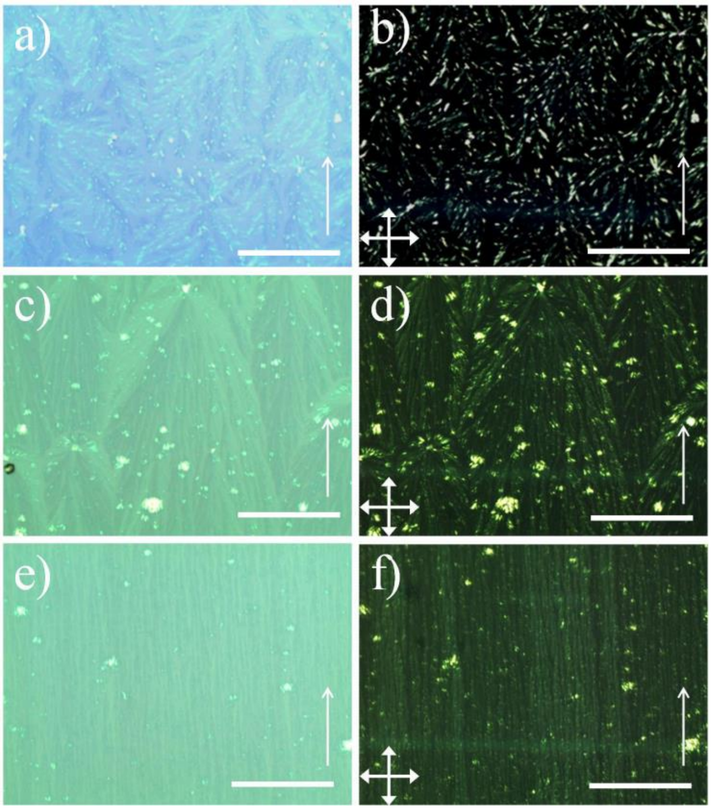

Figure 8.3. Reflection optical microscopy (OM) images of dip coated thin film on different surfaces: a) A, c) B, e) C; b), d) and f) are cross-polarized optical images of the thin films corresponding to a), c) and e), respectively. White arrow indicates the dip coating direction. Scale bar corresponds to 50μm.

Lowering the pulling speed to 40 μm/s leads to ultra thin films with few layers, which are firstly inspected by reflection optical microscopy (OM) images (Figure 8.3). The thicker layers are attributed to the lower pulling speed which ensures more molecules for building up of the microstructures on the SiO_2 surface. The morphology differences between the three different surfaces are enlarged from monolayer to bi/tri-layers: For surface A, a high density of grain boundaries is observed over the whole surface (Figure 8.3a), while for B, a smaller concentration is determined (Figure 8.3c). The film obtained on surface C (Figure 8.3e) is continuous over long-range and much more uniform as required for OFET applications. Under the cross-polarized optical microscope, the differences of these three surfaces are more pronounced (Figure 8.3b, 8.3d, and 8.3f). As is shown in Figure 3f, the film on the smoothest surface exhibits a homogenous birefringence and optical anisotropy indicating high molecular order and uniform orientation. Closer analysis of the AFM images further indicates structural differences between the samples (Figure 8.4). The film obtained on surface C is highly crystalline, with large domains extending several micrometers with a low number of grain boundaries.

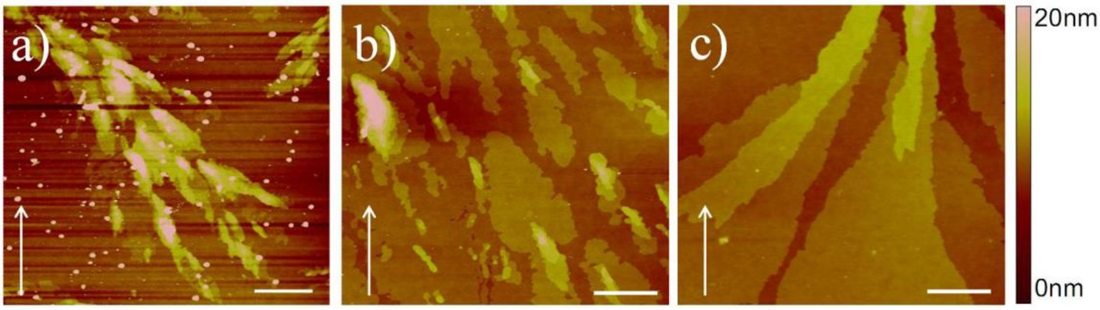

Figure 8.4. Tapping-mode AFM images of **8.1** obtained by dip coating on different surfaces: a) A, b) B, c) C. The scale bar in a), b) is 5μm in c) is 3μm.

8.3 OFETs based on PDI8-CN$_2$ bi/tri layers

All the dip coated films were annealed at 100 ℃ for 30 min to remove any residual solvent. To avoid any discontinuities in the film caused by differences in surface energy between Au electrodes and SiO$_2$ surface, the OFET devices were studied only in a top-contact configuration. Hereby, the surface energy quantifies the disruption of intermolecular bonds that occur when a surface is created.

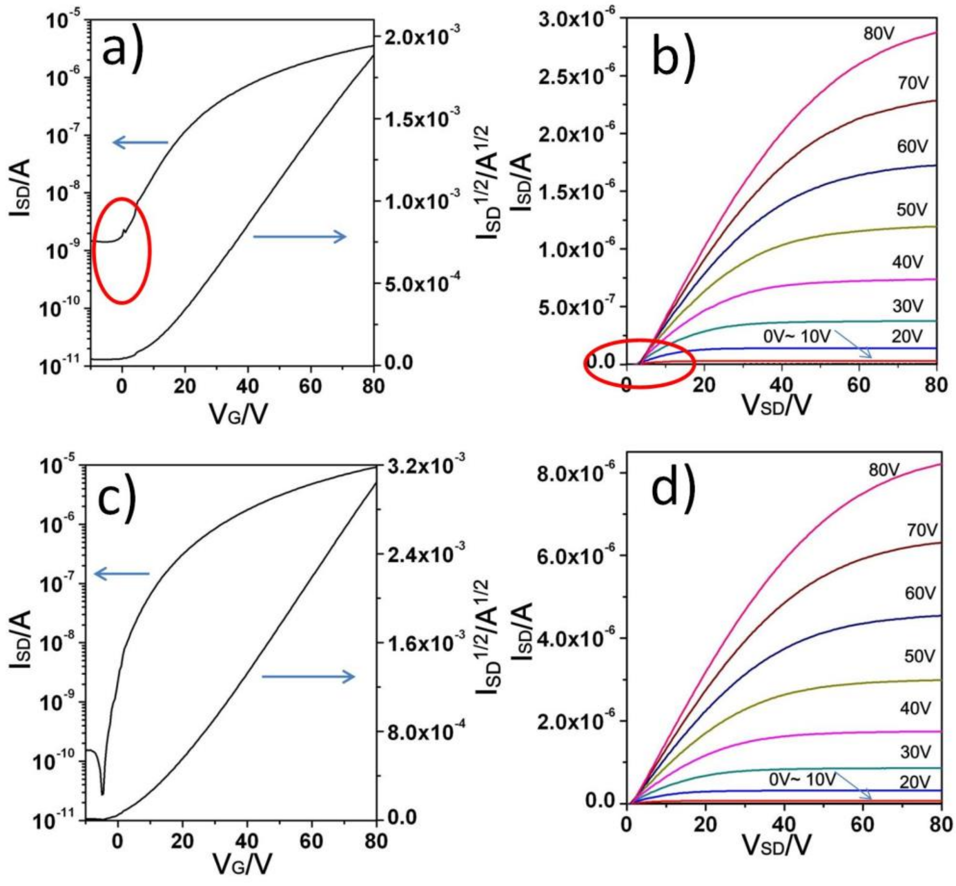

Figure 8.5. Transfer and output curves of the **8.1** films processed by dip coating on different surfaces: a) and b) device performance on surface B, c) and d) on C.

The resulting ultrathin films were contacted using a shadow mask under optical microscopy and OFETs were fabricated by evaporating source and drain gold electrodes, in this way establishing a bottom-gate, top-contact geometry. For the bottom gate, top contact OFETs, source and drain electrodes with channel lengths of 25 μm are defined by a shadow mask, followed by Au evaporation to a height of 50 nm. All standard electrical measurements were performed in a glove box under nitrogen atmosphere. It has to be emphasized that a prerequisite for efficient charge carrier transport is a continuous pathway between the source and drain electrode with intimately packed molecules. However, this is not the case for the layer in Figure 4a since the channel length of 20 μm is larger than the grains size. As a result, for OFET based on surface A, no field-effect was determined. Both devices on B and C surfaces exhibit typical n-type transistor behavior. For surface B, the average electron mobility is 0.0041 $cm^2V^{-1}s^{-1}$ with the maximum value of 0.0057 $cm^2V^{-1}s^{-1}$, with current on/off ratio ~10^3, the film on surface C yielded an average of 0.015 $cm^2V^{-1}s^{-1}$ and maximum of 0.02 $cm^2V^{-1}s^{-1}$, with current on/off ratio ~10^5 (Figure 8.5c and 8.5d). This mobility is in agreement with the previously reported performance of bottom-gate thin film transistors of the same semiconductor on bare SiO_2. [10-11] Obviously, the mobility on the plasma treated surface (C) shows 3~4 times higher than that on B. Significant differences are found also for the off-current which is ~ 10^{-9} for B (Figure 8.5a) and only ~10^{-11} for C(Figure 8.5c). It is known that the charge carrier transport in OFETs is limited by grain boundaries and molecular disorder within the domains which act as structural trapping sites. More precisely, in comparison to surface C, the grain boundaries of surface B act as dopants, thereby increasing the conductivity of the film and resulting in large leak currents with a relatively low on/off ratio. Another proof of the above mentioned effect is that the I-V output curves pass through the origin (Figure 8.5d). Obviously, lower threshold voltages of 0 V on surface C are obtained, in comparison to 8V on surface B. This is attributed to the decreased charge trapping at the organic/insulator interface and within the semiconductor layer itself.

It should be noted that the transistor fabrication by spin coating using highly volatile solvents such as chloroform results in poor device performance (μ<0.001$cm^2V^{-1}s^{-1}$), [17] whereas in this work dip coating is less sensitive to the solvent volatility characteristics. Remarkably enough, the films were simply deposited on SiO_2 dielectric without silanization, which is known as serious charge carrier trap, especially for n-type semiconductors[18]. Our results suggest that silinization is only one of factors contributing to high charge-carrier mobility. Recently researchers also observed that the electron mobility was unchanged both with and without OTS treatment for n-type conjugated polymer fibers based on **P(NDI2OD-T2)**. [19] Especially the above mentioned electron mobility was comparable to the best mobility reported in literature on a **P(NDI2OD-T2)** thin film which was deposited on OTS modified surface. Therefore it is claimed here that the key factor to optimize the device is by controlling film uniformity, long range order, as well as the density of grain boundaries. Hereby, besides silanization, surface roughness can play a leading role.

8.4 Conclusions

The effects of surface roughness on the microstructure evolution are probed by fabricating ultrathin films from monolayer to bi/tri layers via solution processing. The influences on microstructure evolution, alignment of first monolayer and device performance point towards an essential role of the surface roughness on the microstructure evolution and device performance. A rough surface (surface B) leads to small grain size and is detrimental for the long range continuous alignment. For even rougher surfaces (surface A) no continuous films are obtained resulting in no field effect. A smooth surface (surface C) is beneficial for the growth of large grains via 2D nucleation and yields in improved crystalline ordering, as well as long range alignment, which are favorable for the charge carrier transport. The film alignment on smoother surfaces occurs already for the first monolayer and further extends to bi/tri layers. The mobility on the smooth surface is 3~4 times higher than that on the rough surface. Although the effect of surface roughness on the film growth during vacuum deposition was previously studied, this is for the first time that the effect of surface roughness on solution-processed ultrathin layers is clearly illustrated. Our approach holds great potential for fundamental understanding of the role of surface roughness in determining the film alignment, density of grain boundaries, as well as device performance in solution processable OFETs.

REFERENCES

[1] S. Wang, W. Pisula, K. Müllen, *J. Mater. Chem.* **2012**, *22*, 24827.

[2] S. Wang, A. Kiersnowski, W. Pisula, K. Müllen, *J. Am. Chem. Soc.* **2012**, *134*, 4015.

[3] F. Zhang, C. Di, N. Berdunov, Y. Y. Hu, Y. B. Hu, X. Gao, Q. Meng, H. Sirringhaus, D. B. Zhu, *Adv. Mater.* **2012**, DOI: 10. 1002/adma.201204075.

[4] M. Shtein, J. Mapel, J. B. Benziger, S. R. Forrest, *Appl. Phys. Lett.* **2002**, *81*, 4383.

[5] J. Lee, K. Kim, J. H. Kim, S. Ima, *Appl. Phys. Lett.* **2003**, *82*, 4171.

[6] H. Klauk, D. J. Gundlach, J. A. Nichols, C. D. Sheraw, M. Bonse, T. N. Jackson, *Solid State Technol.* **2000**, *43*, 63.

[7] C. Di, G. Gyu, Y. Liu, Y. Guo, X. Sun, J. Zheng, Y. Wen, Y. Wang, W. Hu, D. Zhu, Phys. Chem. Chem. Phys. **2009**, *11*, 7268.

[8] K. Suemori, S. Uemura, M. Yoshida, S. Hoshino, N. Takada, T. Kodzasa, T. Kamata, *Appl. Phys. Lett.* **2008**, *93*, 033308.

[9] J. Rivnay, M. F. Toney, Y. Zheng, I. V. Kauvar, Z. Chen, V. Wagner, A. Facchetti and A. Salleo, *Adv. Mater.*, **2010**, *22,* 4359.

[10] A. Facchetti, *Adv. Mater.* **2008**, *20*, 3393.

[11] J. Rivnay, L. H. Jimison, J. E. Northrup, M. F. Toney, R. Noriega, S. Lu, T. J. Marks, A. Facchetti, A. Salleo, *Nat. Mater.*, **2009**, *8*, 952.

[12] C. Tanase, E. J. Meijer, P. W. M. Blom, D. M. d. Leeuw, *Org. Electron.* **2003**, *4*, 33.

[13]A. Ruiz, A. Papadimitratos, A. C. Mayer, G. G. Malliaras, Adv. Mater. 2005, 17, 1795.

[14] L. Li, P. Gao, K. C. Schuermann, S. Ostendorp, W. Wang, C. Du, Y. Lei, H. Fuchs, L. D. Cola, K. Müllen, L. Chi, *J. Am. Chem. Soc.* **2010**, *132*, 8807.

[15]S. Fabiano, C. Musumeci, Z. Chen, A. Scandurra, H. Wang, Y. Loo, A. Facchetti, B. Pignataro, *Adv. Mater.*, **2012**, *24*, 951.

[16] T. Schuettfort, B. Watts, L. Thomsen, M. Lee, H. Sirringhaus, C. R. McNeill, *ACS. Nano.* **2012**, *6*, 1849.

[17] L. L. Chua, J. Zaumseil, J. -F. Chang, E. C. -W. Ou, P. K. -H. Ho, H. Sirringhaus, R. H. Friend *Nature*, **2005**, *434*, 194.

[18] L. L. Chua, J. Zaumseil, J. -F. Chang, E. C. -W. Ou, P. K. -H. Ho, H. Sirringhaus, R. H. Friend Nature, 2005, 434, 19

[19] E. V. Canesi, A. Luzio, B. Saglio, A. Bianco, M. Caironi, C. Bertarelli, *ACS Marco Lett.* **2012**, *1*, 366.

.

Chapter 9

Conclusions and Outlook

9.1 Conclusions

To further understand the influence of semiconductor microstructure (termed as morphology in both mirco- and nanoscale) on the performance of organic field-effect transistors, different strategies were employed in this thesis. Hereby, two solution processing methods, including novelly designed solvent vapor diffusion and conventional dip coating, were precisely tailored for different semiconductor molecular systems. These techniques allow to control the self-assembly, improve the molecular order, reduce the grain boundaries, and finally to significantly improve their charge carrier mobilities in OFETs. I summarize these different strategies as follows:

1. To overcome the disadvantages of conventional solution processing techniques which suffer from dewetting, a novel solution processing method solvent vapor diffusion (SVD) was designed to tune the self-assembly of semiconductor molecules on the surface. This method was proven to be a powerful tool which allowed a delicate control over the microstructure as presented in chapter 3 for a D-A dyad composed of covalently bonded hexa-*peri*-hexabenzocoronene (HBC) as donor and perylene diimide (PDI) as acceptor (HBC-PDI). In this study, several important processing parameters were optimized in order to balance dewetting effect and intermolecular interactions. For instance, by choosing solvents with different polarities, one can tune the interactions between solvent-substrate, and

solvent-molecule; while by modifying the surface with different surface energy monolayers, the interactions between molecule-surface and molecule-molecule can be adjusted. The combination of surface modification and solvent vapor can balance dewetting effects and the above mentioned various forces, and finally achieve the desired microstructure and molecular organization on the surface. This work allowed a fundamental understanding of how processing parameters influenced microstructure evolution of semiconductor molecules. For semiconductor molecules showing low self-assembly tendency when deposited by conventional solution processing, SVD opens new avenues and yields self-assembling into well defined microstructures. As a new fabrication method, SVD gave control over the microstructure evolution of semiconductor molecules during the solvent evaporation into highly ordered objects. In chapter 4 and chapter 5, SVD was further proven to be a versatile approach to influence the (macro) molecular self-assembly.

2. To improve the charge carrier mobility, one promising strategy is to self-assemble of semiconductor molecules to create defect-free, highly ordered objects in the meso-scale. In this aspect, the utilization of the above mentioned SVD method and the realization of highly ordered microstructures were combined in chapter 4 and chapter 5, where 1D single crystal microribbons based on dithieno[2, 3-*d*;2’, 3’-*d*’] benzo[1,2-*b*;4,5-*b*’]dithiophene (DTBDT) and 1D fiber based on cyclopentadithiophene-benzothiadiazole copolymer (CDT-BTZ copolymer) were successfully fabricated, yielding unprecedented charge carrier mobilities. The structural study of the DTBDT crystals indicated a most favorable arrangement in the ribbons that the *a* plane is oriented along the ribbon axis. Such arrangement is ideal for the OFETs applications because the carrier can transport freely along ribbon axis, the stacking direction. An individual crystal DTBDT OFETs exhibited OFETs mobilities as high as 3.2 $cm^2V^{-1}s^{-1}$, approximately a two-fold improvement in comparison to the dip-coated films.

In chapter 5, CDT-BTZ copolymer single fibers were obtained, exhibiting charge carrier mobilities as high as 5.5 $cm^2V^{-1}s^{-1}$, three times higher than the device based on the corresponding dip coated films. From structural analysis, it was oberseved that the high molecular order increased crystallinity in the fiber for the alkyl side chains appearing as sharp reflections in the electron diffraction pattern. This leaded to a decrease of structural defects as trapping sites. Another remarkable effect is that the alignment of CDT-BTZ backbones was proven to be along the fiber axis which presents the fastest charge transporting direction. In order to achieve the best optimized device performance, two strategies were taken during the electrodes deposition. One was to shorten the transistor channel length to reduce the number of structural defects. Another was to exclude the negative effect caused by Pt overspray during FIB via depositing a SiO_2 protection layer on top of the copolymer fibers. It should be noted that these devices still suffered from contact resistance, which had a negative influence on the charge carrier injection. Nevertheless, such a challenging goal to achieving high performance has been achieved in particular by considering both delicate control over the self-assembly and the optimization of electrode deposition. These results and strategies point to the importance of taking consideration of all the relevant parameters during the device fabrication, which may stimulate further study and shed light on the other high performance conjugated polymers for achieving their unprecedented device performances.

3. To get a fundamental understanding on the role of the first monolayer for the evolution of the bulk polymer microstructure and the charge carrier transport in transistors, in chapter 6 and chapter 7 monolayers and their subsequent microstructures of two high performance conjugated polymers (p-type Poly (2,5-bis(3-alkylthiophen-2-yl)thieno[3,2-b]thiophene) PBTTT and n-type poly{[*N* , *N* ′-bis(2-octyldodecyl)-naphthalene-1,4,5,8-bis(dicarboximide)-2,6-diyl]-*alt*-5,5′-(2,2′-bithiophene)}, P(NDI2OD-T2)) on a rigid surface were obtained by dip coating. This is the first time that polymer monolayers were successfully fabricated by solution

processing. These results indicated an essential role of the first polymer monolayer on the microstructure evolution not only in the bulk film during solution processing, but also in the charge carrier transport in the transistor. In both cases, it was observed that monolayer was not sufficient for a high performance, which required a critical multilayer network for creating the required percolation pathways. The thickness of polymer layers can be precisely controlled via tuning the pulling speed of the substrate during dip coating. This allowed a close detection on the microstructure evolution from the early stages of polymer film formation and on the relationship between the layer thickness and device performance . Moreover, for both studies, significant improvement of the charge carrier transport occured upon completion of the bottom two to three fibrous monolayers. Remarkably, both polymer films were aligned at a low dip coating speed. For PBTTT, structural analysis indicated that polymer chains were uniaxially oriented and corresponding thin films yielded pronounced structural anisotropy and high charge carrier mobilities in the alignment direction. For P(NDI2OD-T2), the thin films obtained on bare SiO_2 exhibited satisfying device performance comparable to the best value obtained from bottom gate devices with OTS treatment.

Another interesting finding is that, for PBTTT**,** a striking difference between the first monolayer and the subsequent microstructure was observed. The first monolayer revealed 2D microstructure, while the subsequent layers exhibited 1D fibers, which were considered to be the result of the different surface tension of PBTTT and SiO_2. In contrast to PBTTT, P(NDI2OD-T2) showed no microstructure differences between different layers. The different self-assembly tendency between PBTTT and P(NDI2OD-T2) monlayer was attributed to the bulky branched side chains of P(NDI2OD-T2) leading to stronger hydrophobic interactions between the molecules. Such an interesting finding suggested that the self-assembly of polymers from solution into the first few layers strongly depended on the design of the backbone, as well as the attached substituents. Therefore, our strategy provides new insights into the fundamental understanding of solution processable OFETs based on polymer thin films. Conceivably, this approach opens exciting perspectives for the bottom-up fabrication of polymer ultrathin films from the monolayer to multilayers and therefore can be further exploited for a broad range of other high performance conjugated polymers.

4. To probe the role of surface roughness in determining the microstructure evolution and carrier transport of solution-processed semiconductors, in chapter 8 PDI8-CN_2 films from monolayer to bi/tri layers were successfully fabricated on substrates with different surface roughnesses. This is for the first time that the effect of surface roughness on solution-processed ultrathin layers was clearly illustrated.

A rough surface (rms= 0.24nm) leaded to small grain size and was detrimental for the uniformity and alignment over long range. For even rougher surfaces (rms > 0.5nm) no continuous films were obtained, thus resulting in no field effect mobility. However, a smooth surface (rms < 0.2nm) was beneficial for larger grain growth and leaded to improved crystalline ordering, as well as long range alignment, all of which were favorable for charge transport. It is important to note that the film on smoother surface (rms < 0.2nm) already started to align even from monolayer and this alignment was further extended to bi/tri layers. In devices, the charge carrier mobility on smoother surfaces was 3~4 times higher than that on rough surface. It was observed that the key factor to optimize the device is by controlling the surface roughness, which influences film uniformity, long range order, as well as the density of grain boundaries. This approach provides new insights into the fundamental understanding of the effects of surface roughness in solution processable OFETs, therefore could be further exploited for a broad range of other conjugated systems.

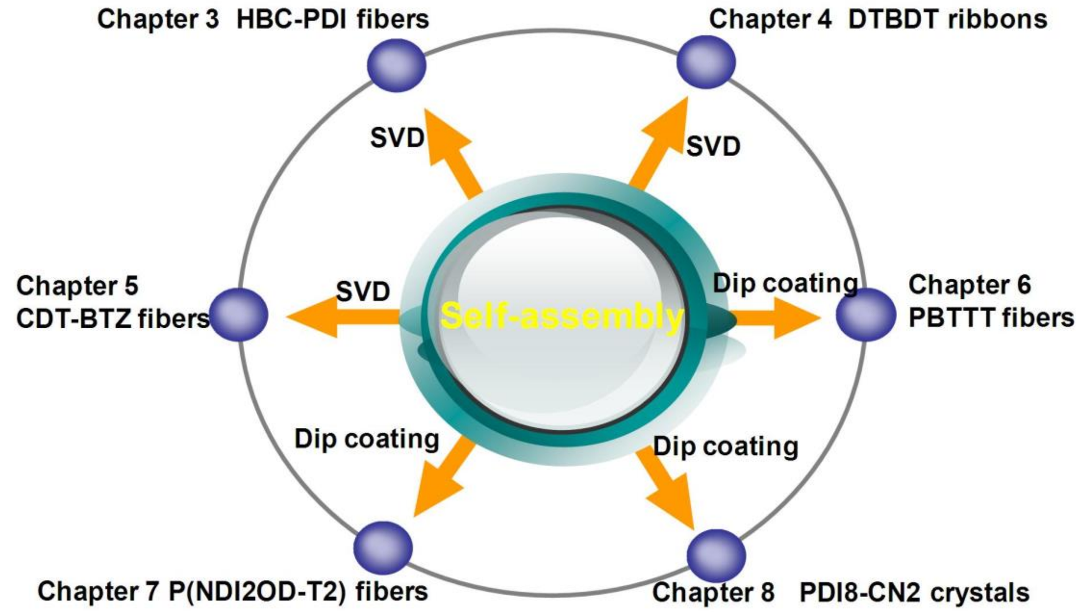

Figure 9.1. Interconnections between different chapters in the whole thesis.

All of the above mentioned topics are well intercorrelated, as shown in Figure 9.1. For instance, the combination of designing novel processing methods and fabricating highly ordered structure is well demonstrated in the thesis. Moreover, except for chapter 8 which is based on the crystalline structure, all of these topics have one common feature, that they are related to 1D highly ordered structures, e.g. fibers, ribbons. Not regarding contact resistance and injection problems; from the high degree of molecular order, it is expected that these 1D defect-free structures are infinitely close to the intrinsic properties of semiconductor molecules. Therefore, these findings in my thesis could contribute to a deeper insight into the field of high performance OFETs.

9.2 Outlook

Nevertheless, there are still challenges in the field of OFETs. For instance, 1D nano- or microstructure based OFETs are promising due to their unprecedented device performance. But a future challenge is their further applicability in a fast continuous process for practical applications in fabrication. Especially, technical questions concerning micromanipulation and precise positioning of high performance mesoscopic fibers/ribbons on more complex circuits in multi-array devices must be answered. An implementation of such high-performance polymer fibers in multi-array devices requires surface patterning to accurately place and align the objects towards the contacts. [1, 2]

In addition, although tremendous progress has been made in improving mobility through developing new materials and optimization the molecular packing, the need for higher mobility OFETs is still compelling. In contrast to organic semiconductor molecules, carbon-based materials such as carbon nanotubes and graphene exhibit pretty high mobility, but suffer from low on/off ratio in OFETs. To enhance the mobility while keeping the on/off ratio sufficiently high, one can create hybrid materials by blending organic semiconductor materials with carbon-based materials. There have been literature reporting organic semiconductor/carbon nanotubes (CNTs) hybrid OFETs, [3-7] and it is observed that the mobility increased remarkably; however, the on/off ratio appears to decrease just as the conductivity increases. This can be attributed to the fact that 1D carbon nanotubes start to percolate at low density; when there are sufficient amount of carbon nanotubes mixed into the organic semiconductor film to drastically enhance the mobility. The density of the CNTs appears to approach the percolation threshold, thus limiting the maximum mobility achievable before the percolation of CNTs reduces the on/off ratio of the transistor. In comparison to CNTs, graphene is a 2D lattice of carbon with single atom thickness. It is expected that few layer graphene flakes can provide good connection.[8] However, another question arises concerning the solution deposition of the semiconductor/graphene composites. Since graphene is only soluble in certain solvents such as DMF, which is a poor solvent for most of the organic semiconductors. This makes the blending process of semiconductor/graphene difficult. Solving this problem relies on the proper deposition of graphene and organic semiconductors separately using different solvents.

REFERENCES

[1] S. C. B. Mannsfeld, A. Sharei, S. Liu, M. E. Roberts, I. McCulloch, M. Heeney, Z. Bao, *Adv. Mater.* **2008**, *20*, 4044.

[2] Y. Xu, F. Zhang, X. Feng, *Small* **2011**, *10*, 1338.

[3] X. Z. Bo, C. Y. Lee, M. S. Strano, M. Goldfinger, C. Nuckolls, G. B. Blanchet, *Appl. Phys. Lett.* **2005**, *86*, 182102.

[4] J. X. Geng, B. S. Kong, S. B. Yang, S. C. Youn, S. Park, T. Joo, H. T. Jung, *Adv. Funct. Mater.* **2008**, *18*, 2659.

[5] S. Liu, S. C. B. Mannsfeld, M. C. LeMieux, H. W. Lee, Z. Bao, *Appl. Phys. Lett.* **2008**, *92*, 053306.

[6] Y. D. Park, J. A. Lim, Y. Jang, M. Hwang, H. S. Lee, D. H. Lee, H. J. Lee, J. B. Baek, K. Cho, *Org. Electron.* **2008**, *9*, 317.

[7] G. W. Hsieh, F. M. Li, P. Beecher, A. Nathan, Y. Wu, B. S. Ong, W. I. Milne, *J. Appl. Phys.* **2009**, *106*, 123706.

[8] J. Huang, D. R. Hines, B. J. Jung, M. S. Bronsgeest, A. Tunnell, V. Ballarotto, H. E. Katz, M. S. Fuhrer, E. D. Williams, J. Cumings, *Org. Elecron.* **2011**, *12*, 1471.

.

Chapter 10.

Experimental details

10.1 Dip coating

Semiconductor molecules were firstly dissolved in organic solvent to form a homogeneous solution. An open glass container with a total volume of 9 ml was used for dip coating. The silicon wafer with 300 nm SiO_2 thermally grown layer was immersed vertically into the solution and then was withdrawn at a defined speed, controlled by a high-precision linear motor stage (Figure 10.1). The whole set-up is entirely made in our own laboratory. The whole process can be divided into 3 stages:

1. Immersion: the substrate is immersed in the semiconductor solution, controlled by the motor (Figure 10.1a).

2. Withdraw: the substrate is withdrawn slowly out of the solution. The speed can be tuned from 1um/s to 2mm/s which is controlled by the high-precision motor (Figure 10.1b).

3. Solvent evaporation and thin layer formation: the organic solvent evaporates from the surface, forming thin semiconductor layer on the substrate.

There are several parameters to control during dip coating process, such as pulling speed, the choice of solvents, solution concentration, and solution temperature. In this thesis, dip coating was employed in chapter 6, 7, 8. Chloroform was chosen as solvent for all the systems. The parameters such as dip coating rate and solution concentration are specified in detail in each chapter. For instance, in chapter 6, the solution was set at a constant concentration of 0.3 mg/ml; the dip rate was set from the fastest speed of 1mm/s to the lowest speed of 2µm/s. In chapter 7, the solution was set at a constant concentration of 0.5 mg/ml; the dipping rate was set from the fastest speed of 1mm/s to the lowest speed of 1µm/s. In chapter 8, the solution was set at a constant concentration of 1 mg/ml; the dipping rate was set from the fastest speed of 1mm/s to the lowest speed of 1µm/s. All the experiments were carried out at ambient laboratory condition (humidity ca 50.0, pressure ca 1000 hPa). The size of the substrate was around 1×1 cm^2.

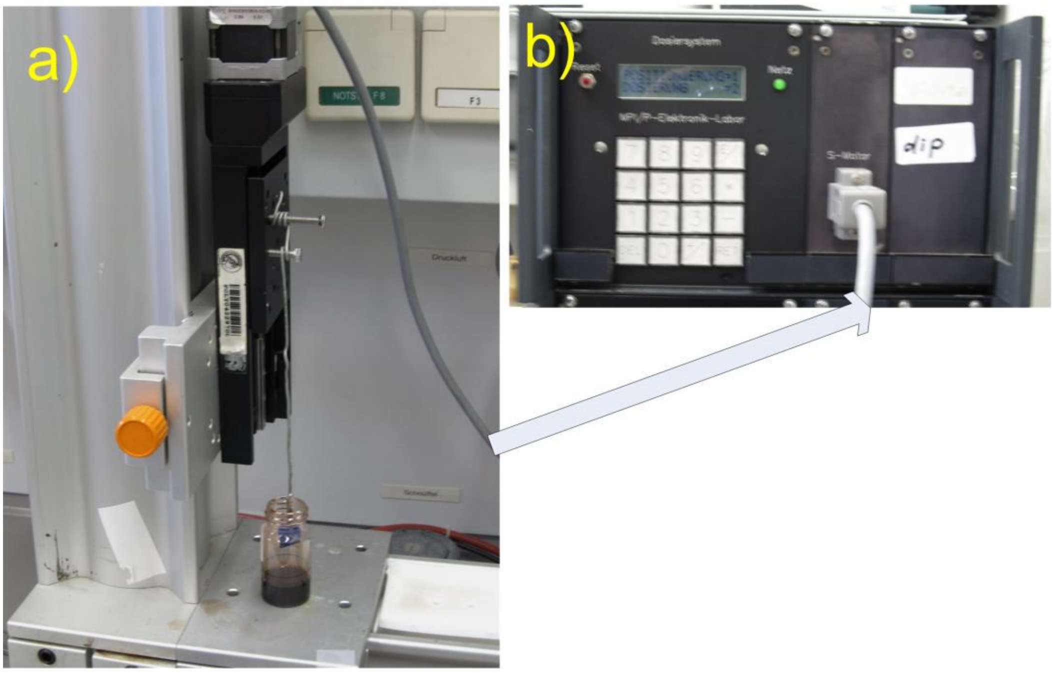

Figure 10.1. Dip coating set-up. a) high-precision motor pulling the substrate out of the solution, b) motor controller.

10.2 Solvent vapor diffusion

In order to control over the microstructure of organic semiconductors on the surface, I developed solvent vapor diffusion (SVD) in our laboratory. During this process, a drop cast solution is exposed to a saturated solvent vapor atmosphere in an airtight container (Figure 10.2). The major advantage of this process is its ability to minimize dewetting effects via carefully adjusting the evaporation rate of the solution by the right choice of the saturated solvent vapor. As a result, this ensures the formation of macroscopically homogenous thin layers. During SVD, the evaporation rate can be adapted by choosing different solvent. Other processing parameters can also be adjusted including solution concentration, choice of solvent vapor, different surface energy, plate temperature, as well as polar/apolar co-solvent conditions under which the solvent polarity forces solvophobic association between the alkyl side chains. (Figure 10.2)

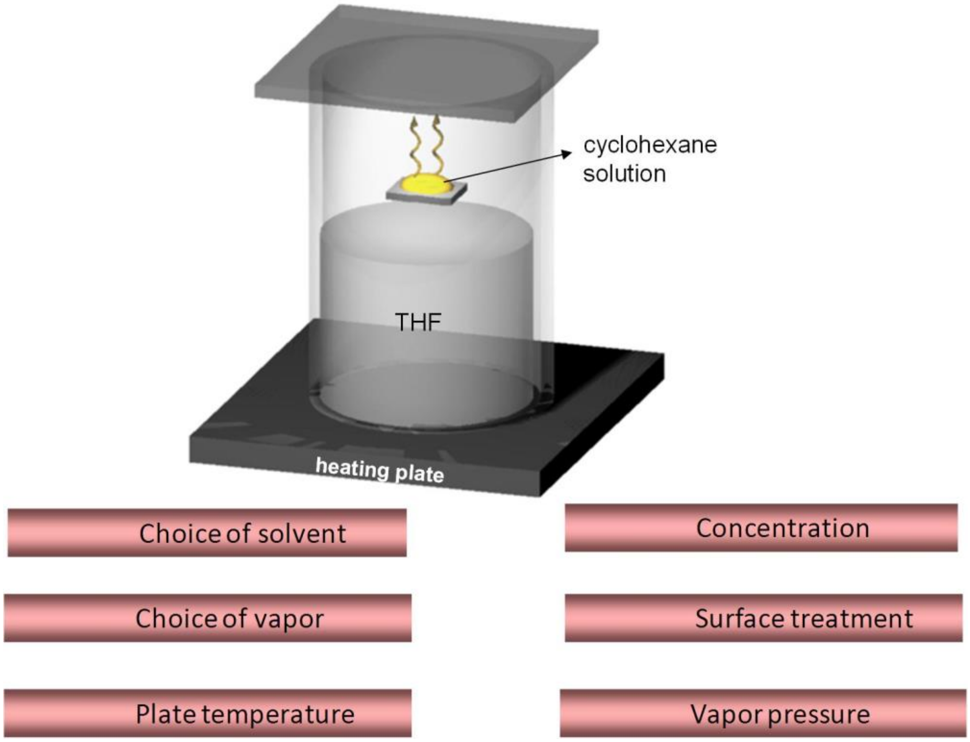

Figure 10.2. Schematic illustration of the solvent vapor diffusion and all the parameters that could be tuned during this process.

The molecular self-assembly from solution is determined by a complex combination of interactions between molecule-molecule, molecule-substrate, molecule-solvent, and substrate-solvent. (Figure 10.3) To obtain a control over the microstructure, a subtle balance of all these interactions involved must be achieved. By choosing solvent, we can tune the interactions between solvent-substrate, and solvent-molecule; while by modifying the surface, one can tune the interactions between molecule-surface and molecule-molecule. Here SVD assisted self-assembly and microstructure formation from solution was demonstrated on the example of HBC -PDI in chapter 3. Several droplets of HBC-PDI solution in cyclohexane (around 20 µL) were drop cast on silicon wafer (1×1 cm^2) which was exposed to an airtight container saturated with solvent vapor (container volume: 100 ml filled with 60 ml solvent such as hexane, methanol, THF, or toluene for creating solvent vapor).

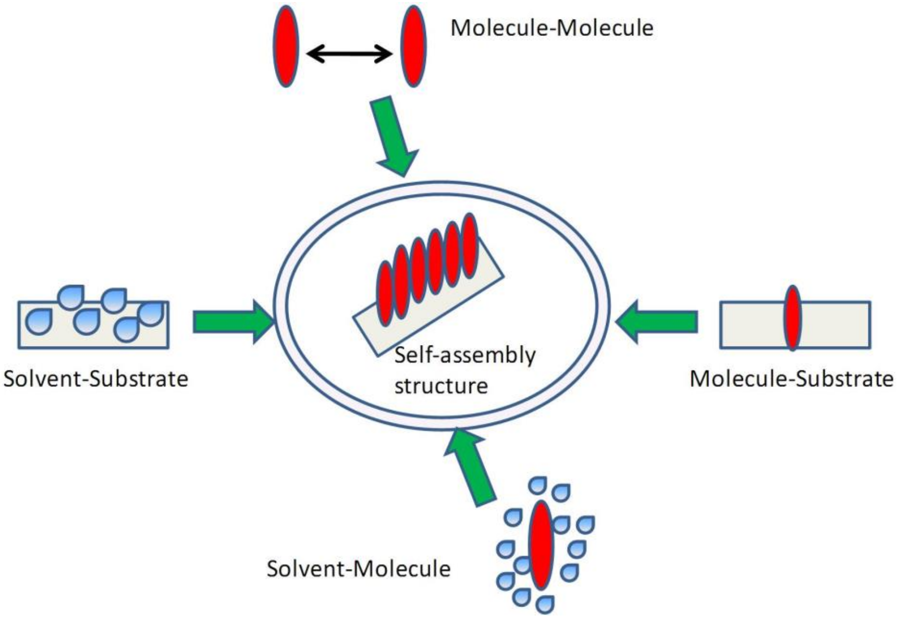

Figure 10.3. Schematic illustration of interactions which dominate the molecular self-assembly from solution.

Before placing the substrate inside the container a saturated solvent vapor atmosphere was created. It took 70, 120, 15, and 10 minutes for the drop cast solution to evaporate completely in THF vapor, hexane vapor, methanol vapor, toluene vapor atmophere, respectively. As soon as the drop fully evaporated, it was taken out of the container for characterizations. For comparison, the same cyclohexane solution drop evaporated completely within 1.5 minutes in air. Among all the solvent vapor used in this study, THF is polar and can be exploited for a polar/apolar co-solvent environment with nonpolar cyclohexane as the solvent. Finally, after cyclohexane completely evaporated, the molecules arranged within the thin layer in an edge-on fashion. The same phenomenon happened when choosing methanol as vapor which is also a polar solvent. The increase in solvent polarity could also induce solvophobic association between the alkyl side chains in 1D self-assembly. [1, 2] As a result, minor fibrillar structures and larger aggregates were formed. However, it was not as well-defined as in the case of THF. Finally, THF was chosen as the best solvent vapor for the whole study. All experiments were performed under ambient temperatures.

Besides in chapter 3, solvent vapor diffusion was also employed in chapter 4, and 5. The parameters such as the choice of solvent, solvent vapor and temperature were specified in detail in each chapter. For instance, in chapter 4, several droplets of DTBDT solution in cyclohexane (around 20 µL) were drop cast on silicon wafer which was exposed to an airtight container saturated with solvent vapor (container volume: 500 ml filled with 50 ml THF). In chapter 5, several droplets of a 0.05 mg/ml dichlorobenzene solution of CDT-BTZ (around 20 µL) were drop cast on a SiO_2 surface which was exposed to saturated solvent vapor atmosphere in an airtight container. (Container volume: 100 ml filled with 10 ml dichlorobenzene).The container was kept at 60 ^{o}C to ensure a saturated vapor atmosphere.

10.3 OFET Device Fabrication and Measurements:

The fabrication of OFET devices consists of the following steps:

—Cleaning of the substrate

—Surface modification of the substrate

—deposition of the organic semiconductor materials

—Deposition of top electrodes

Cleaning of the substrate: For all devices, heavily doped silicon wafers with a thermally grown silicon dioxide layer 300 nm thick were used as substrates. The substrates were firstly cleaned using sonication in acetone for 10 min, following by sonication in isoproponal for 10 min, and finally these substrates were cleaned with oxygen plasma for 10 min.

Surface modification of the substrate: For the substrates in Chapter 3, 4, 5, a self-assembled monolayer of 1,1,1,3,3,3-Hexamethyldisilazane (HMDS) was deposited from the vapour phase. HMDS in electronic grade was purchased from Alfa Aesar. Around 0.5mL (ca. 20 droplets) of HMDS was dropped into a small petri dish which was located in the center of the airtight glass container. The glass container was sealed and placed in an oven at 135 °C for 2h. Hereby, the whole glass container was filled with HMDS vapor which was then attached onto the SiO_2 surface, forming methyl endcapped interfaces. Finally the substrates were taken out of the container and rinsed by isopropanol, drying with nitrogen.

For the substrates in Chapter 3, octyltrichlorosilane (OTS) treatment was processed by dipping the substrate into OTS solution ($1x10^{-4}$ mol/l of OTS solution was made with hexane solvent) for 1h. [3] After that the substrates were taken out of the container and rinsed by isopropanol, drying with nitrogen before use.

Deposition of top electrodes: The gold evaporation was performed in an UNIVEX 350G evaporator which was located in glove box, and is controlled by Leybold systems (Figure 10.4). Gold electrodes were evaporated on top of the single fiber/ribbon (in chapter 4 and 5, channel length 20μm, length/width ratio=1: 20) and on top of the organic semiconductor layer (in Chapter 6, 7 and 8, channel length 25μm, length/width ratio=1: 20). Firstly the samples were put on the sample holder, and then the masks were fixed onto the samples by magnetic stone. Following, the shutter was closed and the whole system was vacuumed. Finally gold was deposited on top of the semiconductor layer. The thickness of gold was tuned by the controller. In this thesis, the thickness in Chapter 4, 5, 6, 7 is 100nm and in chapter 8 is 50nm.

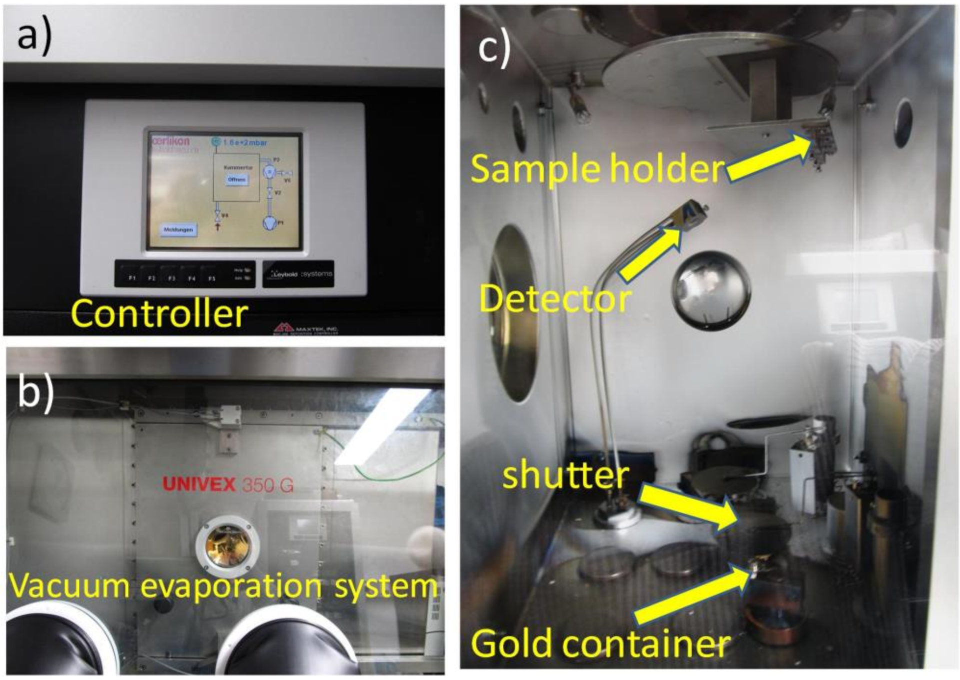

Figure 10.4. Gold deposition system. UNIVEX 350G evaporator was controlled by Leybold systems. a) Controller, b) vacuum evaporation system, c) boat, detector and sample holder inside the vacuum system.

Focused ion beam deposition: In chapter 5, for the bottom gate, top contact OFETs, source and drain electrodes with channel lengths of 3-5 µm were fabricated in a focused ion beam (FIB) instrument (Nova 600 Nanolab, FEI, Hillsboro, OR, USA,) by means of gas assisted FIB deposition of platinum from the metalloorganic precursor methylcyclopentadienyl(trimethyl)platinum(IV). Typical length, width and thickness of the Pt that formed the electrodes were 10 µm, 1 µm and 200~600 nm, respectively.

Electrical connection of the gold electrodes to the CDT-BTZ fibers was established via Pt microelectrodes that were fabricated by gas assisted FIB deposition of Pt in a FEI Nova 600 Nanolab dualbeam instrument, (Figure 11.5) which combined SEM and FIB within one instrument. This allowed finding the CDT-BTZ fibers and defining the position of the microelectrodes using the SEM without damaging the fibers with the focused ion beam.

Figure 10.5. Focused ion beam deposition system.

A beam current of 10 pA corresponding to an extremely low beam current density of ~ 1pA/μm^2 was selected to ensure deposition of Pt without sputtering of the underlying CDT-BTZ fibers. With a typical specific resistivity of the Pt deposit of 2 × 105 Ωm, the series resistivity of the pair of Pt electrodes with total length L of 20μm, width W of 1μm and height h of 200 nm can be estimated to be around 2 kΩ. For the maximum currents used in the OFET measurements of around 10 μA, the Pt electrode resistance would lead to a voltage drop of 20 mV, which was totally negligible compared to the corresponding values of the source-drain voltage of -60 V.

10.4 Characterizations

10.4.1 Optical microscopy: The optical textures of the compound were investigated using a Zeiss Axiophoto microscope equipped with a Hitachi Kp-D50 color digital CCD camera.

10.4.2 Atomic force microscopy:

Atomic force microscope (AFM) is a high-resolution scanning probe microscopy, allowing probed features in the nanometer to micrometer scale. From the height mode imaging it is possible to get film roughness, grain boundaries, etc. From phase mode imaging one can observe the phase segregation. AFM is widely used to get structural and morphological information in material science. Nevertheless, it can only probe top surface of the film and it could not determine the buried interface. In all work in this thesis, AFM images were obtained with a Digital Instruments Nanoscope IIIa AFM in tapping mode. The machines I used are Multimode and Dimension 3100/3100CL (Figure 10.6). Here, Multimode is used to measure relatively small scale up to 10 microns. Also, there is limitation of the piezoelectric support. Therefore, the dimensions of the sample should not exceed $1 \times 1\mathrm{cm}^2$. While Dimension 3100 can be employed to detect larger scale up to 100μm, and the samples remain stationary when the probe scans forth and back above them.

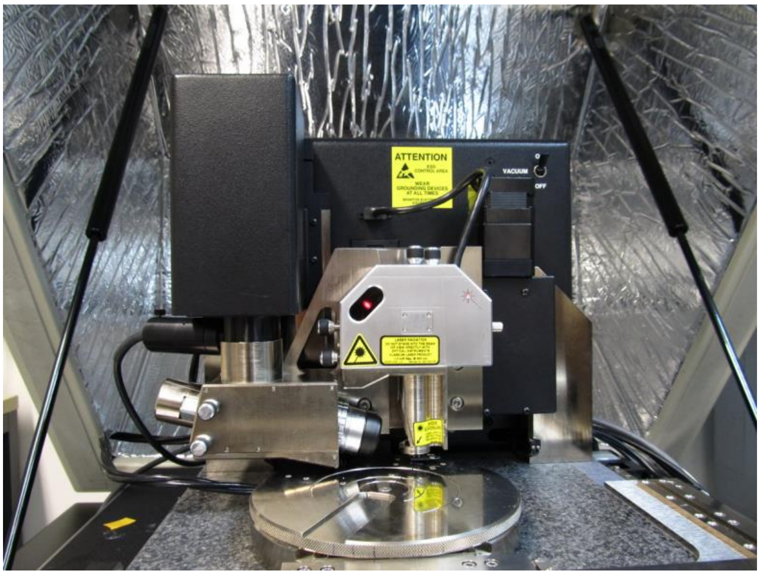

Figure 10.6. AFM dimension 3100 setup.

10.4.3 Transmission electron microscopy:

TEM is widely used to determine the morphological information in small molecules films and single crystal structures. A beam of electrons transmits an ultra thin specimen, interacting with the specimen as it passes through, during which the image is formed and magnified, and then the image is focused onto an imaging device with a fluorescent screen, being detected by a CCD camera. Owing to the small de Broglie wavelength, TEM is capable of imaging at a significantly higher resolution (tens of thousands times) than light microscopes. This allows one to determine the samples in greater details, e.g. as small as a single column of atoms. [4, 5] Therefore, TEM is a major analysis method in materials science.

Figure 10.7. TEM dimension 3100 setup.

Inside TEM, usually selected area electron diffraction (SAED), a crystallographic experimental technique, can be performed. During the measurement, a thin crystalline specimen is subjected to a parallel beam of high-energy electrons. The electrons typically have energy of 100-400 kiloelectron volts, and a few thousandths of a nanometer (hundred times smaller than the spacing between atoms in a solid), thus can easily passing through the samples. Hereby, electrons are in wave-like form, rather than particle-like form, in wave-particle duality. The atoms act as a diffraction grating to electrons. [6] Some fraction of them will be scattered to particular angles, determined by the crystal structure of the sample, while others continue to pass through the sample without deflection. As a result, the image on the screen of the TEM will be a series of spots, the so-called selected area diffraction pattern, with each spot corresponding to a satisfied diffraction condition of the sample's crystal structure. If the sample is tilted, the same crystal will stay under illumination, but different diffraction conditions will be achieved, and different diffraction spots will appear or disappear. [7-8] For this measurement, one can choose any part of the specimen to obtain the diffraction pattern. For instance, for the DTBDT ribbon in chapter 4, no change of the SAED pattern is observed for different parts of the same ribbon, indicating single crystallinity of the 1D object.

In chapter 4 and chapter 5, TEM of the single crystal microribbons and single polymer fibers were carried out on a FEI tecnai F30 ST (Figure 11.7) at 300 kV under liquid N_2 cryoconditions. SAED was recorded using a Philips CM 12 electron microscope at 120V acceleration voltage.

10.4.4 X-ray diffraction:

XRD is a facile and non-destructive technique to elucidate microstructure and morphological features in orders of magnitude length scales, from sub-Angstrom molecular chemistry to device-scale alignment. [9] Powder diffraction is usually employed to determine crystal phase and structure for inorganic species. Since organic semiconductors readily form films for devices, it is of vital significance to directly investigate thin films. Wide-angle X-ray scattering (WAXS) is usually employed to investigate the self-organization of organic materials. [9-10] There are commonly used specular (Figure 10.8a) and grazing geometries.[9]

When the scattering vector is normal to the sample plane (q_z), the observed intensity pattern describes the periodicity out of the substrate plane. This case is known as the true specular geometry (Figure 10.8a). While when it points only along the sample plane (q_{xy}) the diffracting lattice planes are perpendicular to the sample plane. In such case, a glancing incident angle is used below the critical angle of the substrate. Hereby, when this angle is above that of the film, one can probe the bulk. When it is below that of the film, one can probe near surface structure. [9]

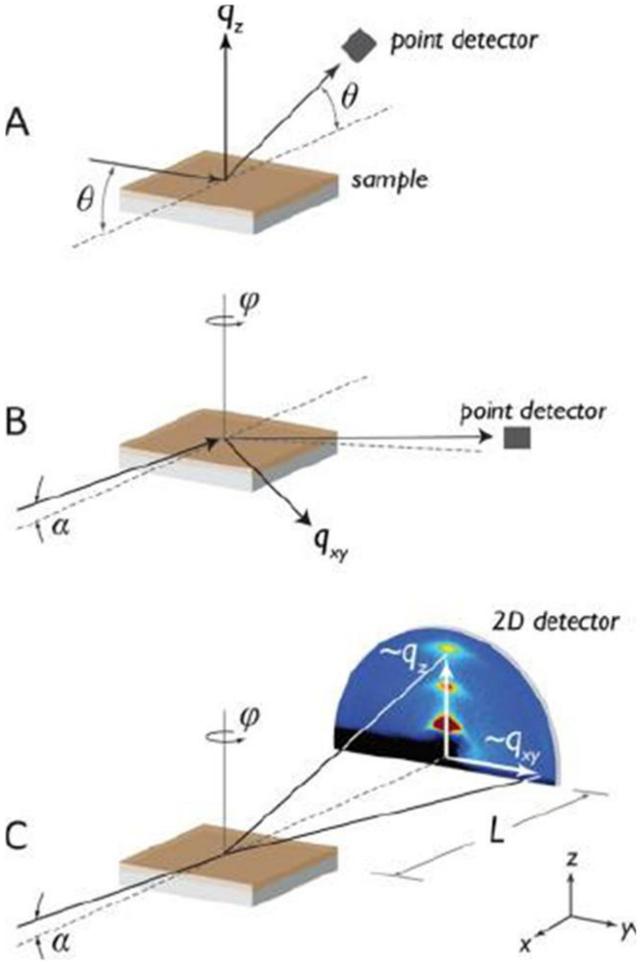

Figure 10.8. Wide-angle X-ray scattering geometries on thin films. a) Specular diffraction used in powder diffraction. b) Grazing incidence wide-angle X-ray diffraction with a point detector. c) Grazing incidence X-ray with a 2D image plate. [10]

In chapter 4, and chapter 7, XRD was performed on a θ-θ Philips PW 1820 kristalloflex diffractometer with a graphite-monochromatized Cu Kα X-ray beam incident on a fiber film on SiO_2 silicon wafer substrate at room temperature. In chapter 3, 2D-WAXS experiments were performed using a rotating anode (Rigaku 18kW) X-ray beam with pinhole collimation and a 2D Siemens detector. A double graphite monochromator for the CuKα radiation (λ=0.154nm) was used. In chapter 6, GIWAXS measurements were performed using a custom setup consisting of rotating anode X-ray source (Rigaku Micromax, operated at 42kV and 20mA), Osmic confocal MaxFlux optics and a three pin-hole collimation system (JJ X-ray). Samples on the top of approx. 1×1 cm^2 silicon platelets were irradiated at the incident angle (α_i) of 0.20°. Diffraction patterns were recorded for 3h on a MAR345 image plate detector. The camera length (316 mm, calibrated using silver behenate) and the diameter of the detector (34.5 cm) allowed analyzing d-spacings within the range of $\sim 3.5 \text{ nm} < d_{hkl} < 0.3 \text{ nm}$.

10.4.5 OFET performance measurement:

Figure 10.9. OFET measurement system inside glove box.

OFET measurement system was employed inside the glovebox (Figure 10.9). A microscope was used to observe the transistor substrate. Source, drain, and gate electrodes contacts were made by the tungsten tips, which were manipulated under the help of microscope. These probes were connected to Keithley SCS 4200 system for the OFET performance characterization (Figure 10.10). Those probe heads can be moved in the x, y and z directions.

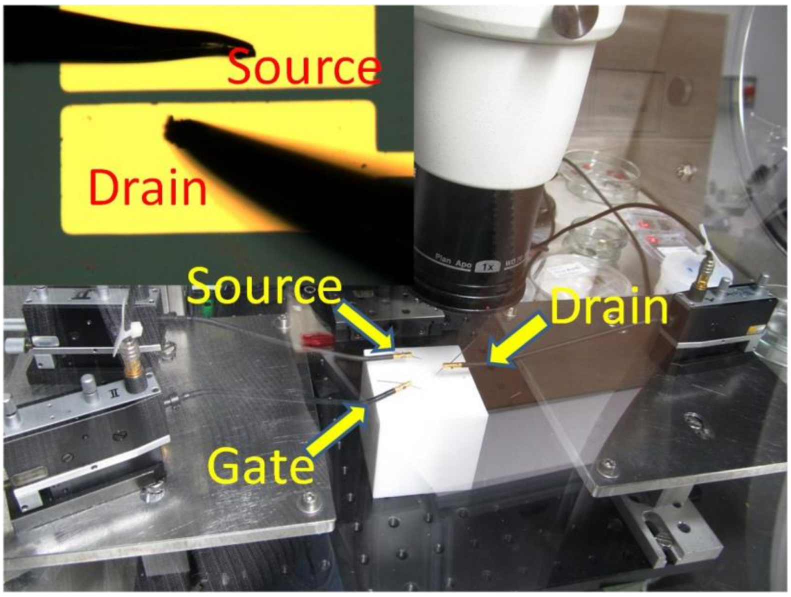

Figure 10.10. Probes for contacting the devices(inset: an OM image of OFET devices).

For the bottom gate, top contact OFETs, source and drain electrodes with channel lengths of 25 µm were defined by a shadow mask, followed by Au evaporation to a height of 100 nm. All standard electrical measurements were performed in a glovebox under nitrogen atmosphere; this ensured the experiments in an oxygen and water free atmosphere.

REFERENCES

[1] V. Palermo, P. Samorì, *Angew. Chem. Int. Ed.* **2007**, *46,* 4428.

[2] Y. Che, A. Datar, K. Balakrishnan, L. Zang, *J. Am. Chem. Soc.* **2007**, *129*, 7234.

[3]D. S. Park, S. J. Kang, H. J. Kim, M. H. Jang, M. Noh, K. H. Yoo, C. N. Whang, *J. Vac. Sci. Technol. B,* **2005**, *3,* 23 .

[4] W. Pisula, A. Menon, M. Stepputat, I. Lieberwirth, U. Kolb, A. Tracz, H. Sirringhaus, T. Pakula, K. Müllen, *Adv. Mater.* **2005**, *17*, 684.

[5] Q. Bao, J. Li, C. M. Li, Z. L. Dong, Z. Lu, F. Qin, C. Gong, J. Guo, *J. Phys. Chem. B* **2008**, *112,* 12270.

[6] D. A. Muller, M. J. Mills, *Materials Science and Engineering*, **1999**, *A260*, 12.

[7] I. Arslan, J. K. Hyun, R. Erni, M. N. Fairchild, S. D. Hersee, D. A. Muller, *Nano Letters*, **2009**, *9*, 4073.

[8] H. L. Xin, D. A. Muller, *Nature Nanotech.* **2010**, *5*, 764.

[9] J. Rivnay, S. C. B. Mannsfeld, C. E. Miller, A. Salleo, M. F. Toney, *Chem. Rev.* **2012**, *12*, 5488.

[10] Y. Wen, Y. Liu, Y. Guo, G. Yu, W. Hu, *Chem. Rev.* **2011**, *111*, 3358.

List of Publications

[1] Kivala, M. *; Pisula, W.; Wang, S. H.; Mavrinskiy, A.; Gisselbrecht J.; Müllen, K.*, Columnar Self-Assembly in Electron-Deficient Heterotriangulenes, *Chemistry-A European Journal*, **2013**, *19*, 8117.

[2] Parvez, K.; Li, R.; Spunreddy, R.; Hernandez, Y.; Hinkel, F.; Wang, S. H.; Feng, X. *; Müllen, K.*, *ACS Nano*, **2013**, *7*, 3598.

[3] Wang, S. H.; Pisula, W.*; Müllen, K.*, Nanofiber Growth and Alignment in Solution Processed n-Type Naphthalene-Diimide-Based Polymeric Field-effect Transistors**,** *J. Mater. Chem.* **2012**, *22*, 24827.

[4] Wang, S. H.; Kiersnowski, A.; Pisula, W.*; Müllen, K.*, Microstructure Evolution and Device Performance in Solution Processed Polymeric Field-Effect Transistors: the Key Role of the First Monolayer, *J. Am. Chem. Soc.* **2012**, *134*, 4015.

[5] Wang, S. H.; Kappl, M.; Lieberwirth, I.; Müller,M.; Kirchhoff,K.; Pisula, W.*; Müllen, K.*, Organic Field-Effect Transistors based on Highly Ordered Single Polymer Fibers, *Adv. Mater.* **2012**, *24*, 417.

[6] Wang, S. H. ; Gao, P.; Lieberwirth, I.; Kirchhoff, K.; Pang, S.; Feng, X.; Pisula, W.*; Müllen, K.*, Field-Effect Transistors Based on Dithieno[2,3-d;2,3'-d']benzo [1,2-b;4,5-b']dithiophene Microribbons by Solvent Vapor Diffusion, *Chem. Mater.* **2011**, *23*, 4960.

[7] Guo, X.; Wang, S. H.; Enkelmann, V.; Baumgarten, M.; Müllen, K.*, Making Benzotrithiophene a Stronger Donor, *Org. Lett.*, **2011**, *13*, 6062.

[8] Wang, S. H.; Dössel, L.; Mavrinskiy, A.; Gao, P.; Feng, X.; Pisula, W.*; Müllen, K.* Self-Assembly and Microstructure Control of Hexa-*peri*-hexabenzocoronene - Perylene Diimide Dyad by Solvent Vapor Diffusion, *Small*, **2011**, *7*, 2841.

[9] Wang, S. H.; Kivala, M.; Lieberwirth, I.; Kirchhoff, K.; Feng, X.; Pisula, W.*; Müllen, K.*, Dip Coating Induced Fiber Growth of a Soluble Heterotriangulene, *ChemPhysChem*, **2011**, *12*, 1648.